

On-Surface Synthesis and Single Molecules Studied Using LT-SPM

M.Sc. Suchetana Sarkar

Dissertation

Submitted to the Faculty of Physics
Technische Universität Dresden

To achieve the academic degree
Doktor (Dr.rer.nat.)

First referee
Prof. Dr. Gianaurelio Cuniberti

Second referee
Prof. Dr. Franziska Lissel

Defence: 19.12.2024

Doctoral Committee

Prof. Dr. phil. Il habil. Lukas Eng

Prof. Dr. Gianaurelio Cuniberti

Prof. Dr. Alexey Chernikov

Dr. Francesca Moresco

Abstract

The behaviour of molecules on surfaces is key to understanding not just their fundamental properties, but can also provide insights into reaction mechanics and rational design principles. Using the surface as a platform for novel reactions that are beyond the scope of solution synthesis, or to trigger conformational changes, is made possible through the atomic “clean-room” provided by a 5 K scanning tunnelling microscope (STM) operating in ultra-high vacuum (UHV) conditions. The tip of an STM can be used to modify and probe molecular structures reproducibly and with a high degree of spatial resolution.

In the first part of this thesis, the self-assembly of two different molecules on Au(111) has been explored. The first molecule, although symmetric, is shown to adsorb in large islands with two distinct domain structures. The role of the substrate temperature and its effect on the molecular dynamics has been studied. This evaluation has been done via both hot deposition and post-annealing the substrate. The second molecule presented is chiral in nature and is shown to adsorb in homo-chiral assemblies. Through sub-molecular resolution using a functionalized STM tip, the structure has been determined and its electronic properties investigated. For both the molecules, the viability of further covalent structures has been discussed.

In the second part of the thesis, the focus is not just on self-assemblies, but on manipulation of single molecules. The first case, a donor-acceptor type thiophene based molecule is found to adsorb in two different conformations, in large islands. This molecule can be manipulated away from the islands, and using inelastic tunnelling tip electrons, reversibly switched between the two conformers. The second molecule, also donor-acceptor type, is shown to adsorb in both a planar and non-planar geometry. The planarity can be tuned by modifying the self-assembly using the STM tip.

In the third part of the thesis, the on-surface synthesis of two different long acenes is presented. The first, an isomer of undecacene, is synthesized using the tip to trigger a dehydrogenation reaction. By utilizing a functionalized tip and qPlus sensor for non-contact atomic force microscopy (nc-AFM), the chemical structure for both the intermediate and final reaction product has been unambiguously assigned. The evolution of molecular orbitals or resonances has been explored in detail, showing an excellent agreement between experimental results and theoretical calculations. The second molecule shown, is the tetradecacene precursor, with the intent to generate fourteen fused benzene rings. The molecule is found to have broken electronic conjugation. Nc-AFM and scanning tunnelling spectroscopy (STS) have been used to correlate these electronic hybridization defects with defects incorporated in the acene structure.

Zusammenfassung

Das Verhalten von Molekülen auf Oberflächen ist der Schlüssel zum Verständnis nicht nur ihrer grundlegenden Eigenschaften, sondern kann auch Einblicke in die Reaktionsmechanik und rationale Designprinzipien liefern. Die Nutzung der Oberfläche als Plattform für neuartige Reaktionen, die über den Rahmen der Lösungssynthese hinausgehen, oder zur Auslösung von Konformationsänderungen wird durch den atomaren "Reinraum" ermöglicht, den ein 5-K-Rastertunnelmikroskop (STM) bietet, das im Ultrahochvakuum (UHV) arbeitet. Mit der Spitze eines STM lassen sich molekulare Strukturen reproduzierbar und mit hoher räumlicher Auflösung verändern und untersuchen.

Im ersten Teil dieser Arbeit wurde die Selbstorganisation von zwei verschiedenen Molekülen auf Au(111) untersucht. Das erste Molekül, obwohl symmetrisch, adsorbiert in großen Inseln mit zwei unterschiedlichen Domänenstrukturen. Die Rolle der Substrattemperatur und ihre Auswirkungen auf die molekulare Dynamik wurden untersucht. Diese Bewertung wurde sowohl durch Heißabscheidung als auch durch Nachglühen des Substrats vorgenommen. Das zweite vorgestellte Molekül ist chiral und adsorbiert nachweislich in homo-chiralen Assemblies. Durch submolekulare Auflösung mit einer funktionalisierten STM-Spitze wurden die Struktur bestimmt und die elektronischen Eigenschaften untersucht. Für beide Moleküle wurde die Realisierbarkeit weiterer kovalenter Strukturen diskutiert.

Im zweiten Teil der Arbeit liegt der Schwerpunkt nicht nur auf Selbstanordnungen, sondern auf der Manipulation einzelner Moleküle. Im ersten Fall, einem Donor-Akzeptor-Molekül auf Thiophenbasis, wird festgestellt, dass es in zwei verschiedenen Konformationen in großen Inseln adsorbiert. Dieses Molekül kann von den Inseln weg manipuliert werden und mit Hilfe von inelastischen Tunnelelektronen reversibel zwischen den beiden Konformeren wechseln. Das zweite Molekül, ebenfalls vom Donor-Akzeptor-Typ, adsorbiert sowohl in einer planaren als auch in einer nicht-planaren Geometrie. Die Planarität kann durch Modifizierung der Selbstanordnung mit der STM-Spitze eingestellt werden.

Im dritten Teil der Arbeit wird die On-Surface-Synthese von zwei verschiedenen langen Acenen vorgestellt. Das erste, ein Isomer von Undecacene, wird mit Hilfe der Spitze synthetisiert, um eine Dehydrierungsreaktion auszulösen. Durch den Einsatz einer funktionalisierten Spitze und eines qPlus-Sensors für die berührungslose Rasterkraftmikroskopie (nc-AFM) konnte die chemische Struktur sowohl für das Zwischen- als auch für das Endprodukt der Reaktion eindeutig bestimmt werden. Die Entwicklung von Molekülorbitalen oder Resonanzen wurde im Detail untersucht, wobei sich eine hervorragende Übereinstimmung zwischen experimentellen Ergebnissen und theoretischen Berechnungen ergab. Das zweite gezeigte Molekül ist der Tetradecacene-Vorläufer, mit dem vierzehn kondensierte Benzolringe erzeugt werden sollen. Das Molekül weist eine gebrochene elektronische Konjugation auf. Nc-AFM und Scanning-Tunneling-Spektroskopie (STS) wurden eingesetzt, um diese elektronischen Hybridisierungsdefekte mit Defekten in der Acenestruktur zu korrelieren.

Contents

1	Introduction	16
2	Scanning Probe Microscopy.....	19
2.1	Introduction	19
2.2	Principle of operation	19
2.3	The STM as an instrument	22
2.4	Scanning tunnelling spectroscopy	23
2.5	Non-contact Atomic Force Microscopy with a qPlus sensor.....	24
3	Manipulation techniques.....	28
3.1	Introduction	28
3.2	Modes of manipulation.....	28
3.3	Lateral manipulation.....	28
3.4	Manipulation induced by inelastic tunnelling electrons	29
3.5	Manipulation induced by electric field.....	29
3.6	Tip functionalization	30
4	Single Molecules Machines Lab	31
4.1	The systems.....	31
4.2	Substrates	35
4.3	Imaging.....	37
4.4	STM image processing and data analysis.....	37
5	Self-assembly and on-surface reactions.....	38
5.1	Fundamentals of self-assembly.....	38
5.2	Surface interactions	39
5.3	Donor-acceptor type molecules.....	40
5.4	On-surface reactions.....	41
5.5	Ullmann Coupling	45
5.6	Overview of unimolecular reactions.....	47
6	Self-assembly of organic molecules on Au(111)	49
6.1	Molecule 1: Acceptor type molecule- HATN	49
6.2	Molecule 2: Azulene based precursor	57
6.3	Summary	65
7	Molecular manipulations in self-assemblies	66
7.1	Thianthrene and next nearest neighbour interactions	66

7.2	Thiophene-based conformational switch.....	81
7.3	Summary	91
8	On-surface synthesis of long acenes.....	93
8.1	Polycyclic aromatic hydrocarbons	93
8.2	On-surface synthesis of isoundecacene.....	94
8.3	On-surface synthesis of tetradecacene: 6-epoxy precursor.....	111
8.4	4 epoxy tetradecacene precursor	121
8.5	Summary	128
9	Summary and outlook	129
10	Bibliography	132
	Scientific contributions	146
	Acknowledgement.....	150
	Curriculum Vitae.....	152
	Statement of authorship.....	156

List of abbreviations

DFT	Density functional theory
d^2I/dV^2	Second derivative of tunneling current over bias voltage
dI/dV	Differential conductance
DOS	Density of states
fcc	Face centered cubic
hcp	Hexagonal closest package
He, LHe	Helium, liquid helium
HOMO	Highest occupied molecule orbital
LDOS	Local density of states
LT	Low temperature
LUMO	Lowest unoccupied molecule orbital
N₂, LN₂	Nitrogen, liquid nitrogen
nc-AFM	Non-contact atomic force microscope
SPM	Scanning probe microscope, Scanning probe microscopy
STM	Scanning tunneling microscopy, Scanning tunneling microscope
STS	Scanning tunneling spectroscopy
UHV	Ultra-high vacuum
vdW	van der Waals

List of figures

Figure 1. Outline of this thesis.	18
Figure 2. The tunnel effect. An electron shown in yellow is tunnelling through a 1D finite barrier (shown in grey).	20
Figure 3: Potential energy diagrams of tip-sample tunnelling in an STM. (a) No applied bias to the sample. (b) Low positive bias applied on the sample, thereby lowering its Fermi energy. The tunnelling proceeds from occupied tip states to unoccupied sample states. (c) Low negative bias applied to the sample. This causes an increase of the Fermi energy and now tunnelling proceeds from occupied sample states to unoccupied tip states.	20
Figure 4. Schematic representation of the measurement modes of an STM (a) constant current mode and (b) constant height mode. (a) In constant current mode, the tip will move up or down to maintain the current set as shown by the squiggly yellow line. (b) In constant height mode, the tip will be maintained at a constant height over the sample, as shown by the straight yellow line.	23
Figure 5: Lennard Jones potential	25
Figure 6: Schematic of a qPlus sensor with metallic tip. S denotes the electrodes to the quartz, while / denotes the tip contact.	26
Figure 7: qPlus sensor characteristics.....	26
Figure 8. LT-STM setups. (a) Photograph of the vacuum setup in STM A. (b) Setup of STM B. The red box is the first port of entry, called the load-lock. The yellow is the next stage in the vacuum chamber, called the preparation chamber. The green is the cryogenic or STM chamber.	32
Figure 9: Different scanner type comparison. (a) Photograph of Besocke-type STM scanner. (b) Photograph of the currently installed PAN Type STM scanner without housing. (c) Exploded schematic of Besocke-type. (1) Ramp. (2) Inner piezo. (3) Sapphire balls. (4) Outer piezo. (5) U-block. (6) Tip. (7) sample.(d) Exploded schematic of a PAN-slider. (1) Body/housing. (2) Shear piezo stacks on both sides of the (3) sapphire prism. (4) Scanner tube (5) Metal tip, either Tungsten (W) or Platinum/Iridium (Pt/Ir). (6) Sample.	34
Figure 10. Photograph of a sample holder for (a) STM A and (b) STM B. (a) 1: Contact plate for thermocouple and heater connections. 2: Grooves for grabbing with the manipulator. 3: Thermocouple. 4: Connection cables for heater and thermocouple. 5: Oven. 6: Sample crystal Au(111). (b) 1: Sample.	35
Figure 11. STM topography (40 nm × 40 nm) of Au(111) showing a step edge. Herringbone reconstruction (can be clearly observed, where the face-centered cubic (fcc) and hexagonal close packing (hcp) domains are separated by the soliton walls and the ridged structures are formed, including the classic elbows or kinks. STM image was taken under $I = 50$ pA and $V = 0.5$ V in constant current mode.	36
Figure 12: Schematic showing an example of self-assembly on a surface.....	40
Figure 13: Relationship between on-surface investigations and rational design.	41
Figure 14: On-surface synthesis via Ullmann coupling.	46

Figure 15: Chemical structure of the precursor. Carbon atoms shown in grey, nitrogen in blue, bromine in green and hydrogen in white.	49
Figure 16: (a) Island with mixed hexagonal and square patterns. (b) Island with only square pattern. Image parameters: (a) and (b) $V = 0.5 \text{ V}$, $I = 10 \text{ pA}$, size: 40 nm^2	50
Figure 17: (a) Close-up of an island with mixed patterns. (b) Schematic representation of proposed molecular arrangement shown in the blue circle. Image parameters: $V = 0.5 \text{ V}$; $I = 20 \text{ pA}$; size : 8 nm^2	51
Figure 18: (a) Close-up of an island with square patterns. (b) Schematic representation of proposed molecular arrangement shown in purple circle. Image parameters: $V = 0.5 \text{ V}$, $I = 20 \text{ pA}$, size = 8 nm^2	51
Figure 19: Pore geometry of 2D-COF	52
Figure 20: (a) Disordered covalent structures near a step edge. (b) Zigzag covalent chains. Image parameters: $V = 0.5 \text{ V}$, $I = 50 \text{ pA}$, size = 15 nm^2	53
Figure 21: (a) Surface after deposition (b) - (e) STM topographies of different areas after post-annealing to 240°C , showing incomplete ring closures. Image parameters: (a) $V = 0.5 \text{ mV}$; $I = 20 \text{ pA}$; size = 40 nm^2 (b) – (e) $V = 0.5 \text{ V}$; $I = 20 \text{ pA}$; size = 10 nm^2	54
Figure 22: (a) Surface after deposition (b) After post-annealing to 240°C . Image parameters: (a) $V = 0.5 \text{ V}$; $I = 20 \text{ pA}$; size = 40 nm^2 (b) $V = 0.5 \text{ V}$; $I = 10 \text{ pA}$; size = 40 nm^2	55
Figure 23: Reaction schematics: (a) Ullman coupling on the surface. (b) Isopropyl coupling. Adapted from [99]	57
Figure 24: Chemical structure of the (a) precursor and (b) expected 2D-COF	58
Figure 25: (a) Two chiralities of the precursor. (b) Surface after deposition. Image parameters: $V = 0.2 \text{ V}$; $I = 100 \text{ pA}$; size = 40 nm^2	59
Figure 26: (a)-(d) Constant current images with CO functionalized tip. (e)-(h) Corresponding constant height images showing molecular structure. Image parameters: (a) $V = 200 \text{ mV}$; $I = 20 \text{ pA}$; size = 2.9 nm^2 . (b) $V = 200 \text{ mV}$; $I = 20 \text{ pA}$; size = 4.3 nm^2 (c) $V = 200 \text{ mV}$; $I = 20 \text{ pA}$; size = $8.5 \text{ nm} \times 5.7 \text{ nm}$; (d) $V = 200 \text{ mV}$; $I = 20 \text{ pA}$; size = $7.1 \text{ nm} \times 2.9 \text{ nm}$. (e) – (h) $V = -5 \text{ mV}$	60
Figure 27: (a) Constant current image of chain structure. (b) Corresponding constant height image. (c) Laplace filter applied to (b), showing bond structure. Image parameters: (a) $V = 0.2 \text{ mV}$; $I = 20 \text{ pA}$. (b) $V = -5 \text{ mV}$. Size: All images = $7.1 \text{ nm} \times 3.6 \text{ nm}$	61
Figure 28: STS on single molecule and on a molecule in chain. Inset: $V = 0.2 \text{ V}$; $I = 20 \text{ pA}$; size = $12.5 \text{ nm} \times 5.7 \text{ nm}$	63
Figure 29: dI/dV maps. Image parameters: (a)-(c) $V = 0.2 \text{ V}$; $I = 20 \text{ pA}$. (d)-(f) $I = 200 \text{ pA}$. All images size: 2.9 nm^2	64
Figure 30: Attempts at surface assisted isopropyl coupling through post-annealing. Image parameters: $V = 0.2 \text{ V}$; $I = 20 \text{ pA}$, size = 40 nm^2	65
Figure 31: bTEPCN chemical structure. Carbon atoms shown in gray, Hydrogen atoms in white, Sulphur atoms in yellow and Nitrogen atoms in blue.	67
Figure 32: bTEPCN crystal structure: (a) Top view of a single bTEPCN molecule in the crystalline structure. (b) Side view of the bTEPCN molecule, showing the non-planarity in the crystal structure. (c) Packing geometry of the bTEPCN molecules in the crystal structure. Figure adapted from [14].	67
Figure 33: Self-assembled molecular islands consisting of bTEPCN molecules adsorbed on Au(111). STM images (a) $10 \text{ nm} \times 10 \text{ nm}$ and (b) $5 \text{ nm} \times 5 \text{ nm}$ showing the unit cell were	

taken at $V = 0.2$ V and $I = 20$ pA. The blue lines in (a) show the stripe-like self-assembly, while the blue and yellow arrows show the two orientations of the molecule.....	68
Figure 34: DFT calculated adsorption geometries of bTEpCN in islands on Au(111). (a) Top view (b) Side view showing non-planarity caused by one peripheral benzene ring.	69
Figure 35: Tuning the nonplanarity of a bTEpCN molecule. (a) The target non-planar molecule located at the edge of the island is marked. (b) Picking up ($V = 10$ mV, $I = 5 - 8$ nA) the three surrounding neighbors (marked with "x") as an indirect isolation. (c) The remaining target molecule becomes planar. All STM images (7 nm x 3.7 nm) were taken under $V = 0.2$ V and $I = 20$ pA.	70
Figure 36: DFT calculated adsorption geometries (side view) of a non-planar and a planarized bTEpCN molecule on Au(111).	71
Figure 37: Linescan comparison. (a – b) STM images (7 nm x 3.7 nm) of before and after planarization by STM vertical manipulation (same images as Figure 3). STM images were taken under $V = 0.2$ V and $I = 20$ pA. (c) Line profiles show the different appearances comparing before and after the planarization	72
Figure 38: Planarization sequence within an island through indirect isolation. Target non-planar molecule shown with white arrow. The four neighbour molecules are picked up by tip manipulation one by one. The target molecule was planarized after removing the fourth neighbour on its bottom left side. All STM images (4.5 nm x 4.5 nm) were recorded under $V = 0.2$ V and $I = 20$ pA. Manipulation parameters: 10 mV, >10 nA. Figure adapted from [14] ..	73
Figure 39: Self-assembled molecular chains and isolated molecule. (a) STM image (25 nm x 8 nm) of a molecular chain along the fcc region of the Au(111) surface. (b) Close-up of a molecular chain (5 nm x 5 nm). (c) An isolated bTEpCN molecule (2.5 nm x 1.5 nm). with same sizes taken at $V = 12$ mV. Constant current STM images were taken under (a) $V = 0.5$ V, $I = 20$ pA, (b, c) $V = 0.2$ V, $I = 20$ pA.....	74
Figure 40: DFT calculated adsorption geometries (top and side views) chain-like self-assembled structures (a – b) and the single molecule (c-d).	75
Figure 41: CO-tip constant height images of different self-assemblies and configurations. (a) Island assembly and non-planar configuration. (b) 1D chain and planar configuration. (c) Isolated molecule in planar configuration. Image parameters: $V = 12$ mV; size: (a) and (b) 5 nm x 5 nm, (c) 2.5 nm x 1.5 nm.....	77
Figure 42: dI/dV spectra and maps of an isolated planar bTEpCN molecule. (a) dI/dV spectrum of the planar (red line) configuration, in grey for comparison the dI/dV spectrum recorded on the clean Au(111). (b) STM topography and the dI/dV maps corresponding to the electronic resonances ($I = 300$ pA).	78
Figure 43: DFT calculated STM topographic image and molecular orbitals.	79
Figure 44: dI/dV spectra and maps of non- planar bTEpCN molecules formed an island. (a) dI/dV spectrum of the non-planar (blue line) configuration, in grey for comparison the dI/dV spectrum on the clean Au(111). (b) STM topography and the corresponding dI/dV maps ..	80
Figure 45: Chemical structure in gas phase. Carbon atoms shown in gray, Hydrogen in white, Nitrogen in blue, Sulphur in yellow and Bromine in green.....	81
Figure 46: Overview STM images of TTPQ molecules adsorbed on Au (111) after sublimation. (a) Large self-assembled island and smaller islands growing along the FCC sites (b) Close-up of an island with the two molecular conformations superimposed: TTPQ-S in green and TTPQ-	

C in blue, (c) Close-up of an island with local domains formed by TTPQ-S (shown in green). Image parameters: (a) $V = 0.5\text{ V}$ and $I = 10\text{ pA}$; $40\text{ nm} \times 40\text{ nm}$ (b) $V = 0.1\text{ V}$ and $I = 20\text{ pA}$; $15\text{ nm} \times 15\text{ nm}$ (c) $V = 0.1\text{ V}$ and $I = 20\text{ pA}$; $15\text{ nm} \times 15\text{ nm}$	82
Figure 47: Isolation of single molecule (TTPQ-C). (a) The blue arrow in the image indicates trajectory of lateral manipulation in constant current mode ($V = 10\text{ mV}$; $I = 2\text{ nA}$). (b) The subsequent image shows that the molecule has been successfully isolated, following the trajectory of the tip. (c) Tip behaviour during manipulation showing tip height vs lateral distance curve. STM images ($6\text{ nm} \times 6\text{ nm}$) were obtained under the conditions of $V = 0.1\text{ V}$ and $I = 50\text{ pA}$	83
Figure 48: Lateral manipulations of two molecules from an island. (a) STM image of an ordered island self-assembly. Lateral manipulation is performed ($V = 10\text{ mV}$, $I = 2\text{ nA}$), where the blue arrow indicates the trajectory of the STM tip. (b) Separation of two molecules from the island and further lateral manipulation using the same parameters is applied along the path shown by the arrow. (c) Completely isolated molecules, both of the C-form. Image parameters: $V = 0.5\text{ V}$ and $I = 10\text{ pA}$; $20\text{ nm} \times 8\text{ nm}$	84
Figure 49: (a) and (b) Experimental STM images of TTPQ-C and TTPQ-S, respectively. Image parameters: $V = 0.1\text{ V}$ and $I = 10\text{ pA}$; $3.0\text{ nm} \times 3.0\text{ nm}$. DFT calculations of adsorption geometry of TTPQ on Au(111): (c) Top view of adsorption geometry (d) Side view of molecular structure showing cis symmetry (TTPQ-C) (e) Side view of molecular structure showing the trans symmetry (TTPQ-S). (f) and (g) Simulated STM images of TTPQ-C and TTPQ-S, respectively. Figure adapted from [5] Figure 49a and Figure 49b show experimental STM images of intact TTPQ-C and TTPQ-S, respectively. The top view of the adsorption geometry as calculated by DFT is shown in Figure 49c. This demonstrates that all the sulphur moieties are pointing away from the molecular backbone. So far, the molecule would appear to be symmetric with only one adsorption geometry possible, however, taking a look at the side view, finally clarifies the differences between the two forms. A closer inspection of the bromothiophene groups reveals that they can adsorb either close or slightly elevated from the surface below. This gives rise to two possibilities. When the two upper groups point away from the surface, the two lower bromothiophenes are inevitably closer to the surface, due to steric hindrance of the adjacent hydrogen atoms. This gives rise to the TTPQ-C form, which can be considered the cis-conformer, as shown in Figure 49d. The second possibility as illustrated by Figure 49e, is when only one of the top bromothiophenes is adsorbed closer to the surface, while the other points away, and the adjacent bottom bromothiophene adsorption is yet again dictated by steric hindrance. This generates the TTPQ-S or trans conformer. The corresponding calculated STM images of the TTPQ-C and TTPQ-S respectively, are shown in Figure 49f and Figure 49g, and are in excellent agreement with the experimental STM image. This proves conclusively that the aforementioned geometries are indeed correct. In conclusion, the two observed conformations of TTPQ on the Au(111) surface are due to the very slight rotation of two adjacent bromothiophene groups.	85
Figure 50: (a) STS spectra of both forms of the molecule (Inset). (b)-(e) topographical STM images ($V = 0.5\text{ V}$ and $I = 20\text{ pA}$), with (d) having all Br intact. (f)-(i) corresponding dI/dV maps taken in constant current mode at (f) 0.6 V (g) 1.2 V (h) 0.6 V (i) 1.2 V . All images $3.5\text{ nm} \times 3.5\text{ nm}$	87

Figure 51: On-surface reversible switching event of the C-form of molecule. (a) A voltage pulse ($V = 2.0$ V, 5 seconds; marked position) is applied above the molecule that was isolated. (b) A slight lateral displacement was induced, and the appearance of the molecule has changed to the S-form. (c) Upon a further pulse in the marked position, the molecule switches back to C-form. (d) - (e) Current vs. time curve showing the tip response during the first and second pulse, respectively. Image parameters: $V = 0.1$ V and $I = 20$ pA.; 4.5 nm x 4.5 nm. Figure adapted from [5]	89
Figure 52: DFT calculation of the bromothiophene groups. The arrows indicate the rotational direction	90
Figure 53: Energy profiles at different states and the corresponding adsorption geometries. Side view of the simulated adsorption geometries, calculated by DFT, starting from TTPQ-S (state I), through intermediate states (II–VIII) to TTPQ-C (state IX). The corresponding reaction energy profiles (in eV) are calculated by the nudged elastic band (NEB) method. Figure adapted from [5].....	90
Figure 54: (a) Self-assembly upon evaporation onto RT Ag(111) showing linkages and single molecules. (b) Single molecules surrounded by dissociated bromines. Image parameters: $V = 0.5$ V and $I = 10$ pA; (a) 80 nm x 80 nm (b) 12 nm x 12 nm.	91
Figure 55: Chemical structure of precursor. Carbon atoms shown in gray, Oxygen in red and Hydrogen in white.	95
Figure 56: DFT calculations of oxygenated precursors on the surface showing incompatible chemical structure.	96
Figure 57: Deoxygenated precursor on the surface.	96
Figure 58: Au(111) surface after deposition: (a) Overview showing linear molecules (in yellow rectangles) and a few kinked molecules (red rectangle). (b) nc-AFM image of two kinked molecules. Image parameters: (a) $V = 0.5$ V and $I = 20$ pA. Image size: 15 nm x 15 nm (b) Image parameters: Amplitude = 150 pm, $V = 1$ mV, size: 6.4 nm x 2.9 nm	97
Figure 59: (a) Image of a single molecule with linescan taken over black line. (b) Line profile showing the length and height of the molecule. Image parameters: (a) $V = -1$ V and $I = 20$ pA . Image size: 4.5 nm x 2 nm.....	98
Figure 60: Tip-induced dehydrogenation and conversion from precursor to final molecule.	99
Figure 61: Pulse-induced dehydrogenation (a) - (c) Constant height CO images of taken after each pulse. Image parameters: $V = 10$ mV, size : 3.5 nm x 2.0 nm.(d) - (f) Constant current STM images with a CO tip showing pulse position (red star). Image parameters: $V = -1$ V, $I = 100$ pA, size: 3.5 nm x 2 nm. (g) - (h): Current vs. time curve showing tip response after each pulse. Pulse parameters: 2 V, 5 seconds. (i) Reaction summary.....	100
Figure 62: Adsorption geometries and image calculations: (a) - (c) Top and side vies of each molecular species' adsorption geometry on Au(111).	101
Figure 63: Calculated STM topographies.	101
Figure 64: (a) Laplace filtered nc-AFM image with CO functionalized tip of the partially reacted II. (b) Laplace filtered nc-AFM image with CO functionalized tip of the final product, III. Image parameters: (a) Amplitude = 300 pm, $V = 1$ mV, size = 4.0 x 1.7 nm (b) Amplitude = 150 pm, $V = 1$ mV, size 4.0 nm x 1.7 nm.	102
Figure 65: STS and constant current conductance maps of I. (a) Constant height STS. Spectra were recorded at the positions shown in the inset. Image parameters: Inset $V = -2$ V, $I = 20$	

pA, image size: 4 nm x 2 nm. (b) Chemical structure of deoxygenated precursor. (c) Conductance maps: Top row: Experimental maps. Bottom row: Calculated maps. Image parameters: I = 200 pA, size of all images: 3.5 nm x 1.7 nm.	104
Figure 66: Constant height STS on II. Spectra were recorded at the positions shown in the inset. Image parameters: Inset V = -2 V, I = 20 pA, image size: 4 nm x 2 nm.	105
Figure 67: Constant current conductance maps of II taken below Fermi energy at incremental bias steps. Image parameters: I = 200 pA, size: 1.7 nm x 3.5 nm.	105
Figure 68: Conductance maps taken below Fermi energy at incremental bias steps. Image parameters: I = 200 pA, size: 1.6 nm x 3.5 nm.	106
Figure 69: (a) Chemical structure of intermediate molecule II. (b) Conductance maps: Top row: Experimental maps. Bottom row: Calculated maps. Image parameters: I = 200 pA, size of all images: 3.5 nm x 1.7 nm.	107
Figure 70: Constant height STS on III. Spectra were recorded at the positions shown in the inset. Image parameters: Inset V = -2 V, I = 20 pA, image size: 4 nm x 2 nm. (b) Chemical structure of deoxygenated precursor. (c) Conductance maps: Top row: Experimental maps. Bottom row: Calculated maps. Image parameters: I = 200 pA, size of all images: 3.5 nm x 1.7 nm.	107
Figure 71: Constant current conductance maps of III taken below Fermi energy at incremental bias steps. Image parameters: I = 100 pA, size: 1.7 nm x 3.5 nm.	108
Figure 72: Constant current conductance maps taken above Fermi energy at incremental bias steps. Image parameters: I = 200 pA, size: 1.7 nm x 3.5 nm.	108
Figure 73: (a) Chemical structure of final molecule III. (b) Constant current conductance maps: Top row: Experimental maps. Bottom row: Calculated maps. Image parameters: I = 200 pA, size of all images: 3.5 nm x 1.7 nm.	109
Figure 74: ACID plots. (a) Deoxygenated precursor I. (b) Final product III.	110
Figure 75: Tetradecacene precursor. Carbon atoms shown in grey, hydrogen in white and oxygen in red.	111
Figure 76: Overview of Au(111) after deposition of tetradecacene precursors. Image parameters: V = 0.5 V, I = 30 pA, size = 35 nm x 25 nm. Stack of tetradecacene precursors shown in green.	111
Figure 77: Close-up of a stack of tetradecacene precursors. (a) Constant current image with a CO-tip. Image parameters: V = 0.5 V, I = 30 pA. (b) Higher bias constant current image with a CO-tip showing position of pulse (red star). Image parameters: V = 2 V, I = 30 pA (c) Constant height image with CO-tip, before pulsing. (d) Post-pulse constant height image with CO-tip. Constant height pulse parameters: 2.5 V, 600 pA. Image parameters for (c) and (d): V = 6 mV. All images size: 5.5 nm ²	113
Figure 78: Pre and post-pulse images of isolated molecule. (a) Pre-pulse constant current image showing pulse positions with arrows. (b) Post-pulse constant current image showing only the bump at the position of the green arrow in (a) disappearing. (c) Pre-pulse constant height image. (d) Post-pulse constant height image, with the conversion of one ring from large to small (green arrow). Image parameters: (a) - (b): V = 2 V, I = 30 pA, size: 4 nm x 2 nm. (c) - (d): V = 5 mV, size: 4 nm x 1 nm. Pulse parameters: Constant height pulse, V = 2.5 V, I = 400 pA.	114

Figure 79: Simplified chemical structure and Laplace filtered constant height images with CO tip showing multiple molecules. Red arrows mark the position of distorted rings. Image parameters: $V = -1$ mV, size: 4 nm x 1 nm	115
Figure 80: Post-pulse molecule. (a) Constant current image with CO tip recorded at $V = 0.1$ V, $I = 100$ pA. (b) nc-AFM with a CO tip: 4.5x1.5nm	116
Figure 81: STS and dI/dV maps one molecule with one distortion. (a) Constant height STS recorded at positions marked in the inset. (b) Constant current dI/dV maps showing broken conjugation. Image parameters: Inset in (a): $V = 0.1$ V, $I = 300$ pA. (b) $I = 300$ pA. All images 4.5 nm x 2 nm.	117
Figure 82: Line scan over pulsed molecule with two distortions. (a) Line scan taken along molecule and over the loop-like distortions. (b). Line profiles showing no contribution of the loop-like features to the apparent height. Image parameters: (a) $V = 2$ V, $I = 30$ pA, size: 5.3 nm x 2.3 nm	118
Figure 83: Simplified schematic of epoxy to ketone conversion. Double bonds and hydrogens have been excluded.....	119
Figure 84: Simplified schematic of epoxy conversion to ring with one or more stereo hydrogens.	120
Figure 85: Simplified schematic representation of possible reaction pathway.	120
Figure 86: Chemical structure of new precursor.....	121
Figure 87: STM over after deposition. Constant current image recorded at $V = 0.5$ V, $I = 10$ pA, size: 30 nm x 15 nm.	122
Figure 88: Pre and post-pulse images of isolated molecule with simplified chemical structure of precursor molecule. (a) - (c) Pre-pulse images. (a) Low bias constant current image. (b) High bias constant current image showing pulsable bump with green star and already existing distortions. (c) Pre-pulse constant height image. (d)- (f) Post-pulse images. (d) Low bias constant current image. (e) High bias constant current image showing the pulsable bump disappearing. (f) Post-pulse constant height image with CO tip. Image parameters: (a), (d): $V = 0.1$ V, $I = 100$ pA. (b), (e): $V = 2$ V, $I = 100$ pA. (c), (f): $V = -1$ mV. All images size: 5 nm x 2.5 nm. Pulse parameters: Constant height pulse, $V = 2.5$ V, $I = 400$ pA.....	123
Figure 89: STS and dI/dV maps one molecule with three distortions. (a) Constant height STS recorded at positions marked in the inset. (b) Constant current dI/dV maps showing broken conjugation at positions of distorted rings. Image parameters: Inset in (a): $V = 2$ V, $I = 300$ pA. (b) $I = 300$ pA. All images 5 nm x 2.5 nm.	124
Figure 90: Pre and post-pulse images of isolated molecule with simplified chemical structure of precursor. (a) - (c) Pre-pulse images. (a) Low bias constant current image. (b) High bias constant current image showing pulsable bumps with green stars and already existing distortions. (c) Pre-pulse constant height image. (d)- (f) Post-pulse images. (d) Low bias constant current image. (e) High bias constant current image showing the pulsable bump disappearing. (f) Post-pulse constant height image with CO tip. Image parameters: (a), (d): $V = 0.1$ V, $I = 100$ pA. (b), (e): $V = 2$ V, $I = 100$ pA. (c), (f): $V = -1$ mV. All images size: 5 nm x 2.5 nm. Pulse parameters: Constant height pulse, $V = 2.5$ V, $I = 500$ pA.....	125
Figure 91: STS and dI/dV maps molecule with two distortions. (a) Constant height STS recorded at positions marked in the inset. (b) Narrower bias range of (a) showing a specific feature around zero bias. (c) Second derivative of (b) showing the spin excitation at 42 mV, either	

side of zero bias. (d) - (e): Constant current dI/dV maps showing broken conjugation at positions of distorted rings. Image parameters: Inset in (a): $V = 2$ V, $I = 100$ pA. (d) and (e): $I = 50$ pA. All images 5 nm \times 2.5 nm. 127

List of tables

Table 1: Types of on-surface reactions. Adapted from [68]	44
Table 2: Summary of deposition attempts	56

1 Introduction

The invention of the Scanning Tunnelling Microscope (STM) in 1981 [1] was a watershed moment in the field of experimental physics. It opened up a new world - the atomic world. Following closely on its footsteps, the Atomic Force Microscope (AFM) which was invented in 1986 [2], pushed the envelope further in images of chemical structures, so much so, that mere decades later, the resolution has allowed us to record organic molecules with such precision, that we can safely conclude that the chemical drawings from high school textbooks are indeed correct.

With the best known example of using a quantum phenomenon in a real world device, the STM, rather Scanning Probe Microscopy (SPM) has become the state of the art technique to not only spatially resolve atomic and molecular structures but also probe them electronically, study their response to electric [3] and also photonic impulses [4] and using these to induce conformational changes [5, 6], triggering reactions that our colleagues in chemistry had abandoned hope for, via on-surface synthesis [7, 8], developing nanomachines like gears, motors, cars [9], and even detecting spin resonance [10]. Perhaps even Richard Feynman himself could not have imagined quite how much room there was at the bottom.

Scientists from very different fields have been able to come together to design experiments that were thought impossible, like detect a single tautomerization event of a molecule [11], create optoelectronic and electronic devices, with the possibility of one day scaling up [12]. These are only two examples from a veritable minefield, but this is to show that SPM is invaluable for both fundamental and applied sciences. Indeed, much like the feedback loop used constant current measurement (Chapter 2), fundamental research must always feed into applied and vice versa.

Given the powerful tools at our disposal (Chapters 3 and 4), one can make good use of them to study molecules, and understand why they do what they do, when they arrange themselves in a certain natural way on surfaces (Chapter 5). This study of self-assembly holds within itself a plethora of information about molecular and surficial attributes and can be used to generate further reaction steps [13] or even tweak the structure of the molecule itself, by changing the self-assembly [14]. A more passive example, it was recently found that the inherent magnetic properties of a lead-containing molecule can change, depending on its particular self-assembly [15].

This thesis combines many of these ideas; of tuning self-assembly with the goal inducing conformational change, exploiting intramolecular interactions to turn a molecule into a reversible switch, try and synthesize in 5K molecules that were

impossible via conventional techniques and also take a closer look at why certain molecules will be less successful in creating complex frameworks, even with all the best intent.

This thesis is organized as follows:

Chapter 6 presents two molecules that were intended for the aforementioned complex chemical structures but were prevaricated from doing so, in part due to their self-assembly and in part due to their inherent properties.

Chapter 7 looks at the successful manipulation of molecules within self-assemblies, in the first case, to modify intermolecular interactions to induce intramolecular change of a thianthrene based molecule. In the second case, using yet again manipulation techniques to promote reversible switching of a thiophene based molecule.

Chapter 8 is dedicated to the on-surface synthesis of long acenes and acene-analogue, where both the successful tip-induced synthesis of an undecacene isomer and the attempted synthesis of a 14-ring or tetradecacene has been presented.

In short, the experiments presented in this thesis, use both the high-resolution imaging and electronic investigation available to us in a low-temperature STM (LT-STM) as shown in Chapter 6 and also the tip-based manipulation techniques (Chapter 3) to induce structural changes (Chapter 7) and create completely new species of molecules (Chapter 8).

An overview of the physics of SPM techniques (Chapter 2), and our in-house systems and resources has also been presented in Chapter 4.

Finally, a summary of all the experimental work discussed in the thesis and an outlook has been provided in Chapter 9.

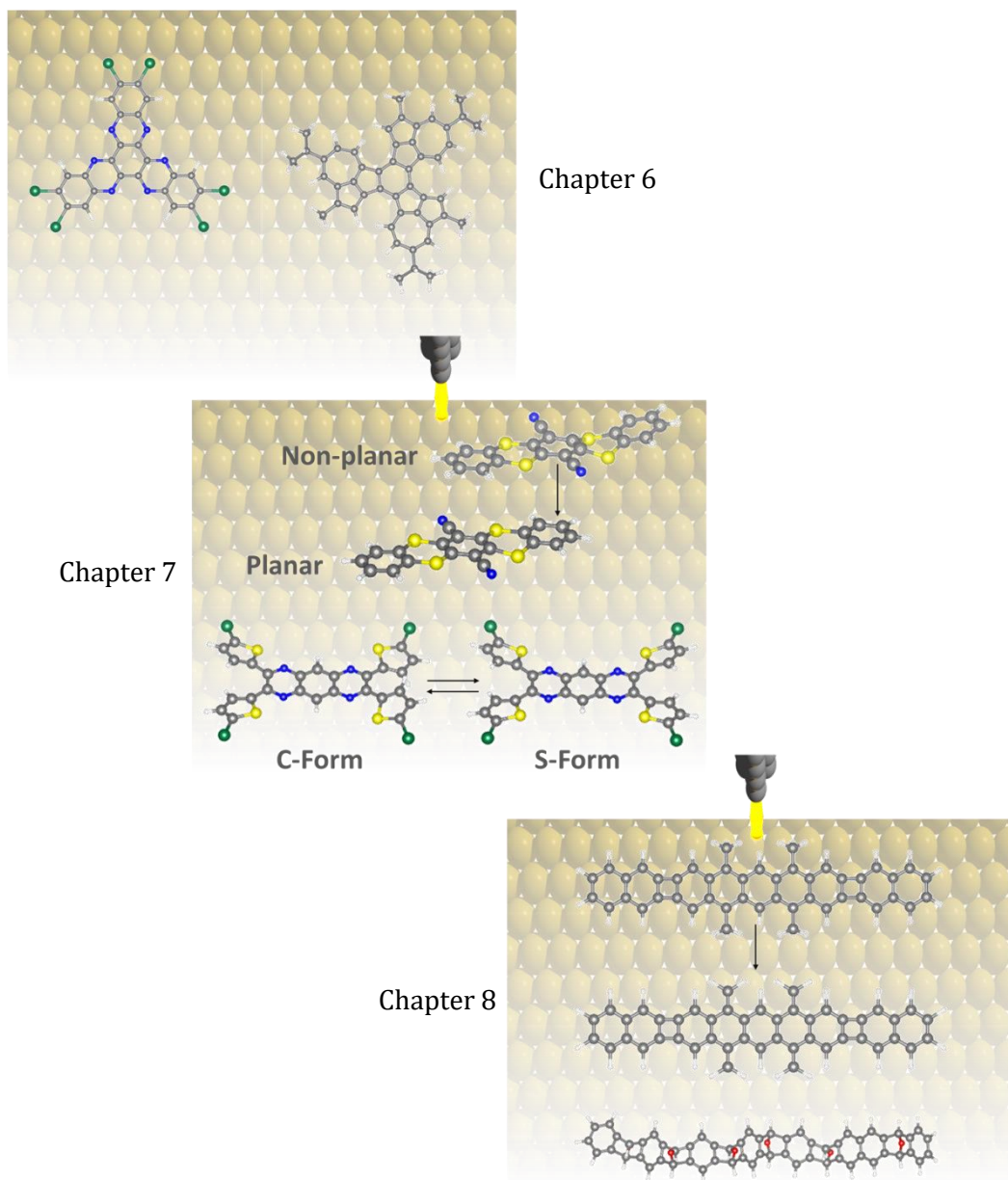


Figure 1. Outline of this thesis.

2 Scanning Probe Microscopy

This chapter is an introduction to scanning probe microscopy and presents the working principles of Scanning Tunnelling Microscopes (STM) and Non-contact Atomic Force Microscopy (AFM). The different measurement modes are presented along with an explanation on Scanning Tunnelling Spectroscopy (STS).

2.1 Introduction

“All approaches at a higher level are suspect until confirmed at the molecular level”, so declared Francis Crick in his book, *What Mad Pursuit*, in 1988 [16].

Thanks to the 1981 invention of the STM by G. Binnig, H. Rohrer, E. Weibel and C. Gerber at IBM in Zurich, Switzerland [17], we are able to not only go to the molecular level, but also atomic [1]. G. Binnig and H. Rohrer earned a well-deserved Nobel Prize in Physics for this invention in 1986, and for the last forty-odd years, STM has become the state-of-the-art technique in not just physics, but biology, chemistry, material science and engineering. In 1990, by demonstrating in 4K that single atoms could be manipulated with great precision, Eigler et.al [18], opened the floodgates to a plethora of possibilities in surface science. This scanning probe technique utilizes the quantum phenomenon called the tunnel effect or tunnelling.

2.2 Principle of operation

With the advent of quantum physics in the early 20th century, the principle of tunnelling has been around much longer than its realization as an experimental technique. It can be understood graphically, as illustrated in Figure 2. It shows a model of tunnelling in a 1D finite barrier. Were it Newtonian Physics, the electron, shown as a yellow ball would not be able to overcome and pass through the barrier, shown as a grey rectangle. But since an electron is considered a quantum particle, manifesting wavelike properties as elucidated by de Broglie [19], if it travels from Region I to Region II, there is a non-zero probability that it can cross the barrier (Region II). This probability, called the transmission probability, decreases exponentially within this finite barrier. This effect is called the tunnel effect.

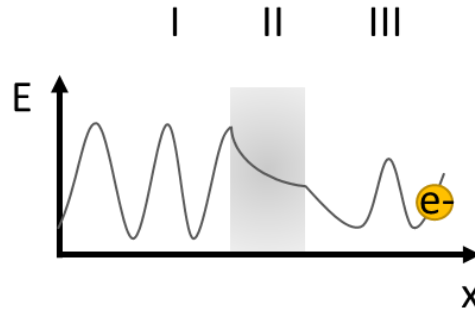


Figure 2. The tunnel effect. An electron shown in yellow is tunnelling through a 1D finite barrier (shown in grey).

Now to understand how this quantum phenomenon can be used in an instrument like the STM, a simple model is presented in Figure 3. The electrons travelling from the tip can be considered region I, the vacuum barrier between the tip and sample is region II and the sample itself is region III. The potential energy is dependent on the work functions of both tip and sample, designated as Φ_T and Φ_S , respectively. When no bias is applied, a situation as illustrated in Figure 3a occurs. However, upon applying a low positive bias, a small current will be generated between the tip and the sample, which we can consider as two electrodes, which can overcome the barrier, as shown in Figure 3b. If we switch the polarity of the applied bias, the direction of the flow of current will also change, as shown in Figure 3c.

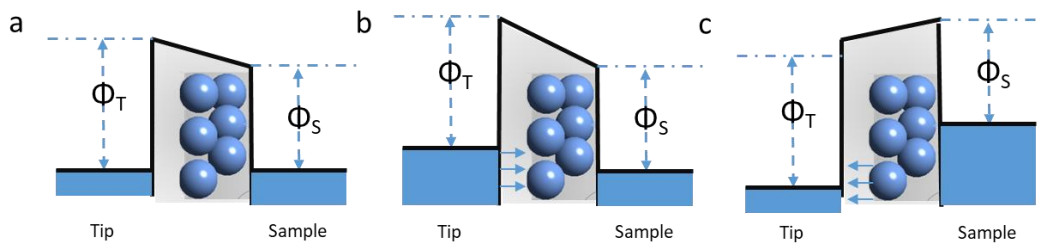


Figure 3: Potential energy diagrams of tip-sample tunnelling in an STM. (a) No applied bias to the sample. (b) Low positive bias applied on the sample, thereby lowering its Fermi energy. The tunnelling proceeds from occupied tip states to unoccupied sample states. (c) Low negative bias applied to the sample. This causes an increase of the Fermi energy and now tunnelling proceeds from occupied sample states to unoccupied tip states.

The probability of an electron travelling from region I to region III, i.e., tip to sample, also known as the transmission coefficient, can be determined by solving a time-dependent Schrödinger equation [20, 21].

This coefficient can be directly expressed as the tunnelling current as a first approximation, and therefore, can be written as shown in the equation below.

$$I \propto e^{-2kd} \text{ with } k = \frac{\sqrt{2m_e\phi}}{\hbar} \quad (2.1)$$

Where, m_e is the mass of an electron, ϕ is the average work function of the two electrodes (tip and sample), and \hbar is the reduced Planck constant.

The reason for the atomic resolution afforded by an STM is also contained in this equation, since there is an exponential dependence of the current on the distance d . This means that small changes in the tip-sample distance, translates as substantial change in the tunnelling current. In real space, this is the reason for change in contrast even at sub-nanometre regimes.

To make the expression for tunnelling current more formal, we turn to J. Bardeen [22], who developed his theory using perturbation and the “golden rule No.2” [23]. This formalism was used later by Tersoff and Hamann as well [24]. Bardeen obtained the following equation:

$$I = -\frac{4\pi e}{\hbar} \int_{-eV}^0 |M|^2 \rho_t(\epsilon) \rho_s(\epsilon + eV) (f(\epsilon) - f(\epsilon + eV)) d\epsilon \quad (2.2)$$

Where, ρ_t and ρ_s are the densities of state (DOS) of the tip and sample respectively, f is the Fermi distribution and M is the tunneling matrix.

We can simplify this equation by assuming that M reflects the probability of an electron to travel from region I to region III, or tip to sample. This is why an approximation of M as an exponential function as shown in Eq. 2.1 is valid.

As STM tip is a clean, atomically sharp metal tip, which means that its DOS is considered flat around the Fermi energy as is constant. Therefore, Eq. 2.2 can be reduced as:

$$I = -\frac{4\pi e}{\hbar} e^{-2kd} \rho_t(0) \int_{-eV}^0 \rho_s(\epsilon + eV) (f(\epsilon) - f(\epsilon + eV)) d\epsilon \quad (2.3)$$

A very important revelation of Eq. 2.3 is that the current is not only exponentially dependent on the tip-sample distance, but also on the integral of the DOS of the sample. At low temperatures, the Fermi function shows a very sharp cutoff at the Fermi energy, and this is the energy window that the electrons can use to tunnel to unoccupied sample states from occupied tip states as shown earlier in Figure 3.

2.3 The STM as an instrument

Taking all of the theoretical considerations into play, we arrive at the standard STM instrument. After bringing the tip close to the sample, a distance of some Angstroms and applying a voltage, a current in the range 1 pA- 10 nA can be detected. Due to the exponential dependence of current and tip-sample distance (shown in Eq. 2.1), even topographic irregularities or as we call it, features in the sub-nanometre range will build a contrast in an STM image. We also know from Eq. 2.3 that the current also depends on the DOS of the sample. This means that we have access to two different modes of operation.

2.3.1 Constant current mode

This is the usual mode of scanning (going line-by-line) a sample, where a feedback loop is employed to maintain a constant current. This means, we will have a change in the tip height over the sample, or tip-distance change is the observable we get. This has been illustrated in Figure 4a. This movement of the tip is controlled by a piezo-actuator.

2.3.2 Constant height mode

In this mode, there is no need for the feedback loop, since the tip-sample distance remains constant. This has been illustrated in Figure 4b. This measurement mode requires caution, since it is very easy to crash into the sample, or any adsorbate therein. The signal or observable we derive from this mode is the change in current. The most common use of this is for high-resolution images with a CO-functionalized tip to resolve intramolecular structures [25]. This will be discussed in the next chapter.

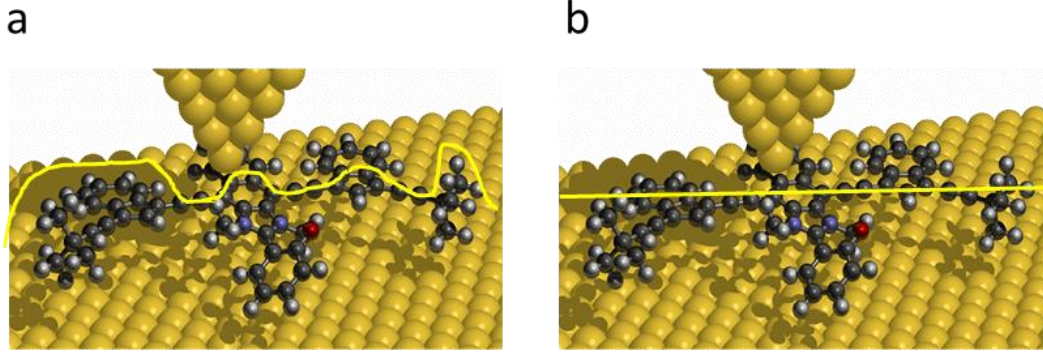


Figure 4. Schematic representation of the measurement modes of an STM (a) constant current mode and (b) constant height mode. (a) In constant current mode, the tip will move up or down to maintain the current set as shown by the squiggly yellow line. (b) In constant height mode, the tip will be maintained at a constant height over the sample, as shown by the straight yellow line.

2.4 Scanning tunnelling spectroscopy

Since we have established that an STM tip is also sensitive to the DOS of the sample, we can use STS to record and identify resonant states of a molecule or molecular system. To do this, we first record the differential conductance, i.e., the first derivative of the current I with respect to voltage [21], which is:

$$\frac{dI}{dV} = -\frac{4\pi e}{\hbar} e^{-2kd} \rho_t(0) \int_{-eV}^0 \rho_s(\epsilon + eV) \frac{\partial f}{\partial \epsilon} d\epsilon \quad (2.4)$$

The differential conductance therefore, depends on the local densities of states (LDOS) of the sample and tip.

This was the theoretical principle of STS, to achieve it experimentally, the following is done. The tip is positioned over a feature of interest with a certain tip-sample distance in constant height mode, which means without the feedback loop active. The bias is then ramped up from a negative to positive value in a fixed range. This records the I/V characteristics, but to obtain the first derivative, a lock-in detector must be employed. A lock-in amplifier is used to provide an additional sinusoidal wave (V_{mod}), to modulate the bias that we apply (V_0). This has a certain frequency, ω . The tunnelling current can also be written as an extension of the Taylor series around V_0 as :

$$I(V) = I(V_0) + \frac{dI(V_0)}{dV} V_{mod} + \frac{d^2 I(V_0)}{dV^2} V_{mod}^2 \sin^2(\omega t) + \dots \quad (2.5)$$

The second term in Eq. 2.5 describes the current modulation with ω , while all higher terms have a short periodicity. This implies that the lock-in amplifier is essentially

functioning as a band-pass filter for the frequency we set, and the first term describes merely the current we measure of the unmodified signal. Since the current is proportional to the dI/dV , this technique can detect it as a direct observable.

This spectroscopic data where we can obtain and identify molecular resonances can then also be mapped spatially with dI/dV mapping or conductance mapping. In this case, one can image an area of interest, at certain energy values which indicate the position of resonances to see the distribution of said resonances. In this way, we can get not only information about the topography of a feature, but also its electronic characteristics.

The usual procedure for performing STS, as has also been presented in this thesis is as follows. The tip is positioned over the target molecule and the feedback loop opened. The voltage is then ramped between ± 2.5 V. It is important to first do this over the bare metal, in this case Au(111) surface, and check for the characteristic surface states, to ensure the metallicity of the tip.

For our experiments, all spectroscopy measurements were conducted in constant height mode, while dI/dV maps were obtained in constant current mode. Spectra and maps were measured using lock-in detection with a modulation frequency of 833 Hz and a modulation amplitude of 40 mV. Only those tips showing the Au(111) surface state were used for spectroscopy measurements on the molecules.

2.5 Non-contact Atomic Force Microscopy with a qPlus sensor

Atomic force microscopy (AFM) followed quickly in the footsteps of the invention of STM, since people wanted to image and probe non-conductive surfaces as well [2]. AFM, like STM also contains a sharp tip acting as a probe. But unlike the STM tip which works with the principle of tunnelling electrons, thereby necessitating a conductive surface, the AFM tip, which is mounted on a flexible cantilever, reacts to forces between the tip and the sample, and the cantilever deforms or deflects as it scans over the sample. These deflections can be detected and a topographic picture of the sample thus generated.

The origin of these deflections can be understood with the Lennard-Jones potential [26], which is a model describing the intermolecular interactions. Figure 5 shows the most this potential as a graph. ϵ denotes the well depth and is indicative of how strongly two interacting particles can attract each other. σ is the distance where the potential between the participating particles is zero [27].

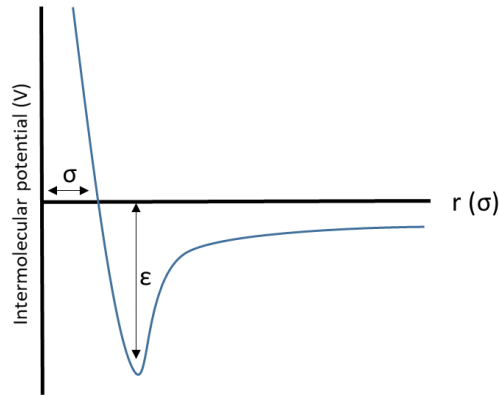


Figure 5: Lennard Jones potential

Simply put, interacting particles (atoms, molecules, nanoparticles etc.), will repel each other at close distances and conversely, attract each other at larger distances. In the former case, due to the very small tip sample distance, also called contact mode, the electronic orbitals overlap, giving rise to exchange interactions.

The latter case, i.e., attractive regime is mediated via weak van der Waals (vdW) forces and causes polarization interactions between tip and sample. This is also called the non-contact mode and will be the focus of this section.

2.5.1 qPlus Sensor

In classical AFM, the tip is a cantilever, which oscillates near its resonant frequency and vdW forces between the tip and sample cause changes in amplitude and oscillation phase. This is the non-contact mode as mentioned previously. However, with this technique, only pure AFM can be performed. To be able to combine STM and AFM, was realized by Franz Giessbl, with his invention of a qPlus sensor [28], a simplified schematic of which is shown in Figure 6. Instead of a deflecting cantilever, a metallic tip is contacted directly to a quartz sensor in the form of a tuning fork. Unlike the cantilever design, where the force-sensing or deflection was detected via optical methods, the qPlus sensor utilizes the natural piezoelectricity of quartz, and is therefore, self-sensing [29]. Compared to a normal quartz tuning fork, such as the ones used in watches, which have two oscillating tines, the qPlus sensor has only one tine that oscillates, while the other is immobilized. Due to this incorporation of a quartz tuning fork, which is much stiffer than the normal deflecting cantilever used in standard AFM, the qPlus sensor is more sensitive to weak or smaller forces, making it very suitable for measurements in the atomic regime. Therefore, as a direct benefit of this increased sensitivity, even better spatial resolution of atomic and molecular structures is now possible.

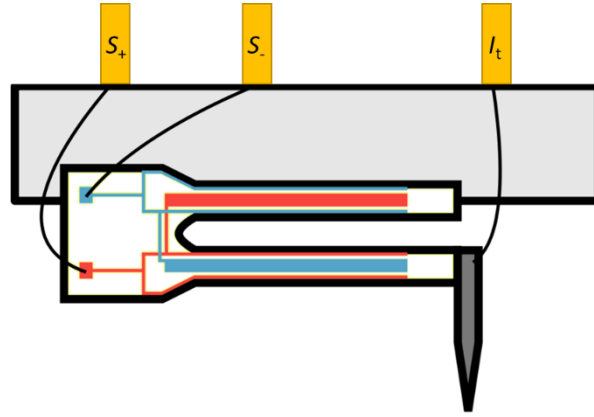


Figure 6: Schematic of a qPlus sensor with metallic tip. S denotes the electrodes to the quartz, while I denotes the tip contact.

Time, and its inverse, frequency are one of the physical observables that can be measured with greatest precision [30]. Therefore, the use of frequency modulation in AFM (FM-AFM) emerged as the preferred mode of operation. The qPlus sensor also detects forces by recording the changes in the eigen or resonance frequency and oscillation amplitude. To do this, first the resonant frequency of the sensor has to be determined, since the change in frequency will be around this resonance. The qPlus sensor properties as used in our lab have been shown in Figure 7. The resonant frequency is around 27 kHz, with a very high quality factor (Q factor) of 30k. This is a measure of the damping of the oscillation, a high value indicating low energy loss and sharp resonance [31].

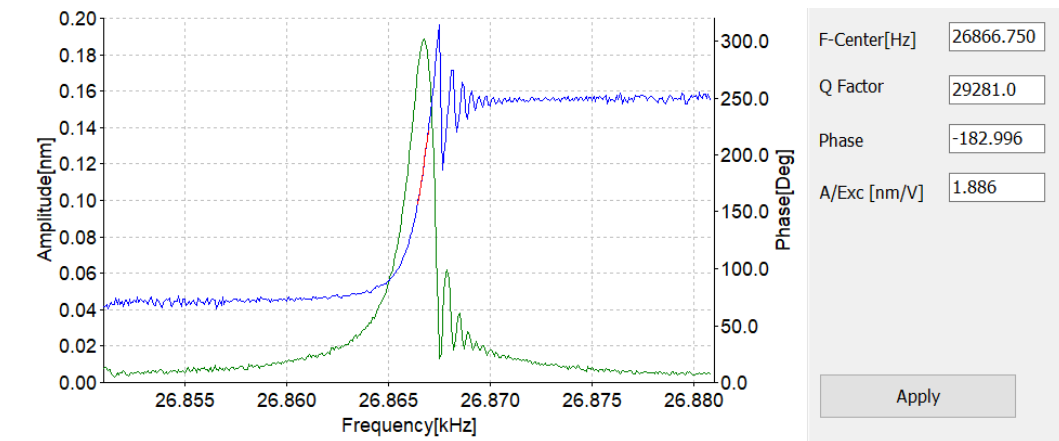


Figure 7: qPlus sensor characteristics.

The resonant frequency is given by:

$$f_o = \frac{1}{2\pi} \sqrt{\frac{k}{m}} \quad (2.6)$$

Where m is the mass of the cantilever, and k its spring constant. In the case of the qPlus sensors, the cantilever can be approximated as a rectangular beam [29], and therefore the fundamental eigenfrequency or resonance frequency can be written as Eq 2.7 instead [32]:

$$f_o = 0.162 \cdot \frac{h}{L^2} v_s \quad (2.7)$$

Where, L is the length of the beam, height is h and v_s is the speed of sound in quartz.

Therefore, the interaction force between tip and sample can be expressed as Eq. 2.8 [33]:

$$\Delta f \approx \frac{-f_o}{2k} \left\langle \frac{\partial F}{\partial z} \right\rangle \quad (2.8)$$

Where, $\left\langle \frac{\partial F}{\partial z} \right\rangle$ is the averaged gradient of the interaction force.

The stiffness of the tuning fork is also quite high, 1800 N/m, which is responsible for the high Q factor. This allows for the detection of small forces, causing the very high resolution that we can achieve with this technique. Additionally, quartz sensors provide stable oscillations, reducing thermal drift, a critical parameter in low temperature measurements.

3 Manipulation techniques

3.1 Introduction

Often it becomes necessary to isolate molecules from their adsorption positions via tip-based techniques as has been the case presented in Chapter 6 and Chapter 7. For example, in Chapter 6, we report the case of a non-planar molecule, that adsorbed in two kinds of planarity, depending solely on the architecture of its self-assembly.

Furthermore, we demonstrated that by tuning the self-assembly through tip-based manipulations, we were able to tune the planarity of the molecule itself. This molecular transformation through intermolecular interactions has been explored in the first part of Chapter 6.

Tip-based manipulations have also proved efficient in inducing intramolecular transformations in a not only isolated molecules, but also on a large number of molecules within an island, and continues to be of interest in this field of research [6, 34-36]. The second molecule presented in Chapter 6 is an example of such an intramolecular conversion from one form to another, induced reversibly through tip electrons.

This chapter will therefore introduce the ways in which manipulation of atoms or molecules can be undertaken in our LT-STM.

3.2 Modes of manipulation

Broadly speaking, we can divide the manipulations into two categories: lateral and vertical. The former is mediated by atomic forces, like vdW, while vertical manipulation can be undertaken through inelastic tunnelling electrons or the electric field effect. Both manipulation modes have been elaborated in the upcoming sections.

3.3 Lateral manipulation

Lateral manipulation is used to move molecules or atoms by almost pulling or pushing them [37]. The tip is brought close to the surface, less than 5 Å, and then moved laterally. This is a multistep process, where the tip (i) approaches the target vertically, with a low bias, (ii) is driven across the sample over the target with a set trajectory, (iii) then retracted to normal scanning position. In constant current mode, which is the mode used for all lateral manipulation in this thesis, the bias is around 1 mV – 10 mV and current around 1

nA, which results in a high tunnelling resistance of $1\text{ M}\Omega - 10\text{ M}\Omega$. This technique was first used by D. M. Eigler and E. K. Schweizer from IBM in California, to position individual Xenon (Xe) atoms on a Nickel(110) surface and write "IBM" [18]. Since then, this technique has been used to induce and probe conformational changes in molecules, and is very important in the field of molecular machines [9].

3.4 Manipulation induced by inelastic tunnelling electrons

In this type of manipulation, the tip is positioned over the target at a fixed point and a bias applied to it, without moving it laterally. This has been used since the 1990s, the first demonstration being the construction of quantum corrals [3].

In the elastic tunnelling regime, the energy of an electron is conserved. But when an electron undergoes inelastic tunnelling, it can lose part of its energy, which could then be transferred to the sample or molecule, exciting vibrational modes [38]. This can then be converted to movement, either translational or rotational. This is a crucial technique for understanding the mechanical behaviour of molecules, and its propensity towards different kinds of motion or switching [39] [40] [5]. In fact, in the International Nanocar Races [41-43], that our group participated in, the driving mechanism was through vertical manipulation techniques.

Additional to exciting vibrational modes, tunnelling electrons can also tunnel into resonances, in which case, the target will undergo an electronic transition into an excited state. During the subsequent relaxation, it has the possibility to move into another lattice site, something that is called lattice hopping. Typically, bias required to generate movement by exciting vibrational the modes is lower than the one through electronic transitions [39, 40, 44, 45].

3.5 Manipulation induced by electric field

It is important to remember, that when a bias voltage is applied to the tip, which can be thought of an electrode, a static electric field is generated between it and the sample surface, which is another electrode. The tip-sample distance will dictate the strength of this electrostatic field, but it is usually in the order of 10^7 V/cm . This means that for certain molecules, for example with a dipole moment or large charge separation, For molecules having a large intramolecular charge separation or dipole moment, they can be excited and moved controllably on the surface by using electric field [46]. This is a polarity dependent effect, and the effect of directional motion in such locally generated electric fields is still a matter of on-going research [47] [48].

3.6 Tip functionalization

A common lament of an STM operator is often that while performing tip manipulations, the target is lost because the tip picks it up. But when done intentionally to pick up a carbon monoxide (CO) molecule, it can serve to enhance the resolution of the STM image not only topographically, but also to better resolve molecular orbitals [25, 49]. Moreover, by terminating a qPlus tip apex with a CO molecule, researchers were able to resolve the internal structure and bond order of organic molecules in qPlus nc-AFM imaging [50, 51]. This process is called CO tip functionalization.

The reason for this increased resolution is the difference between the usual tip state, which is s-wave, vs. the functionalized tip state, which is p-wave. With a metallic s-wave tip, the STM images will resemble the LDOS, given by the modulus squared of the sample wave functions at the Fermi energy [24]. However, upon functionalizing it with CO, the tip state changes to p-wave [52], which show the spatial derivatives of the sample wave functions [32].

After a sample has been prepared with molecules, the CO is dosed in the chamber through a leak valve, upto a certain pressure value, usually, 10^{-8} mbar. The sample is then cooled to 5K, and scanned to detect CO molecules. The CO molecule can be picked up by vertically approaching it with a bias of -1.8 V to -2 V, and retracting the tip quickly. If successful, the CO attaches at the tip apex electrostatically via the carbon atom.

There have been experiments with a variety of tip functionalization, for example with hydrogen [53] and deuterium [54], Xenon atoms and CH₄ molecules [55], but CO terminated tips are by far the most popular and have been used for all tip-functionalization operations in this thesis.

4 Single Molecules Machines Lab

Our lab is called the Single Molecules Machines Lab (SMM), and this chapter will be a brief introduction to the LT-STMs, substrates and other resources available to us.

4.1 The systems

The lab is now equipped with two custom-built LT-STMs, operating at 5K and UHV conditions. Both have been manufactured by (CreaTec Fischer & Co. GmbH, Industriestr. 9, 74391 Erligheim, Germany). Both of these systems have been used for the experiments presented in this thesis.

4.1.1 Ultra-high vacuum systems

All experiments have been carried out in UHV conditions, with a base pressure of about 1×10^{-10} mbar. A cascading series of pumps in different sections of the system enables one to go from ambient conditions to UHV. Figure 8 shows the setup of both the STMs which are almost identical. The older STM is called STM A and is shown in Figure 8a, while the newer STM is called STM B and is shown in Figure 8b. To bring a sample or tip into the system, one must access the load-lock highlighted by the red box in Figure 8. This can be vented with dry nitrogen, and conversely pumped first with a rough pump or pre-pump pump ($\sim 1 \times 10^{-2}$ mbar), and then, with the turbo molecular pump ($\sim 1 \times 10^{-8}$ mbar).

Once the vacuum has reached this value, which is in the high vacuum regime, the sample can be introduced in the preparation chamber, shown in yellow. This chamber is pumped by an ion getter pump (IGP), which in combination with a titanium sublimation pump (TSP), can reach an ultra-high vacuum of 1×10^{-10} to 10^{-11} mbar. All sample preparation operations like cleaning the substrates, and deposition of molecules, are carried out in this chamber.

Finally, when we are ready to scan the sample, it is introduced into the STM or cryogenic chamber, shown in green. This chamber is also pumped via an IGP, and cooled to 5K via a nested cryo setup, where the outer cryo is cooled to 77 K with liquid nitrogen (LN_2) and the inner cryo cooled to 5 K via liquid Helium (LHe).

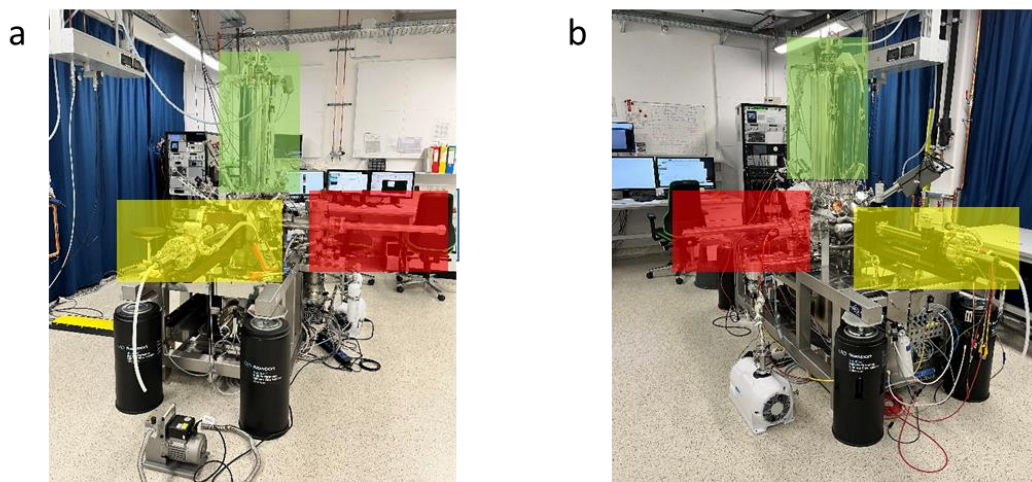


Figure 8. LT-STM setups. (a) Photograph of the vacuum setup in STM A. (b) Setup of STM B. The red box is the first port of entry, called the load-lock. The yellow is the next stage in the vacuum chamber, called the preparation chamber. The green is the cryogenic or STM chamber.

Each of these chambers is separated via gate valves, which can be closed to separate them from each other. The load-lock is equipped with a lamp for degassing anything that needs to be introduced into the prep chamber. To transfer, a transfer rod is provided that can move into the prep chamber.

To move samples or tips from the prep to the STM in STM A, a manipulator is provided that has degrees of motion in all directions (x , y , z , Θ). There are specific positions at which a sample has to be placed for cleaning and depositing of molecules, which can also be accessed via the manipulator. The manipulator is used to anneal the samples as well, through the electrical feedthrough at the head.

In STM B, the sample is transferred into the cryo chamber in the scanning position, from the manipulator, via a wobble stick. The sample holder itself is quite different, along with the manipulator, as will be discussed in the upcoming sections.

4.1.2 Preparation chamber

The preparation chamber is equipped with several other components along with the manipulator: a sputter gun, a Knudsen cell molecular evaporator with four slots, a metal evaporator with one evaporant rod, and a storage rack where multiple samples and sample holders, tips, and tip transfer tools can be housed. The storage also has a lamp to anneal the tip apexes via electron bombardment, if so desired. The preparation chamber also has a quartz microbalance to determine the rate of molecular deposition and therefore coverage on our sample. Its sensitivity in the range of ± 0.1 Hz and is

driven to oscillate at about 6 MHz. A mass spectrometer is also housed in the chamber for analysis of residual gases, contaminations or to perform leak tests. In STM B, the storage is in the form of a vertically mounted carousel in the STM chamber.

4.1.3 STM Chamber

Achieving a temperature of 5 K is made possible by a two-stage cryostat coupled to the STM. The outer cryostat, with a 14-liter capacity, is filled with liquid nitrogen (LN₂), while the inner cryostat, which holds 4 liters, is filled with liquid helium (LHe). With a typical LHe consumption rate of 100 mL per hour, the system can maintain cooling for approximately 80 hours before a refill is needed. To isolate the 5 K-cooled STM from the room temperature environment during sample transfers, a shutter can be opened. The STM's electrical cabling runs through the cryostat.

During operation, the STM scanner is suspended by three springs, providing significant mechanical vibrational damping. The scanner's position for transfer is controlled by a push-pull mechanism, since it requires mechanical restriction. To minimize mechanical noise from the surrounding environment, the entire setup is supported by four pneumatic feet, and the STM scanner is stabilized using an eddy current damping system. This vibration isolation is crucial for achieving a vertical resolution of 0.01 pm in STM, with the stability of the tip-sample spacing maintained at 0.001 pm [56] .

4.1.4 STM scanners

Before 2021, the STM was fitted with the Besocke Beetle-type [57, 58] design as the STM head, shown in Figure 9a.

However, at the end of 2021, the slider in STM A was upgraded to a Pan-slider type scanner [59], as shown in Figure 9b, and STM B also has this same scanner type.

Figure 9c is an exploded schematic representation of how the old Besocke-type scanner worked. This used a stick-slip motion, where the coarse approach was achieved via a serrated circular ramp, which was divided into three segments.

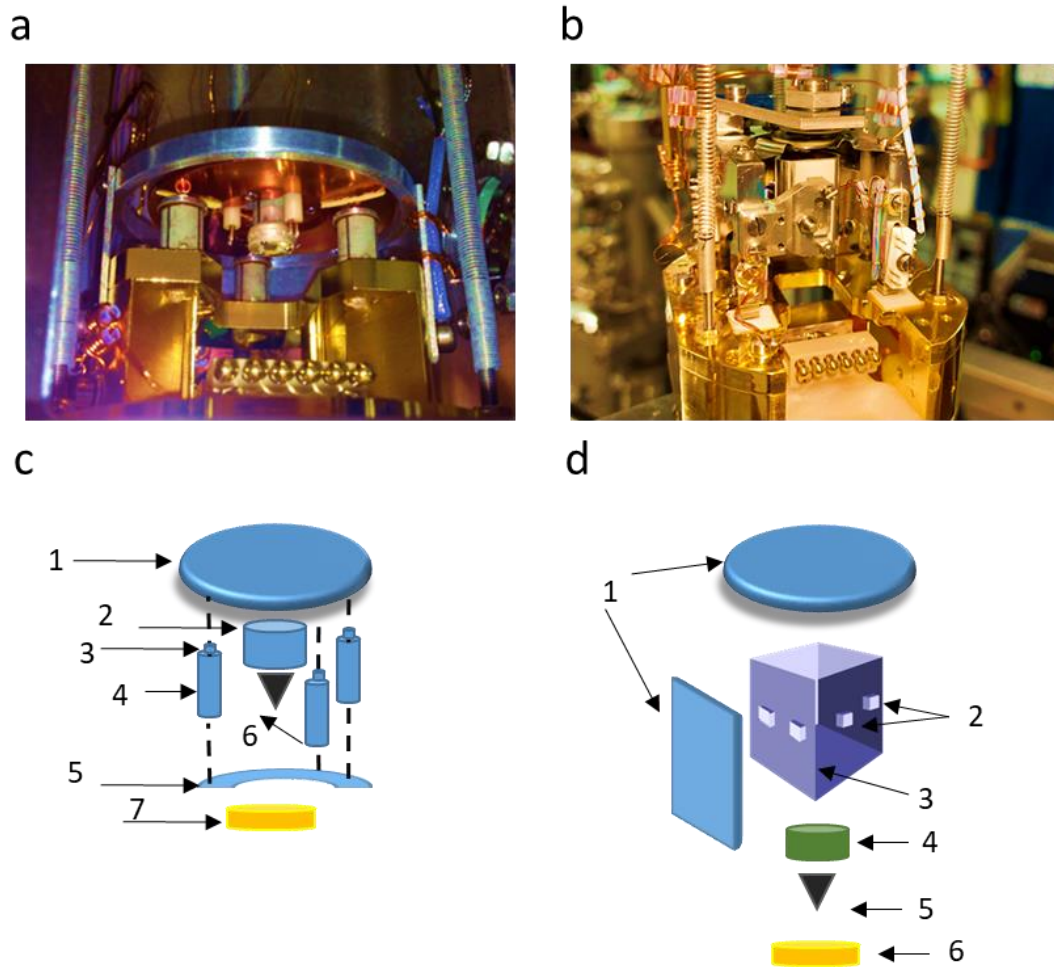


Figure 9: Different scanner type comparison. (a) Photograph of Besocke-type STM scanner. (b) Photograph of the currently installed PAN Type STM scanner without housing. (c) Exploded schematic of Besocke-type. (1) Ramp. (2) Inner piezo. (3) Sapphire balls. (4) Outer piezo. (5) U-block. (6) Tip. (7) sample. (d) Exploded schematic of a PAN-slider. (1) Body/housing. (2) Shear piezo stacks on both sides of the (3) sapphire prism. (4) Scanner tube (5) Metal tip, either Tungsten (W) or Platinum/Iridium (Pt/Ir). (6) Sample.

The new Pan-type scanner is constructed differently. In the z-direction, i.e., vertical direction, the sapphire prism is attached with shear piezo stacks, responsible for the coarse motion. The prism also has the scan tube, which also houses the tube scanner. The linear stick-slip motion of the PAN type is superior to that of the Besocke-type, which used rotary motion for the coarse approach. This has the disadvantage of inducing unintentional lateral shifts, thus making z-motion and re-approaching the same area unreliable.

4.2 Substrates

Unless otherwise stated, a single Au(111) crystal was used in all experiments. The main difference between STM A and STM B is the sample holder type, as can be seen in Figure 11. The STM A sample holder (Figure 10a) is much more complex and houses all connections to heat and readout the temperature of the sample. Since it is bulkier, cooling down from room-temperature (RT) to 5 K, takes about 3-4 hours. On the other hand, the STM B sample holder, houses just the sample and is much lighter, therefore we can reach 5 K in around 40 minutes.

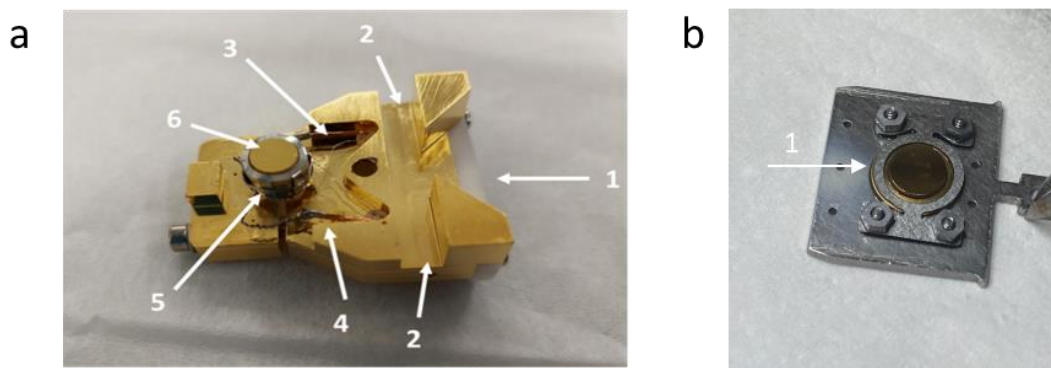


Figure 10. Photograph of a sample holder for (a) STM A and (b) STM B. (a) 1: Contact plate for thermocouple and heater connections. 2: Grooves for grabbing with the manipulator. 3: Thermocouple. 4: Connection cables for heater and thermocouple. 5: Oven. 6: Sample crystal Au(111). (b) 1: Sample.

Unlike in STM A, where the sample is connected with heater cables and thermocouples for annealing, the STM B manipulator has various slots in which we can install the samples, to anneal them.

In order to obtain an atomically flat and clean surface, multiple round of Argon (Ar^+) sputtering and subsequent annealing cycles have to be performed. Depending on the surface and level of contamination, the parameters of the sputter-anneal cycles can vary. As mentioned earlier, all cleaning operations are carried out in the preparation chamber. The sample (Au(111) in the present case) is positioned in front of the sputter gun at 45° . Ar gas is introduced in the chamber, which the sputter gun ionizes (Ar^+ ions; applied power at 0.5 keV for STM A and 2.5 keV for STM B) at a pressure of 2.5×10^{-5} mbar, and sputtering is done for 15-30 minutes, in order to bombard away the topmost layers of the Au(111) crystal. Annealing the sample for 20-30 minutes at 450°C reconstructs the Au(111) surface. In the standard procedure, three cycles are usually done to obtain an atomic-flat Au(111) surface. In STM A, after the cleaning

procedure, the sample holder is cooled by LN₂ (through the manipulator) before transferring it inside the cryostat. This is not done in STM B.

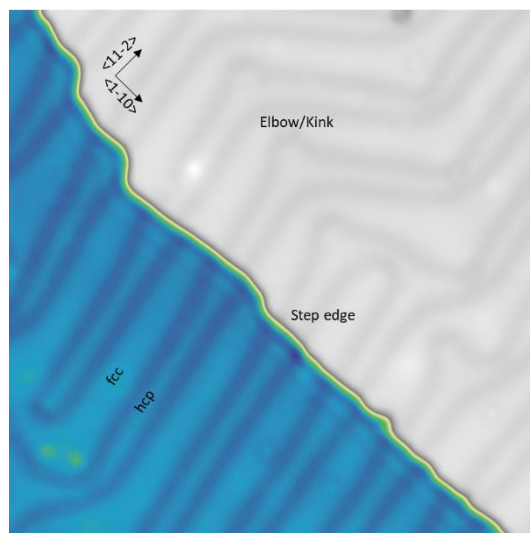


Figure 11. STM topography (40 nm × 40 nm) of Au(111) showing a step edge. Herringbone reconstruction (can be clearly observed, where the face-centered cubic (fcc) and hexagonal close packing (hcp) domains are separated by the soliton walls and the ridged structures are formed, including the classic elbows or kinks. STM image was taken under $I = 50$ pA and $V = 0.5$ V in constant current mode.

Figure 11 presents an STM image of an atomically clean Au(111) surface. The Au(111) surface is notable for having an additional gold atom in its topmost layer unit cell (23 atoms instead of the usual 22). This phenomenon can be understood through a two-step process [60]:

(1) The top layer compacts into a $22 \times \sqrt{3}$ stripe pattern by adding an extra Au atom into an $\langle 1-10 \rangle$ atomic chain every 22 lattice constants. This insertion creates an apparent height difference of 0.22 Å as observed in the STM topography.

(2) The formation of this stripe pattern relieves the strain in the topmost layer along the $\langle 1-10 \rangle$ direction. Consequently, a herringbone reconstruction, characterized by a periodic length of approximately 30 nm, becomes visible. This reconstruction features face-centred cubic (fcc) and hexagonal close-packed (hcp) domains separated by soliton walls, forming ridged structures. The fcc domains are broader than the hcp domains. Additionally, dislocations occur at the elbows of the herringbone pattern during reconstruction, which serve as favourable adsorption sites for molecules.

Additionally, the Au(111) surface also has monoatomic step edges, as shown in the figure.

4.3 Imaging

In our experiments, unless stated, a vast majority of STM images have been obtained in the constant current mode, which is with the feedback loop active, and the bias voltage (V) applied to the sample. The tip is a W tip in STM A and a Pt/Ir tip in STM B, the qPlus sensor is also equipped with a Pt/Ir tip. Typical tunnelling current set points are in the range of 5 pA to a few hundred pA, amplified by a low-noise preamplifier by a factor of 10^9 V/A. For specific scanning purposes e.g., atomic resolution with a CO-functionalized tip or nc-AFM, constant height mode (feedback off) has been used.

An atomically-sharp tip with only one atom at the apex is key in order to obtain good STM images. This is usually achieved by gently crashing the tip inside the metallic surface (through vertical manipulation) until the usual features on the surface like step edges or adatoms are clearly resolved.

4.4 STM image processing and data analysis

Along with the commercial Createc STMAFM software that comes with the instrument, image analysis and post-processing of raw data have been done by Gwyddion [61]. This includes generally the following: resizing or cropping, filtering for noise reduction or certain post-processing choices like Laplace filter for nc-AFM images. The images are also tuned for contrast and colour maps. Line profiles can also be obtained in this software from the STM topographies. Numerical data has been processed, analysed, and plotted where necessary, using Originlab (OriginLab Corporation, One Roundhouse Plaza, Suite 303, Northampton, MA 01060, USA.).

5 Self-assembly and on-surface reactions

This chapter presents the fundamental principles behind the self-assembly of organic molecules on surfaces, how it can be used as a cornerstone for bottom-up syntheses of complex nanostructures. An overview of on-surface reactions is provided, with special emphasis laid on unimolecular reactions.

5.1 Fundamentals of self-assembly

Simply put, self-assembly is the spontaneous organization of molecules into ordered structures on a surface. This requires no external stimuli, rather is driven by surface properties and intermolecular interactions. This phenomenon is non-covalent in nature, and is usually mediated by hydrogen bonds, van der Waals (vdW) and π - π interactions [13]. When molecules or even atoms are evaporated onto surfaces, nanoscale architectures are built as a result of multitudinous atomistic processes. This non-equilibrium phenomenon is governed by a competition between substrate kinetics and thermodynamics, since the primary mechanism for assembly is often the transport of molecular adsorbates on the flat terraces of substrates [62]. This transport involves lattice site hopping [63], meaning that diffusion barriers have to be overcome when going from one adsorption configuration to another [64], till the molecule finds one that is energetically favourable.

Typically, the diffusivity D , is expressed in Ångström scale as the mean square distance travelled by any adsorbed species per unit time and follows the Arrhenius law [64]. Let us now consider a typical experiment, wherein molecules are being evaporated onto a substrate, at a deposition rate of F , usually expressed as Ångström per second. The average distance that the molecule will have to travel to meet another molecule will be given by the ratio, D/F . This could be the site of nucleation or it could also mean the continuation of an already forming island. Therefore, this ratio and the rate of deposition are vital parameters in understanding and tuning growth kinetics. For example, if molecules are deposited slower than the diffusion rate, meaning a large D/F ratio, the self-assembly proceeds at equilibrium conditions, i.e., molecules will have enough time to traverse the potential energy landscape to reach the minimum energy configuration. This is the principle of hot deposition that has been used in our experiments, and will be discussed in the next chapter.

The other case, where deposition proceeds faster as compared to the diffusion rate, signifying a small value of D/F , then the self-assembly is dominated by kinetics and individual processes, which can lead to adsorption configurations that are often metastable and can be switched into other conformations. This is what we often find with low-coverage samples, leading to the possibility of molecular manipulations and tuning the intra and intermolecular interactions. This has been explored in great detail in Chapter 7.

5.2 Surface interactions

As mentioned in the previous section, the origin of self-assembly on a surface can be explained via three types of interactions.

- Hydrogen bonds: This is usually the interaction between hydrogen atoms and neighbouring electronegative atoms, like oxygen. This of course also works when these atoms are incorporated in a molecule. Therefore, the self-assembly of acceptor and donor-acceptor type molecules that has been shown in Chapter 5 and Chapter 6, are understood to be governed by this interaction.
- vdW interactions: This is within the purview of electrostatic and electrical interactions between molecules [65], and is also often the predominant interaction governing tip-based manipulations of molecules, as shown in Chapter 6.
- π - π stacking: This pertains to the attraction between aromatic rings, very common in organic molecules and conjugated systems. Indeed, we believe that the stacks of long acenes that we observe, as is shown in Chapter 8, is an example of this.

It must be noted that it is often a combination of the aforementioned interactions that causes a specific kind of on-surface self-assembly, and not just one. Therefore, it is very difficult to predict how molecules will arrange themselves, something that some on-surface reactions are predicated upon. This has been discussed in detail in Chapter 6. A very recent paper shows that even the magnetic properties of molecules can be affected, depending on the way they self-assemble on a lead substrate [15].

A simple schematic showing the principle of self-assembly is illustrated in Figure 12.

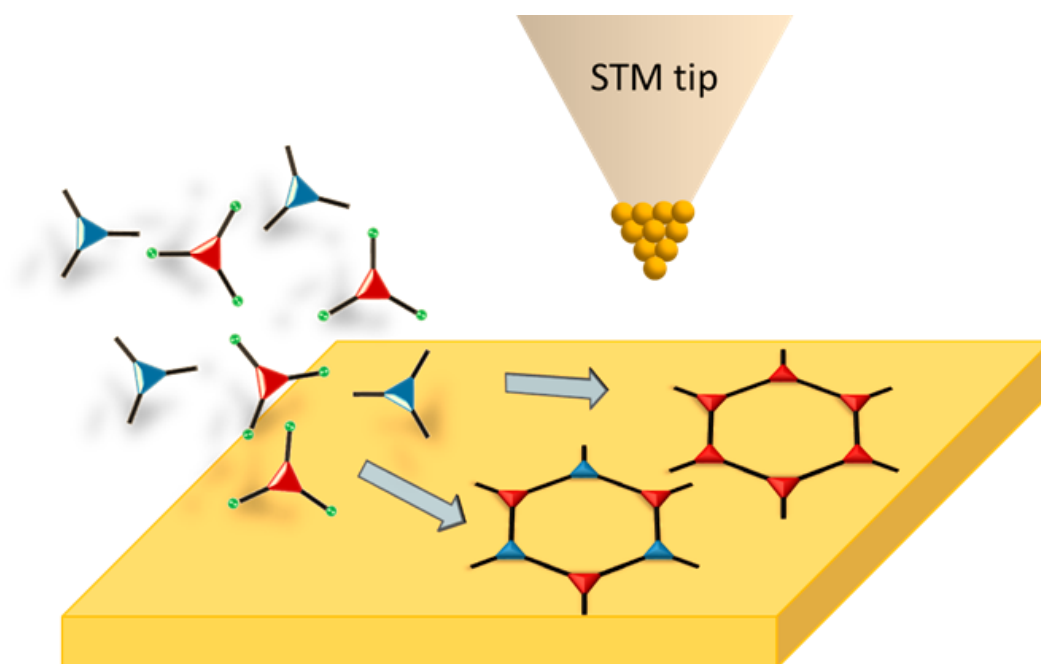


Figure 12: Schematic showing an example of self-assembly on a surface.

5.3 Donor-acceptor type molecules

Since most of the molecules presented in the next two chapters are donor-acceptor (D-A) type, a quick and concise introduction is presented here. This class of molecules are very attractive for organic and molecular electronics, photovoltaics and light emitters since they have interesting optoelectronic properties [66, 67]. They incorporate a donor, or electron-rich moiety, and an acceptor that is an electron-poor moiety into one molecule. Once deposited on the surface, we have means of controlling the initiation step of the donor-acceptor building blocks, i.e., the mediating reaction and its degree of advancement in terms of reaction yield. Furthermore, we can characterize the structure, position and orientation of these D-A molecules, glean information on the viability of covalently bonded polymers, to create two-dimensional covalent organic frameworks (2D-COFs).

Probing the properties of the individual molecules and if successful, the formed networks through LT-SPM techniques makes possible bettering rational design principles. This interdependency between probed molecules on surfaces and design philosophies has been summarized in the image shown in Figure 13.

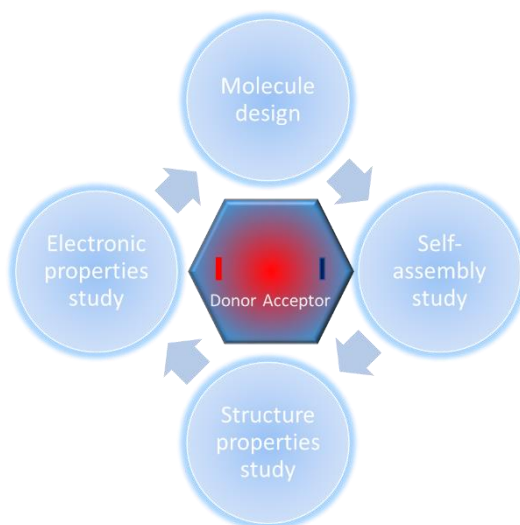




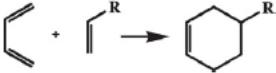
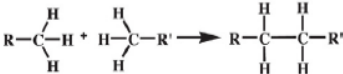
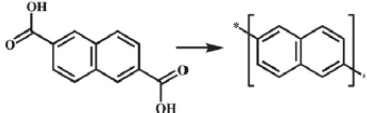
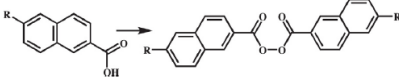
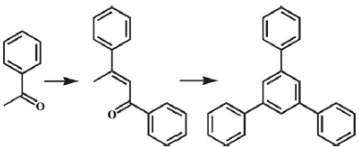
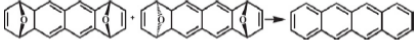
Figure 13: Relationship between on-surface investigations and rational design.

5.4 On-surface reactions

It is clear that we can use the STM tip to probe adsorption geometry, structural and electronic properties and even induce changes in the afore-mentioned by tip-based manipulation techniques [36]. An extremely powerful tool also at our disposal is to trigger reactions on the surface [7, 8, 68]. There is a plethora of advantages to this; unprecedented access to reaction mechanism, sub-molecular level resolution, and importantly, promoting reactions not possible with conventional solution chemistry [69, 70].

Since this is an ever-burgeoning field of study, a summary of common on-surface reactions is provided in the table below.

Type	Reaction Name	Chemical Equation
SP ⁰ -C	N-heterocyclic carbenes: Formation and dimerization	
	Glaser coupling	
SP ¹ -C	Alkyne cyclotrimerization	
	Metalated carbene	
	Bergman Reaction	
	Azide-alkyne cycloaddition	
SP ² -C	Sonogashira coupling	
	Dehalogenative homocoupling of alkynyl bromides	
	Ullman coupling	
	Aryl-aryl dehydrogenation coupling	

Type	Reaction Name	Chemical Equation
SP ² -C	Dehydrogenative homocoupling of terminal alkene	
	Dehalogenative homocoupling of terminal alkenyl bromides	
	Diels-Alder reaction	
SP ³ -C	Wurtz coupling	$R-X \longrightarrow R-R$
	Linear alkane polymerization	
Carboxylic acid/ester/ether/acetyls (C-O, C=O)	Decarboxylative polymerization	
	Dehydrogenative coupling	
	Dimerization and cyclotrimerization of acetyls	
	Dealkylation of ethers to alcohols	$R-O-R' \longrightarrow R-OH$
	Reduction	
	Schiff-base reaction	$R-C(=O)H + H_2N-R' \longrightarrow R-C(=N-R')H$

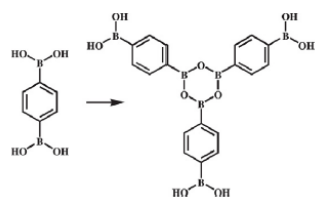
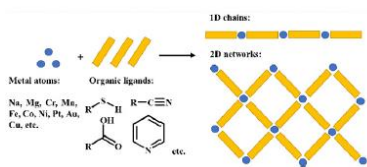
Type	Reaction Name	Chemical Equation
Others	Boronic acid condensation	
	Surface confined metal organic coordination	

Table 1: Types of on-surface reactions. Adapted from [68].

The principle of on-surface reactions is using the solid substrate as a two-dimensional confinement to create new molecular species, hitherto unachievable or impractical through conventional chemistry. Additionally, operating in a solvent-free and ultra-clean UHV environment, the purity of reaction products is at the atomic level. But the most attractive proposition is undoubtedly the fact that we can explore new reaction pathways that are contingent on the substrate-molecule interactions and directly characterize each step in sub-molecular resolution in real space.

When it comes to the low-dimensional molecular structures, on-surface synthesis via bottom-up approach has the potential to not only create long-lived stable molecular species, but also to provide specific functionalization with regards to well-controlled properties [71]. To name a couple, electron transport for devices, for example with D-A type molecules [72], and frustrated spin magnetism with exotic superstructures like Kagome lattices [73]. Another benefit is also the possibility to steer dimensionality by careful precursor design, as shown by Grill et. al [74].

Furthermore, thanks to the confinement of the reaction in a two-dimensional rigid template that is the surface, new reaction pathways have opened up and even inert bonds like C-H have been shown to be activated by the use of an aromatic core. By depositing the molecules at different surface temperatures, it was shown that not only can this bond be activated but also has very high yield of 99% [75].

Another highly promising avenue to explore is hierarchical covalent linkages. This utilizes the difference in bond strengths of different carbon-halogen substitutions to steer the polymerization degree and direction. By first activating one dehalogenation reaction and then sequentially triggering the other through annealing steps, a 1D polymer chain could be converted to an ordered 2D network [76].

Usually when one talks of on-surface reactions, it is either about cleaving functional groups to create new bonds, bond reordering or closing. But there is also a converse possibility of ring-opening polymerization, where molecules can be unfurled like origami to make completely new low-dimensional materials [77]. In general, the success of on-surface synthesis towards larger nanostructures is gauged by the degree of order achieved by the polymeric network. This is driven by a fine balance between precursor diffusivity and reactivity, both of which will ultimately depend on the substrate nature. Therefore, a lot of effort has been expended upon studying the surface modulation effects on bottom-up syntheses, for example, to show that silver substrates are better for long-range order than gold [78-80].

5.5 Ullmann Coupling

Ullmann coupling is possibly the most successful migration of in-solution techniques to on-surface coupling reactions and therefore this section has been dedicated to it. First described for solution chemistry in 1904 [81], it took less than a hundred years for its pioneering demonstration on surface, in the year 2000 [7]. It is quite straightforward and involves halogenated precursor molecules being deposited onto a surface and undergoing dehalogenative C-C covalent coupling, either through thermal energy or through tip-based techniques [8]. The reaction mechanism is illustrated in Figure 14.

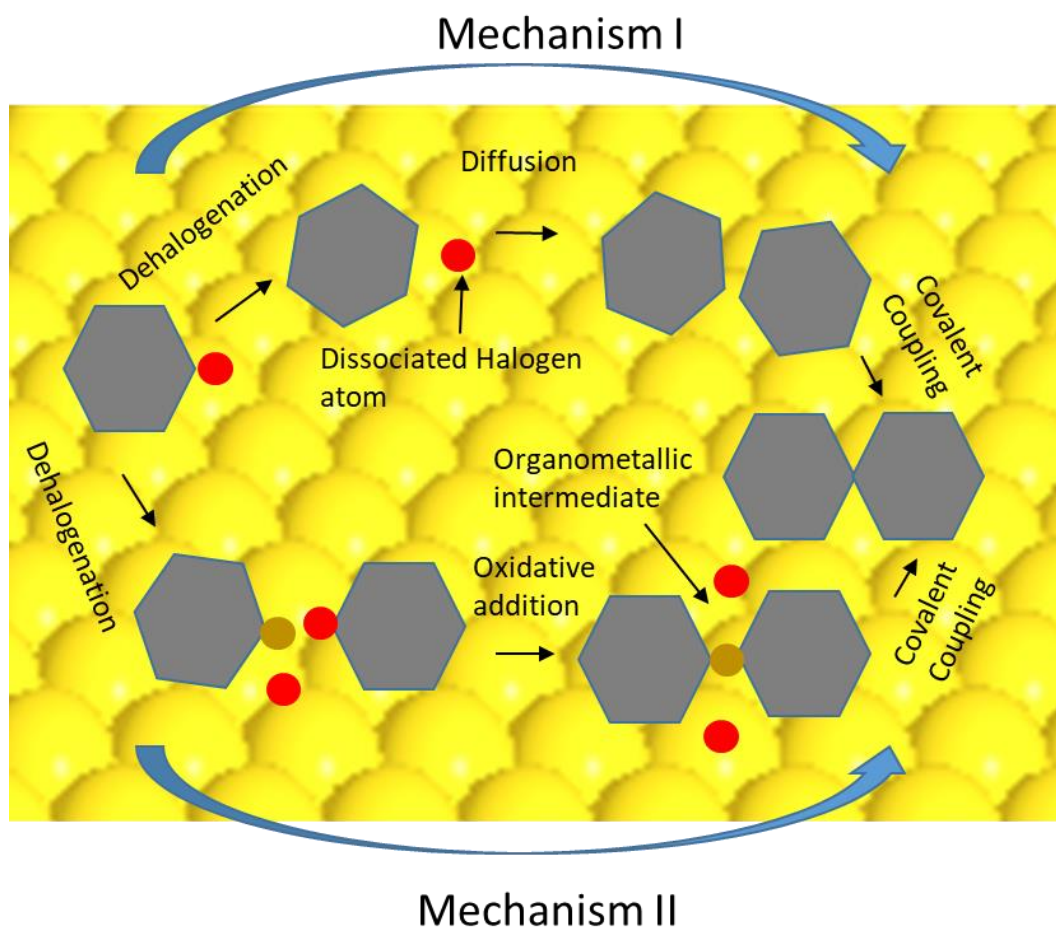


Figure 14: On-surface synthesis via Ullmann coupling.

This reaction was used successfully for the first bottom-up synthesis of graphene nanoribbons [12], and became the coupling reaction of choice for much of the on-surface syntheses of low-dimensional carbon-based nanostructures [82]. The synthetic route suggested for one of the molecules shown in Chapter 6 towards 2D-COFs was also Ullmann coupling mediated.

With the help of rational design, substrate choice, regioselectivity and other factors discussed above, more novel reactions towards complex nanostructures can be realized on the surface. The next section will focus on unimolecular reactions, by both tip-based and thermal techniques since this forms a significant part of Chapter 8.

5.6 Overview of unimolecular reactions

The seminal work performed by Hla *et al.*, showing that all steps of a chemical reaction could be executed using an STM tip [7], kickstarted the rich field of on-surface synthesis of elusive, reactive, or otherwise hard to access molecules [83]. This section will be an overview of the advances made in this field, and the considerable efforts that are still being expended.

To be able to directly visualize single bond formation, sounds like science fiction, but was executed using a pentacene molecule and a gold atom on an NaCl film by Repp *et al.*, in 2006 [84]. They were able to exploit manipulation techniques available in LT-SPM to create and study different structural isomers by bringing together the molecule and metal atom in various configurations. Both weak coupling arising from proximity effects of the π -conjugated molecule and metal atom, and covalent interactions due to the formation of metal-organic complexes were studied topographically and electronically.

The 2015 paper demonstrating how individual arynes could be generated on an ultrathin insulating film by LT-STM and AFM, provided valuable insights into not only the chemistry of the final product, but also on elusive intermediate products [85]. A couple of years before that, the direct imaging of covalent bonds in single molecule reactions was pioneering work conducted using nc-AFM, illustrating in real space the mechanisms involved in the thermally induced cyclization of enediyenes [86]. In a similar vein, the catalytic properties of a Cu(111) surface were explored by thermally instigating a sequential multi-step dehydrogenation of a hydrocarbon [87]. Going a step further in dehydrogenative reactions, the origin of regioselectivity was unambiguously illustrated via nc-AFM images of pyrazine and pyridine moieties, showing a preferential activation of the former, as compared to the pyridine species [88].

Using nc-AFM in combination with STM/STS techniques to structurally and electronically characterize the reaction steps from monomer to 1D oligomers was successfully demonstrated in semiconducting π -conjugated polymers, and showed how the extended π -conjugated states are much lower as compared to their single monomer units [89]. The first molecule presented in Chapter 8 is investigated similarly, starting from the precursor monomer to the final reacted monomer, both structurally via BR-nc-AFM and electronically with high-resolution differential conductance maps and STS.

While nc-AFM is better suited to planar molecules and nanostructures, researchers have demonstrated the remarkable use of tip-based dehydrogenation via voltage pulses, to convert a non-planar, and therefore not well-resolved molecule, into a

completely planar and 2D naphthodiazaborinine molecule, that could then be imaged successfully [90]. The molecules in the next chapter have been similarly dehydrogenated in one case, and partially deoxygenated in the other, using tip-induced voltage pulsing.

Furthermore, when it came to coupling reactions like aryl-aryl recombination, much of the reaction steps were impossible to study, since the initial activation of the C-H bond dehydrogenation was energetically demanding, therefore most intermediate steps, although theorized, were thought to be beyond the reach of experimental proof [91, 92]. However, recently, researchers have been able to decipher this very mechanism, thanks to the careful design of the precursor and LT-SPM techniques [93].

Cyclo[*n*]carbons are yet another tantalizing class of molecules which could not be fully studied or isolated due to their extremely high reactivity. That is, until researchers used voltage pulses from an AFM tip to sequentially remove CO moieties from their precursor molecule adsorbed on a thin layer of NaCl and conclusively show what kind of bond ordering is preferred by these molecules [94]. Pulse-induced cleaving of bonds can not only generate new species of molecules, but also rearrange the skeletal chemical structure, so to speak. This was demonstrated in the on-surface conversion of alkenes to polyynes on an NaCl surface via radical formation and reductive rearrangement, adding to the toolbox for the synthesis of molecules through atomic and molecular manipulations [95].

It must also be mentioned that on-surface synthesis and characterization is not just limited to organic molecules, but is equally robust as a technique for inorganic molecules. The recent on-surface generation of cyclotriphosphazene, the inorganic aromatic analogue of benzene, which is a very short-lived species, via voltage pulse induced sextuple dechlorination, is a good example of this [96].

In short, the inherent benefits afforded by a UHV environment and the degree of precision that is available in SPM techniques, make the field of on-surface synthesis both exciting but simultaneously challenging, since we are often limited by surface-modulated reaction dynamics, self-assembly driven regioselectivity and unpredictable reaction intermediates that diminish the yield of target molecules. This thesis aims to discuss both by providing insights into molecular behaviour on surfaces.

6 Self-assembly of organic molecules on Au(111)

Investigating how molecules adsorb on a surface after thermal deposition, is the first step in probing their viability as precursors for covalent structures. This chapter will focus on the self-assembled structures of two different molecules, and the mitigating effect it has on the bottom-up synthesis of covalent organic frameworks (COF).

6.1 Molecule 1: Acceptor type molecule- HATN

Synthesized in the group of X. Feng in TU Dresden, called 2,3,8,9,14,15-hexabromodiquinoxalino[2,3-a:2',3'-c]phenazine, or HATN-6Br in short, is a nitrogen-containing molecule of the acceptor type, terminated by Bromine atoms in order to promote Ullmann coupling mediated 2D-COF. The molecule, which is symmetric is shown in Figure 15.

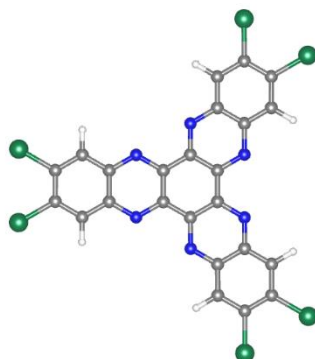


Figure 15: Chemical structure of the precursor. Carbon atoms shown in grey, nitrogen in blue, bromine in green and hydrogen in white.

6.1.1 Surface after deposition

The molecule is evaporated onto Au(111) kept at RT, using a Knudsen cell and is found to have a high sublimation temperature of 415°C. Upon deposition, the molecule self-

assembles in large islands, with domains formed by two different molecular arrangements.

Figure 16 shows a large area STM topography of two kinds of molecular islands, with the herringbone reconstruction of the substrate clearly visible. This is indicative of a weak van der Waals type interaction between molecules and surface, a well-known feature of self-assemblies [13]. Figure 17a shows an ordered island with hexagonal and square patterns among other complex arrangements. Figure 17b is less daunting, with the island formed by zigzag and square packing geometry.

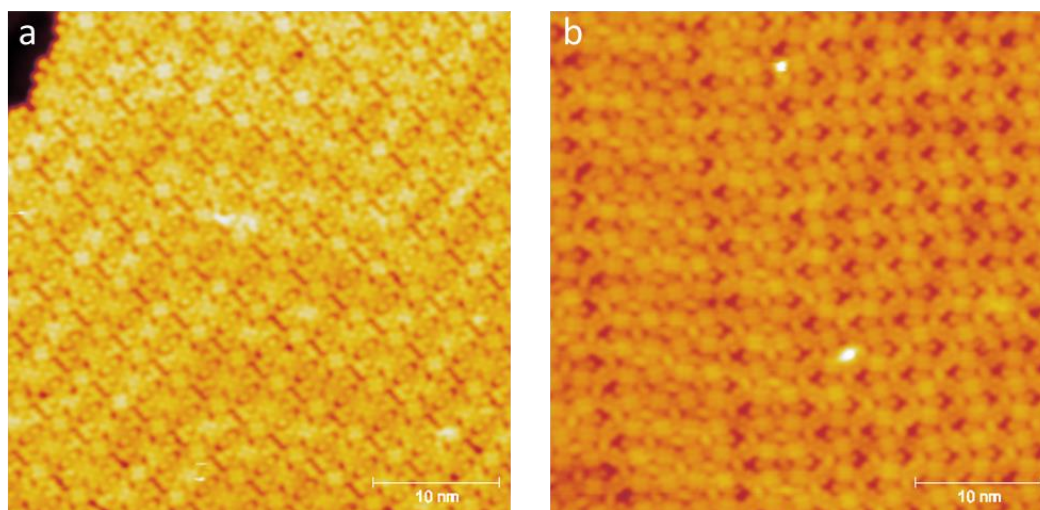


Figure 16: (a) Island with mixed hexagonal and square patterns. (b) Island with only square pattern. Image parameters: (a) and (b) $V = 0.5$ V, $I = 10$ pA, size: 40 nm^2

While adequately charming to look at, at this size resolution, it is difficult to understand the origin of these intricate patterns. A smaller area image, accompanied by a schematic representation of the molecular arrangement makes it simpler.

Figure 17a shows a close-up of an island with a mixed hexagonal or floral, and square pattern. It is found that the six lobes of the hexagonal flower are actually formed by only four molecules, arranged as shown in Figure 17b.

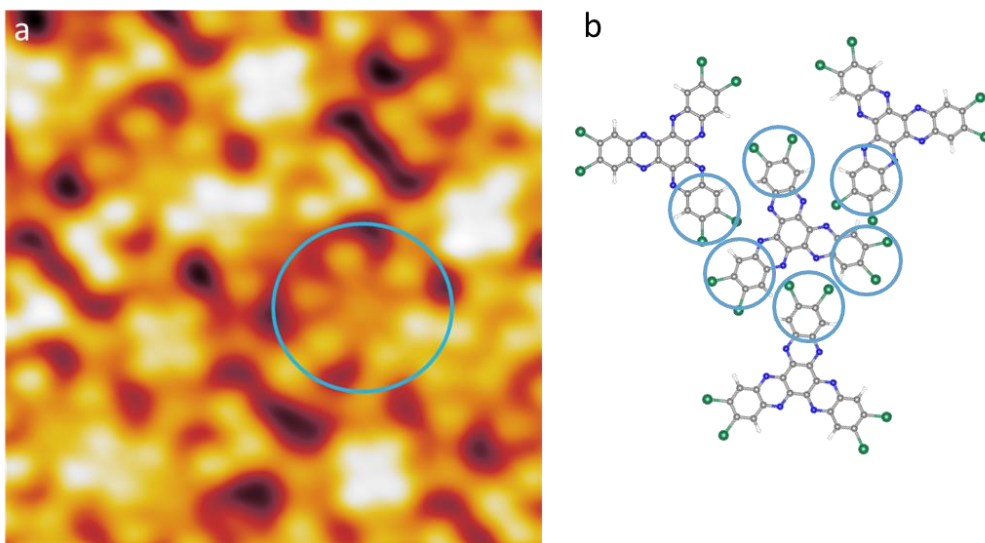


Figure 17. (a) Close-up of an island with mixed patterns. (b) Schematic representation of proposed molecular arrangement shown in the blue circle. Image parameters: $V = 0.5$ V; $I = 20$ pA; size : 8nm^2

If we repeat this image analysis on an island formed by square patterns, we yet again find that the structures arise due to the ordered arrangement of four molecules, albeit, in a different packing geometry this time. This is shown in Figure 18a and Figure 18b.

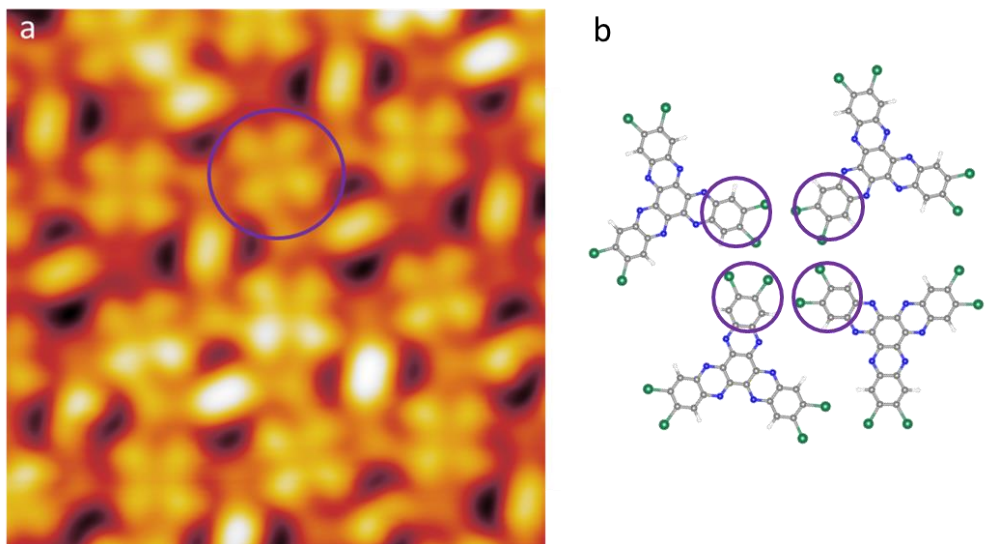


Figure 18: (a) Close-up of an island with square patterns. (b) Schematic representation of proposed molecular arrangement shown in purple circle. Image parameters: $V = 0.5$ V, $I = 20$ pA, size = 8nm^2

This sort of island conformation was present throughout the areas of the Au(111) that were scanned. Both the molecular packing geometries, hexagonal and square, were not conducive to the desired pore geometry of the extended 2D-COF (as shown in Figure 19), since surface assisted Ullman reactions necessitates first the dehalogenation of the precursor, and then the polymerization, leading to covalent structures. In our case, the bromines terminating the molecule are always facing the nitrogen doped core of the molecule, rather than an orientation that is end to end. The hexagonal packing geometry fares slightly better in this respect, but for the 2D COF to have any kind of long-range order, the molecular self-assembly must follow an exact design.

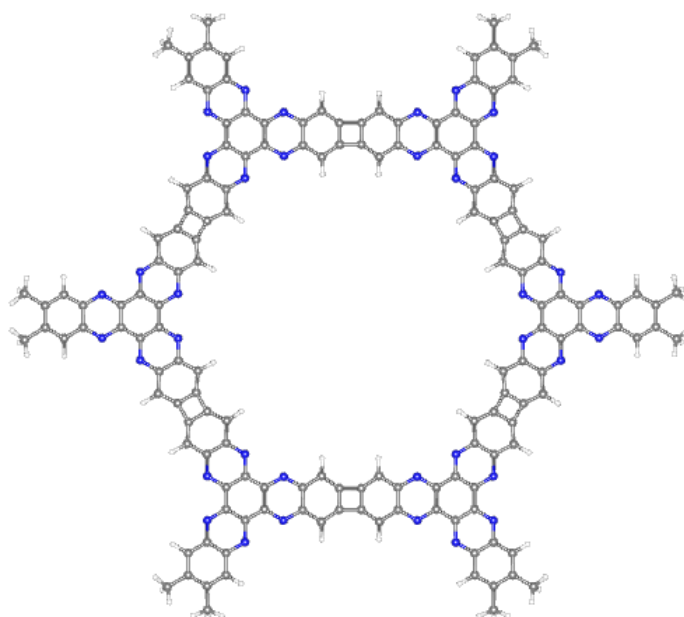


Figure 19: Pore geometry of 2D-COF

This is indeed what we find upon post-annealing the surface to 240°C for 10 minutes. There is substantial desorption already at this temperature and while there are local and non-iterant pore geometries that almost have the desired hexagonal structure, it lacks long-range order. This is shown in Figure 20.

Figure 20a shows some reacted structures growing from the Au(111) step edge, where at least one structure has a passing resemblance to a hexagonal pore, albeit stretched. The other structures resemble zig-zag linkages and are haphazardly arranged. Figure 20b is another area on a larger terrace with a trigonal structure and more zigzag linkages.

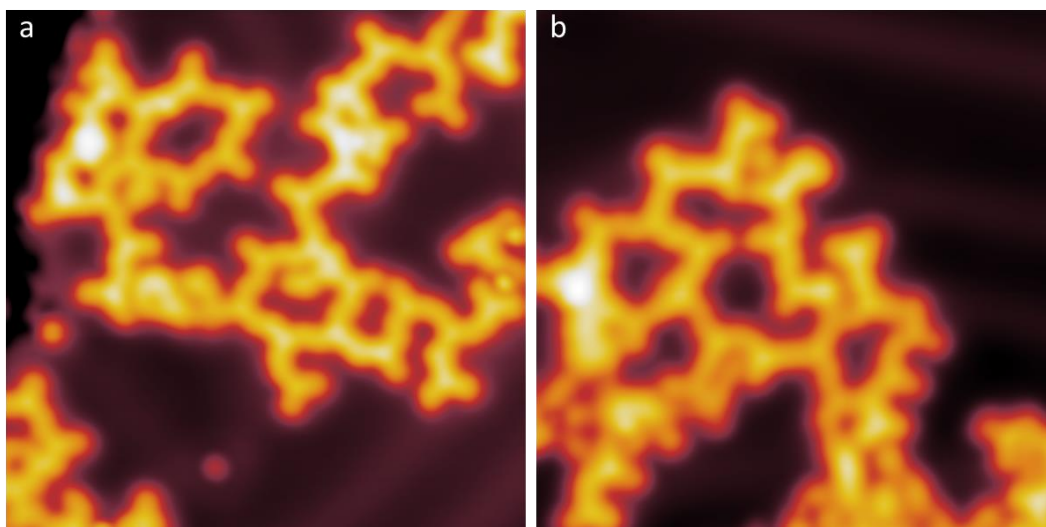


Figure 20: (a) Disordered covalent structures near a step edge. (b) Zigzag covalent chains. Image parameters: $V = 0.5$ V, $I = 50$ pA, size = 15nm^2

6.1.2 Hot Deposition

The molecules were evaporated onto a hot Au(111) surface to promote a different self-assembly and possibly trigger surface-assisted long-range order. This technique is also called direct polymerisation, since the energy from a hot surface is enough to trigger a direct coupling reaction, rather than step-wise through sequential post-annealing steps. The coverage can be controlled by keeping the evaporation temperature well below the sublimation point of the molecules, thereby ensuring long deposition times. This technique of lowering the molecular flux over an extended time has been shown to be effective when doing bottom-up synthesis [97] [98]. The figure below shows the result of one such deposition attempt, where the surface was kept at 210°C , and the molecules evaporated for 1 hour.

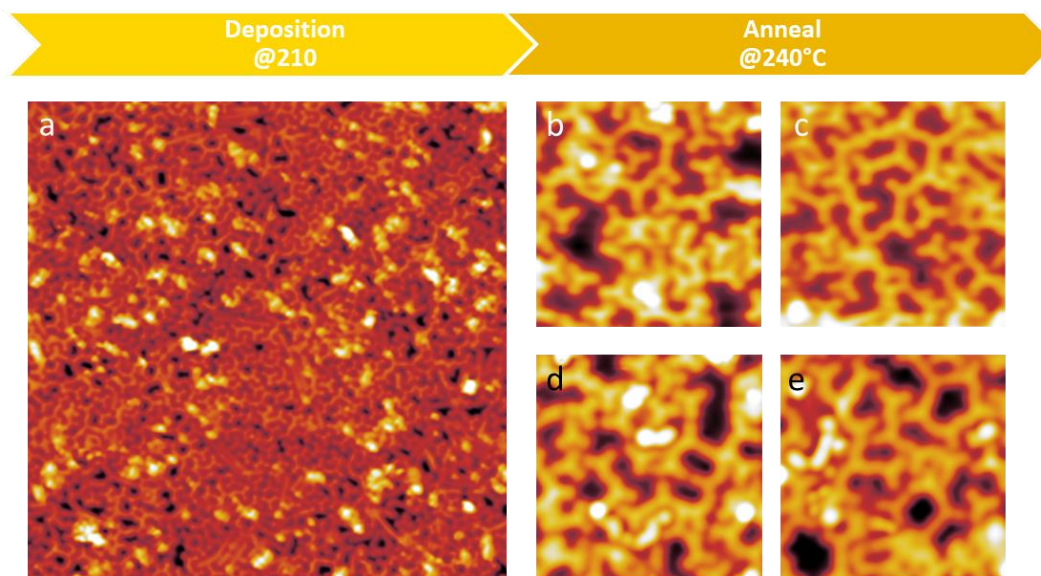


Figure 21. (a) Surface after deposition (b) - (e) STM topographies of different areas after post-annealing to 240°C, showing incomplete ring closures. Image parameters: (a) $V = 0.5$ mV; $I = 20$ pA; size = 40 nm² (b) - (e) $V = 0.5$ V; $I = 20$ pA; size = 10 nm²

Figure 21a shows the surface right after deposition. There is evidently no self-assembly and it is almost a monolayer coverage. However, it is possible to identify individual molecules, and as shown, they are densely packed within the monolayer. Upon post-annealing for 5 minutes, very little desorption is observed, but molecules have reacted to form closed pore structures. This is shown in Figure 21b-e. However, long-range order in the 2D COF is still elusive.

Therefore, we attempted to reduce coverage by lowering the evaporation temperature further, while keeping the Au(111) temperature the same. This time, the coverage was not only low, but the molecules were adsorbed far apart from each other. These results have been shown in Figure 22a. This was in contrast to both the RT self-assembly and the previous hot deposition, where the molecules had been densely packed in islands. As shown in Figure 22b, upon post-annealing, the surface does not change much and no covalent structures are observed.

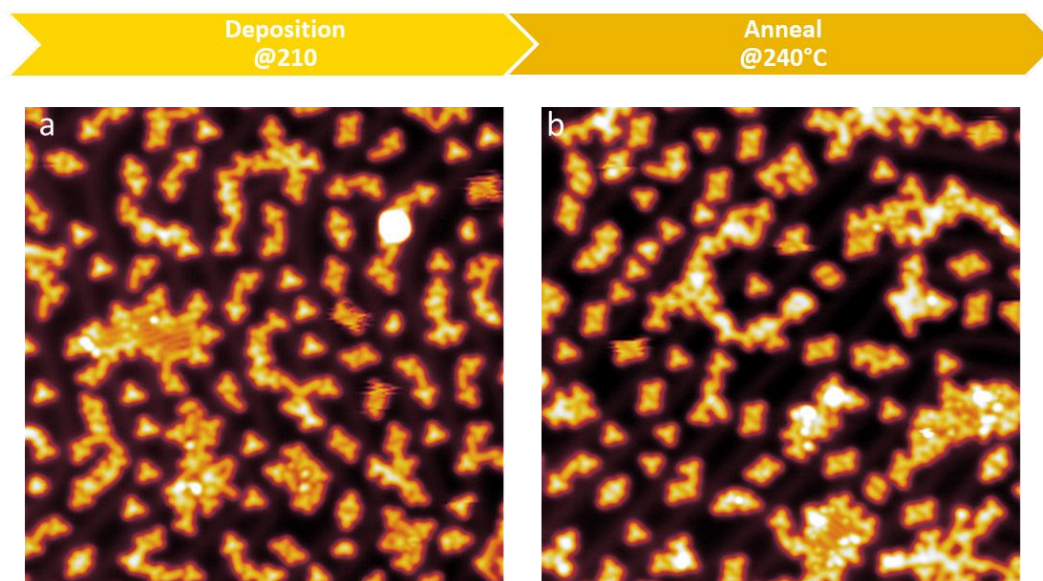


Figure 22; (a) Surface after deposition (b) After post-annealing to 240°C. Image parameters: (a) $V = 0.5$ V; $I = 20$ pA; size = 40 nm² (b) $V = 0.5$ V; $I = 10$ pA; size = 40 nm²

A summary of various deposition attempts is given in the table below. It is clear that varying the evaporation temperature by 10°C during the slow deposition/direct polymerization technique, caused a remarkable change in both coverage and packing density. On the other hand, the distinct self-assembly of the fast deposition, prevaricated the molecules from arranging in a way that would be conducive to further ordered structures. All of this empirical evidence points to the fact that this particular precursor was not suitable for the construction of a hexagonal 2D-COF.

<i>Slow Deposition</i>			
Evaporation Temperature(°C)	Substrate Temperature(°C)	Time(seconds)	Result
320	210	3600	Monolayer
280	210	3600	Very low coverage
300	220	3600	Very low coverage
300	210	3600	Very low coverage
310	210	3600	Low coverage of single molecules
<i>Fast Deposition</i>			
415(2x)	RT	30s	Islands
320	RT	30s	Nothing
330	RT	60s	Nothing

Table 2: Summary of deposition attempts

6.2 Molecule 2: Azulene based precursor

A relatively new on-surface reaction, that is more complicated than the popular Ullman coupling, is the isopropyl isomerization. So far, this has been reported once in literature, and for extended 1D structures [99]. The reaction mechanism (shown in Figure 23b) involves the selective generation of new phenylene rings, through cycloaromatization of two isopropyl substituents. This is more challenging than the comparatively simple Ullman reaction (Figure 23a), where dehalogenation followed by cyclodehydrogenation creates the final molecule.

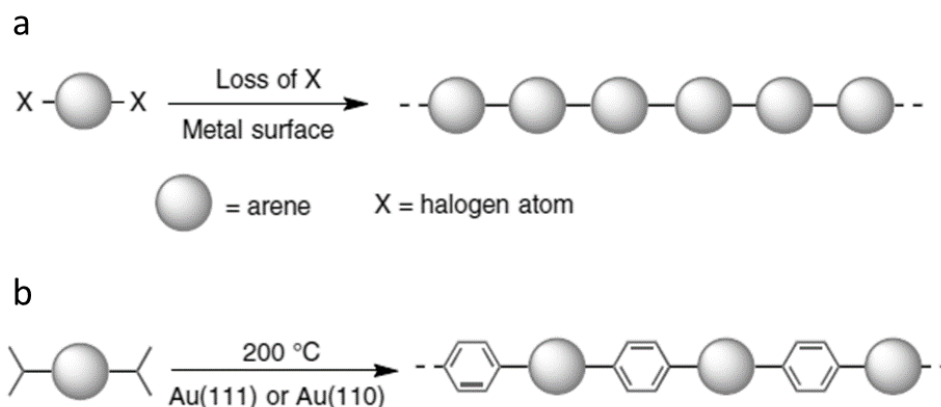


Figure 23: Reaction schematics: (a) Ullman coupling on the surface. (b) Isopropyl coupling. Adapted from [99]

Our azulene-based precursor, also synthesised by the group of Feng in TU Dresden, is more ambitious but the mechanism remains the same. Instead of a 1D chain of arenes, our goal is to create 2D-COFs, with slightly twisted hexagonal pores, as shown in Figure 25. To ensure success, the precursors must self-assemble in a six-fold symmetry, with each neighbouring molecule in an up-down orientation. This should then promote the formation of four new phenyl rings, coming from the isopropyl cycloaromatization via post-annealing.

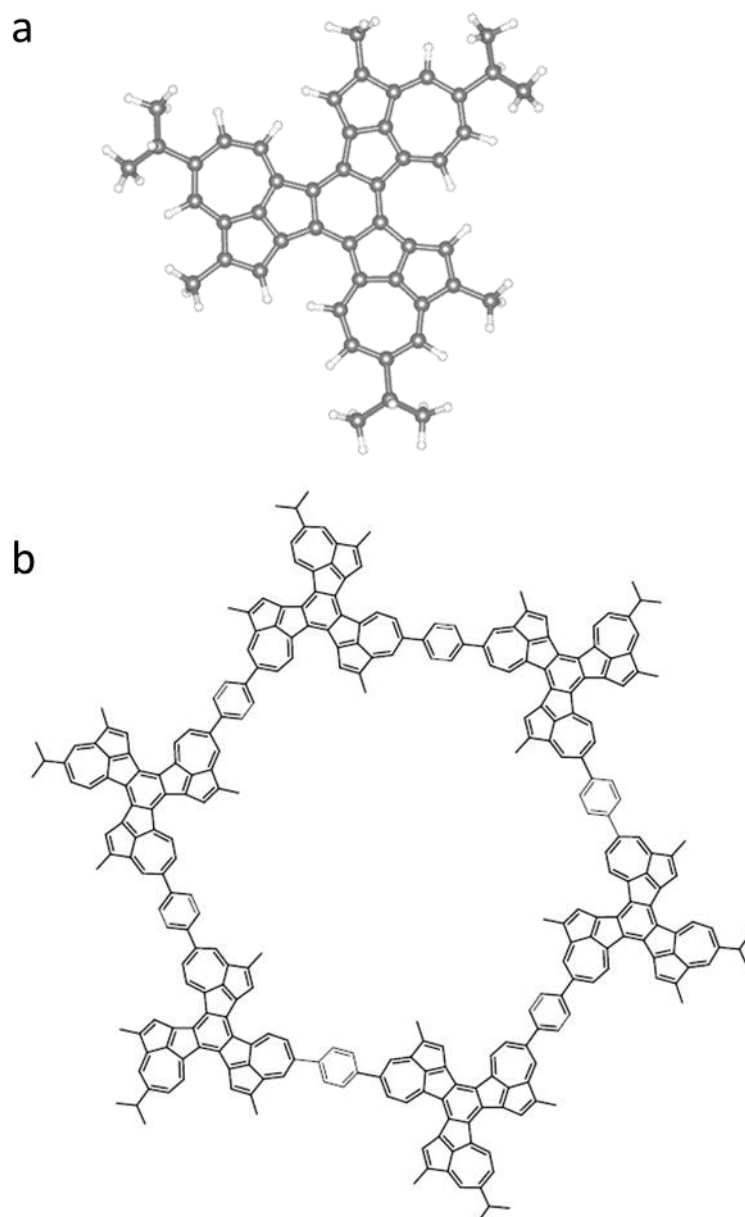


Figure 24: Chemical structure of the (a) precursor and (b) expected 2D-COF

6.2.1 Deposition on Au(111)

We note here that the molecule is chiral, and can adsorb on the surface in two chiralities, that will henceforth be called A and B (Figure 25a). The surface after thermal evaporation is shown in Figure 25b. The self-assembly seems to follow the

Au(111) reconstruction with some units formed of 6 molecules. However, in order to determine the chirality, since type A is most conducive to the hexagonal 2D-COF pore geometry, we must investigate the self-assembled structures using a CO functionalized tip. This technique, as described in Chapter 3 is used to determine and ascribe the chemical structures of molecules, since it affords sub-molecular resolution. The next section elucidates in detail the various self-assembled structures.

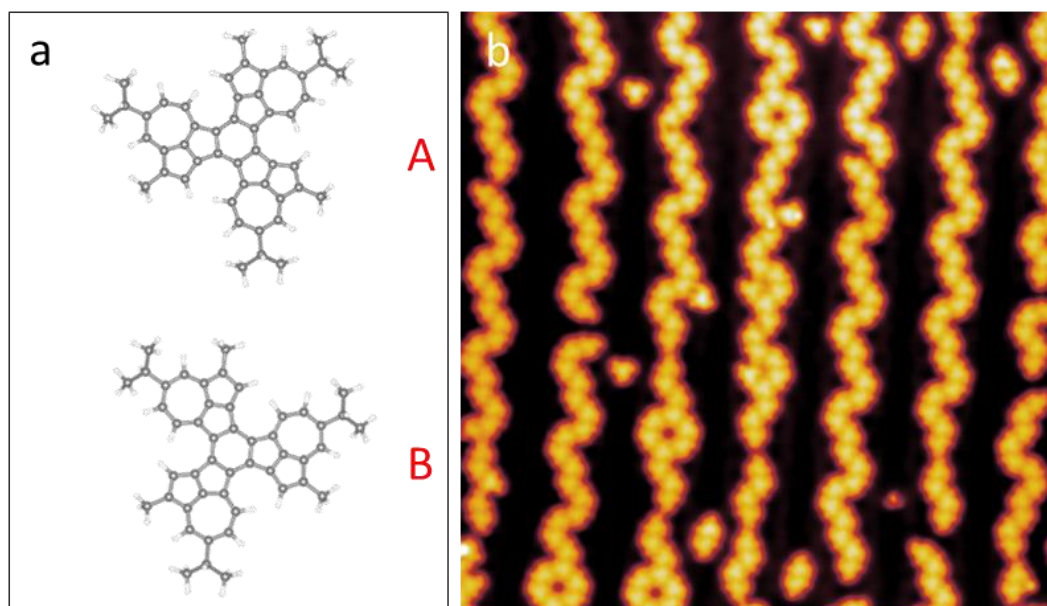


Figure 25: (a) Two chiralities of the precursor. (b) Surface after deposition. Image parameters: $V = 0.2$ V; $I = 100$ pA; size = 40 nm²

6.2.2 Constant height imaging with a CO-functionalized tip

A CO tip can improve the resolution to the extent that this method is also called bond-resolved STM (BR-STM). However, this works with planar molecules, since the imaging is conducted in the constant height mode. Too severe a non-planarity would cause a tip crash, since the feedback loop is switched off.

In the set of images below, the top row (Figure 26a - Figure 26d) shows standard constant current topographies, however, with a CO functionalized tip. Each corresponding constant height image is shown in the bottom row (Figure 26e - Figure 26h). Going from single molecule to more populous self-assemblies, it becomes apparent that the molecule is homochiral in the each assembly. This has been highlighted for each case as A or B type. Moreover, it is also possible to assign topographical features to their chemical moieties, for example, the pronounced lobes

are methyl groups that terminate the molecules. It now becomes easier to assign A or B chirality than based on just the constant current images.

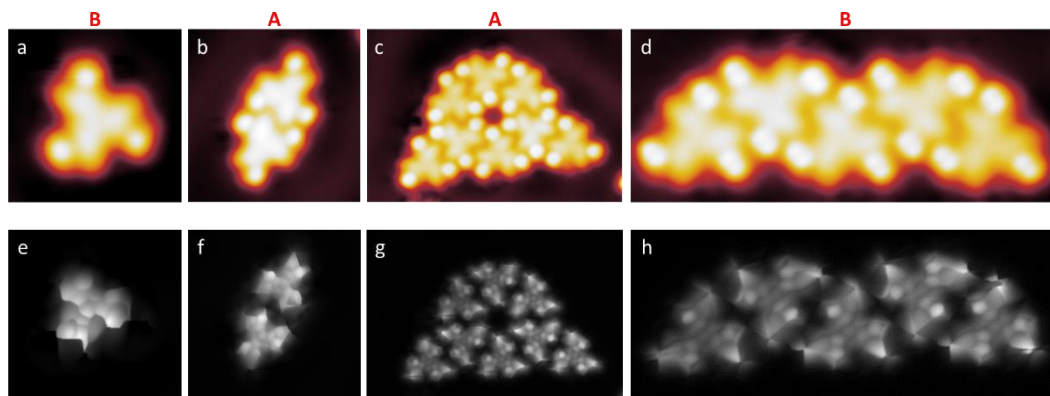


Figure 26: (a)-(d) Constant current images with CO functionalized tip. (e)- (h) Corresponding constant height images showing molecular structure. Image parameters: (a) $V = 200$ mV; $I = 20$ pA; size = 2.9 nm^2 . (b) $V = 200$ mV; $I = 20$ pA; size = 4.3 nm^2 (c) $V = 200$ mV; $I = 20$ pA; size = $8.5 \text{ nm} \times 5.7 \text{ nm}$; (d) $V = 200$ mV; $I = 20$ pA; size = $7.1 \text{ nm} \times 2.9 \text{ nm}$. (e) – (h) $V = -5$ mV.

The different self-assembled structures can be made of the other chirality as well. That is to say, the superstructures are not driven by the chirality, rather, they exist natively. A good example of this is if we look at the chain-like structure constituting four B type molecules in Figure 26d and Figure 26h, we find another structure, its mirror opposite since it is formed by four A type molecules, elsewhere. This has been shown in Figure 27.

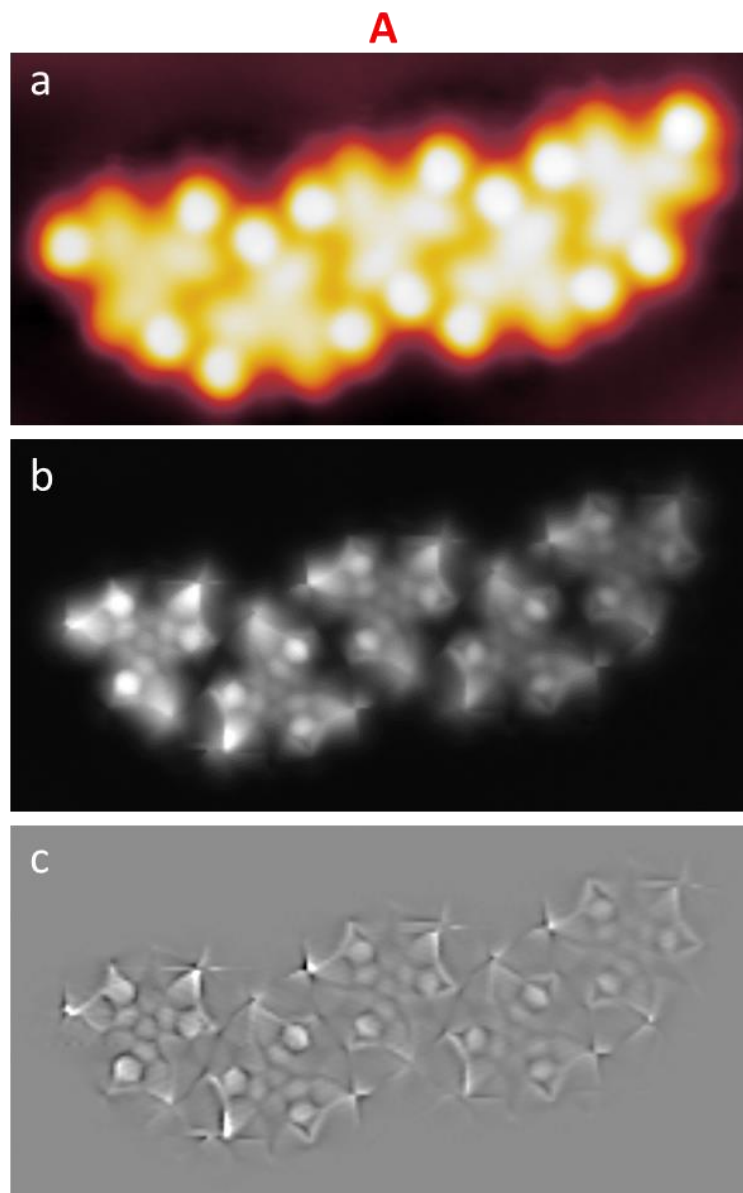


Figure 27: (a) Constant current image of chain structure. (b) Corresponding constant height image. (c) Laplace filter applied to (b), showing bond structure. Image parameters: (a) $V = 0.2$ mV; $I = 20$ pA. (b) $V = -5$ mV. Size: All images = 7.1 nm \times 3.6 nm

Among the different structures, the one shown in Figure 26c and Figure 26g, being hexagonal, is clearly the most promising. However, before moving on to post-annealing, the electronic properties of the precursor were investigated and will be described in the next section.

6.2.3 Scanning tunneling spectroscopy and conductance maps

As discussed in Chapter 2, STS is used to probe the electronic resonances of molecules, thereby elucidating on their bandgap.

This precursor being azulene based, i.e., dipolar, should show electronic states that are mostly localized at the edges, since that is where the azulene moieties are, and being a non-benzenoid nanographene with additional functionalization, is expected to be in the semiconducting range.

Our experimental results are in accord with the above hypothesis. We measured STS spectra on both a single molecule and a molecule in a chain and found that the self-assembly did not affect the electronic states. Furthermore, all molecules regardless of chirality, were found to have the same electronic properties.

Figure 28 shows the dI/dV curves of the molecule. Both isolated and otherwise, the molecule has a resonance at -0.9 V, which manifests as a small and broad peak. Above the Fermi energy, the single molecule has a broad but intense peak, the maximum of which is at 0.9 V. The molecule within the chain has an almost shoulder-like feature, with the maximum at 1.4 V. A further peak is observed at more than 2 V for both molecules. However, at such a high bias, the molecule starts moving, and therefore we will restrict ourselves to data points below this bias.

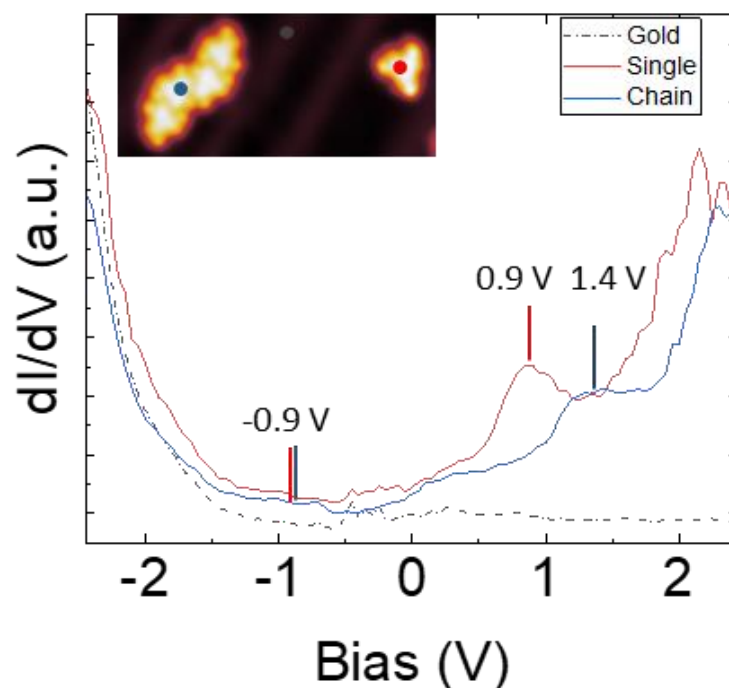


Figure 28: STS on single molecule and on a molecule in chain. Inset: $V = 0.2$ V; $I = 20$ pA; size = 12.5 nm x 5.7 nm.

To visualize the spatial distribution of the charge at the STS resonances, dI/dV maps were obtained. This has been shown in the figure below. The top row, (Figure 29a-Figure 29c) are the constant current images taken at standard bias and current. The other images in the figure are maps taken in constant current mode with higher current parameters. This has been presented in Figure 29d-Figure 29l. At both -0.9 V and 1.4 V, the states are strongly localized at the edges, with the centre being devoid of charge density, therefore appearing dark (Figure 29d- Figure 29f and Figure 29j- Figure 29l). At 0.9 V, for the single molecule, there is a contribution of the central moieties to the contrast. This is in good agreement with the STS curve shown previously, where there was an unmistakable maximum at this bias.

Therefore, the orbital ascription we suggest would be thus: the highest occupied molecular orbital (HOMO) at the resonance found at -0.9 V and for the lowest unoccupied molecular orbital (LUMO), 0.9 V is deemed accurate. This is because in both cases of the molecule, the contrast is quite well-defined, with the difference being the localization in different parts of the molecule. The bandgap then becomes 1.8 V.

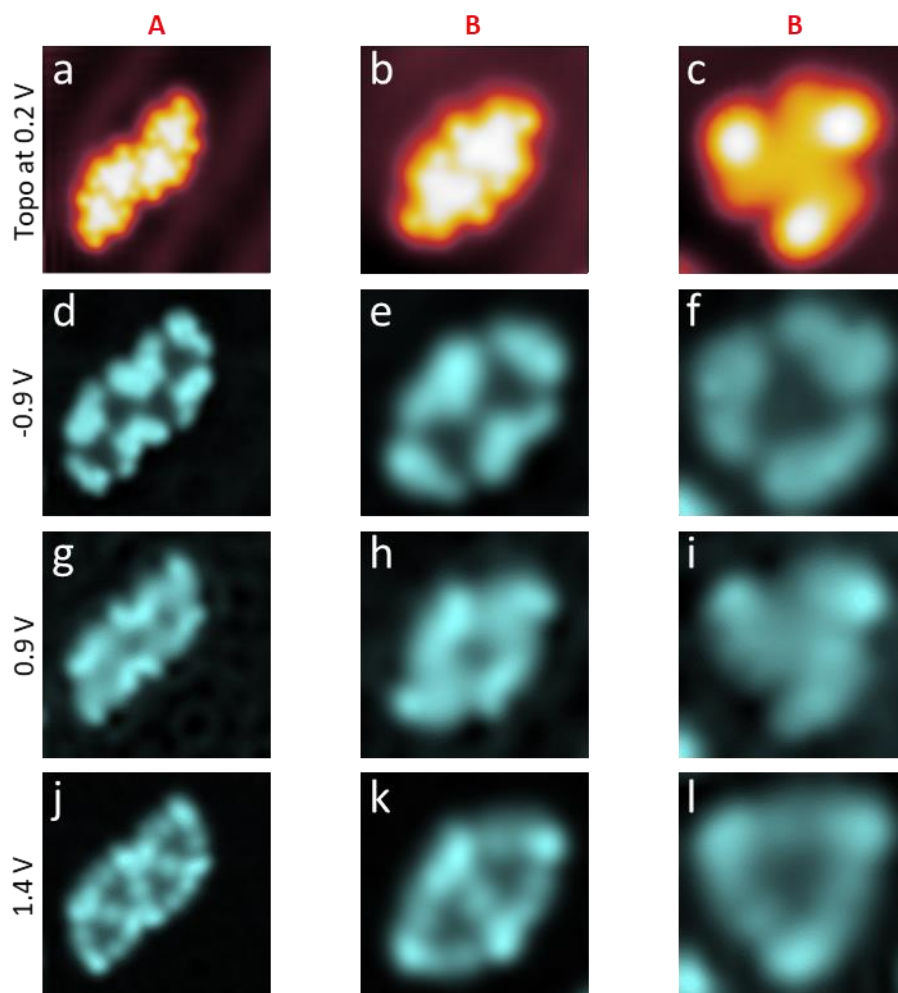


Figure 29: dI/dV maps. Image parameters: (a)-(c) $V = 0.2$ V; $I = 20$ pA. (d)-(l) $I = 200$ pA. All images size: 2.9 nm^2

After the full scope of precursor investigation, we moved on to the next step of the experiment, i.e., to trigger the isopropyl coupling via post-annealing steps. This was done in several different sets of experiments, the results shown in the upcoming section is an example of one experiment.

6.2.4 Attempts at isopropyl coupling

As clarified at the beginning of this section, the isopropyl reaction is quite complex and has so far been reported for 1D polymers. Our precursor being chiral and designed for 2D networks, added extra challenges and mitigating factors to success. The figure below shows the sequential post-annealing steps with diminishing results. Although there were sparse structures with favourable hexagonal self-assemblies, there seems to have been mostly random dehydrogenation reactions and covalent linkages between neighbouring molecules, rather than only the specific methyl groups reacting with each other. In other words, the formal cycloaromatization did not occur.

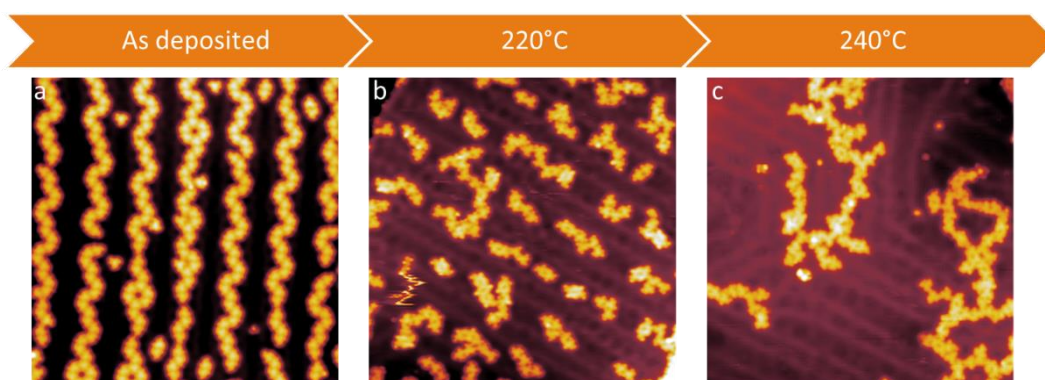


Figure 30: Attempts at surface assisted isopropyl coupling through post-annealing. Image parameters: $V = 0.2 \text{ V}$; $I = 20 \text{ pA}$, size = 40 nm^2

6.3 Summary

This chapter presents examples of how the on-surface synthesis of ordered COFs, hinges upon the self-assembly of the precursor. Undoubtedly, factors like surface kinetics vs. thermodynamics play an important role, as elucidated in the state-of-the-art literature ([13, 97, 100]), the probability of success is contingent upon rational design promoting ideal self-assembly. As demonstrated, this is the case for Ullman-assisted reaction for a symmetric molecule, and the more challenging, isopropyl reaction with an asymmetric, chiral molecule.

The difficulty lies in predicting what a precursor might do on the surface, but often the results are illuminating with regards to the fundamental properties of molecules. This will be the subject of the next chapter.

7 Molecular manipulations in self-assemblies

This chapter examines how tip-based manipulation can be used in self-assemblies to address molecules and induce conformational change. In the first part, the effect of intermolecular interactions on the planarity of thianthrene-based molecules adsorbed in two different kinds of self-assemblies has been studied. We find that in the island self-assembly, the molecule adsorbs in a non-planar fashion, due to next nearest neighbour interactions. In the second kind of self-assembly that resembles chains, the same molecule is discovered to be planar. By using the tip to modify the number of neighbours surrounding the non-planar molecule in an island, thereby tuning the intermolecular interactions, we can also alter its conformational geometry, i.e., switch it to planar. The latter part of this chapter focuses on a thiophene-based molecule, which also adsorbs in large self-assembled islands, but here we discover a conformational change due to the surface-mediated chirality and intramolecular interactions, rather than intermolecular interactions. We use the tip to first isolate the molecules and then, via voltage pulses, induce reversible conformational switching between the two chiralities. Parts of the text and figures are reproduced with permission from our published work [5] and [14].

7.1 Thianthrene and next nearest neighbour interactions

The discussion in the previous chapter considered one aspect of self-assembled molecules, i.e., it is often a limiting factor in on-surface syntheses. However, another intriguing point is the effect of self-assembly on the molecule itself. The next section will show, how the planarity of a molecule is affected by the interaction with its nearest neighbours. We will also show how the planarity can be tuned by modifying nearest-neighbour interactions. The molecule in question is a thianthrene-based molecule, that is non-planar in its crystalline form [101], but we find that it exhibits planar as well as non-planar adsorption geometry on Au(111). Interestingly, we find that with high coverage, the molecules preferentially adsorb in large islands, in the non-planar configuration, while in lower coverages, there is an emergence of planar molecules, in quasi-1D chains, coexisting with the non-planar island geometries. Tip-based manipulation techniques have been employed successfully to switch the planarity, and the effect it has on the electronic properties of both configurations has been studied using STS.

7.1.1 Design of the molecule

This work was done in collaboration with the Kaskel group from TU Dresden, who synthesized the molecule. They recently reported the creation of a 2D layered COF from 2,3,5,6-tetrafluoroterephthalonitrile and triphenylene-2,3,6,7,10,11-hexathiol, in which the organic building blocks are linked through dithiine bridges [101]. Unlike, the structurally closely related dioxins [102] or phenazines [103], the dithiine unit is non-planar with a C-S-C dihedral angle of 101° [14, 101]. In addition to the dithiine linked framework structure, a model compound featuring two dithiine units was isolated from the reaction of 2,3,5,6-tetrafluoroterephthalonitrile and benzene-1,2-dithiol.

This second molecule, shown in Figure 31, benzo[5,6][1,4]dithiino[2,3-b]thianthrene-6,13-dicarbonitrile (bTEpCN), will be the focus of this section.

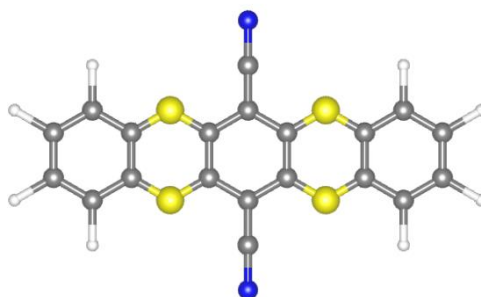


Figure 31. bTEpCN chemical structure. Carbon atoms shown in gray, Hydrogen atoms in white, Sulphur atoms in yellow and Nitrogen atoms in blue.

The gas phase bTEpCN molecule was found to be non-planar (Figure 32a), having a C-S-C dihedral angle of 120° (Figure 32b). With these parameters, the crystal structure could be solved as is shown in Figure 32c [104].

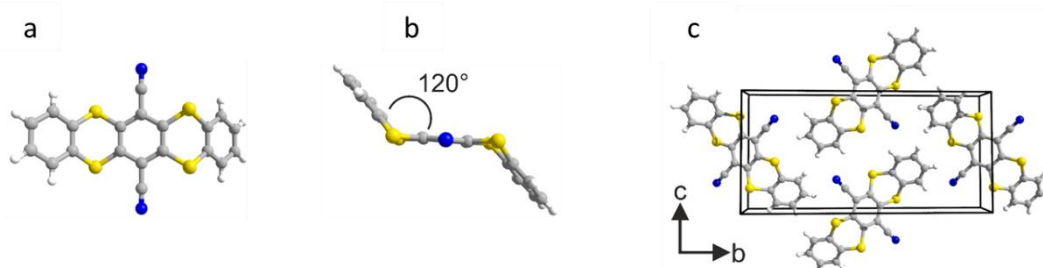


Figure 32: bTEpCN crystal structure: (a) Top view of a single bTEpCN molecule in the crystalline structure. (b) Side view of the bTEpCN molecule, showing the non-planarity in the crystal structure. (c) Packing geometry of the bTEpCN molecules in the crystal structure. Figure adapted from [14].

A quick foray into literature will show us that the planarity of polycyclic molecules such as bTEpCN, has been investigated for many years, due to the fact that it influences the aromaticity of π -conjugated systems [105-108]. In non-planar molecules, bond angle strain can be introduced via heteroatoms or overcrowded structures [109, 110], which causes geometric deformation of the molecule, leading to a bending of the π -system. In a few cases, such non-planar aromatic structures maintain their π -conjugation, with additional advantages. For example, limiting aggregation causes quenching, providing stability and novel electronic properties, valuable in applications for organic energy storage systems and in organic electronics [101, 111]. Therefore, to probe the behaviour of bTEpCN on a surface, might be fruitful in understanding the relation between geometric and electronic properties of this class of molecules.

7.1.2 Deposition on Au(111)

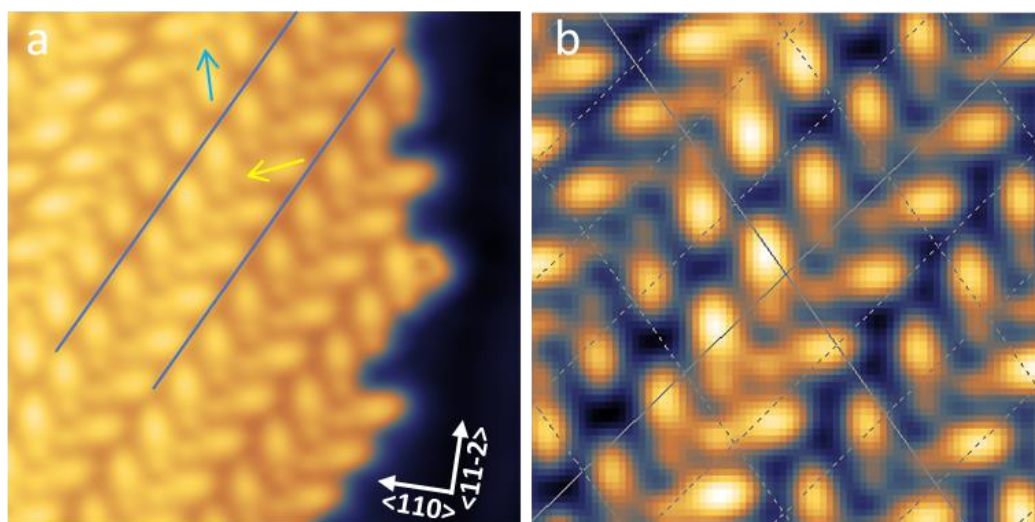


Figure 33. Self-assembled molecular islands consisting of bTEpCN molecules adsorbed on Au(111). STM images (a) 10 nm x 10 nm and (b) 5 nm x 5 nm showing the unit cell were taken at $V = 0.2$ V and $I = 20$ pA. The blue lines in (a) show the stripe-like self-assembly, while the blue and yellow arrows show the two orientations of the molecule.

The bTEpCN molecules were evaporated at 240 °C onto an Au(111) substrate kept at RT. The surface after deposition is shown in Figure 33. An overview STM topography (Figure 33a) shows well-ordered self-assembled islands growing from the step edges of the Au(111) surface. These can be further resolved as stripes (highlighted by blue lines in Figure 33a) running over the characteristic herringbone reconstruction lines. These stripes are formed by molecules arranged in two directions as indicated again in Figure 33a, with blue (up) and yellow (down) arrows. There is no selectivity as to the preferred direction ($\sim 50\%$). The image also shows that the molecules have a pear

shape, with a smaller differentiated lobe at one end, and a larger, elongated feature at the center, suggestive of an asymmetric non-planar conformation. Figure 33b shows a close-up of an area inside the island with the unit cell superimposed on it. Based on this unit cell, we find that the angle between two molecules is 81° , while the intermolecular distance measured between the center of one molecule to another in the same orientation is 1.1 nm.

DFT calculations were performed to understand the geometric properties of this densely packed structure. All calculations in this section and the next, were performed by D. Ryndyk in TU Dresden.

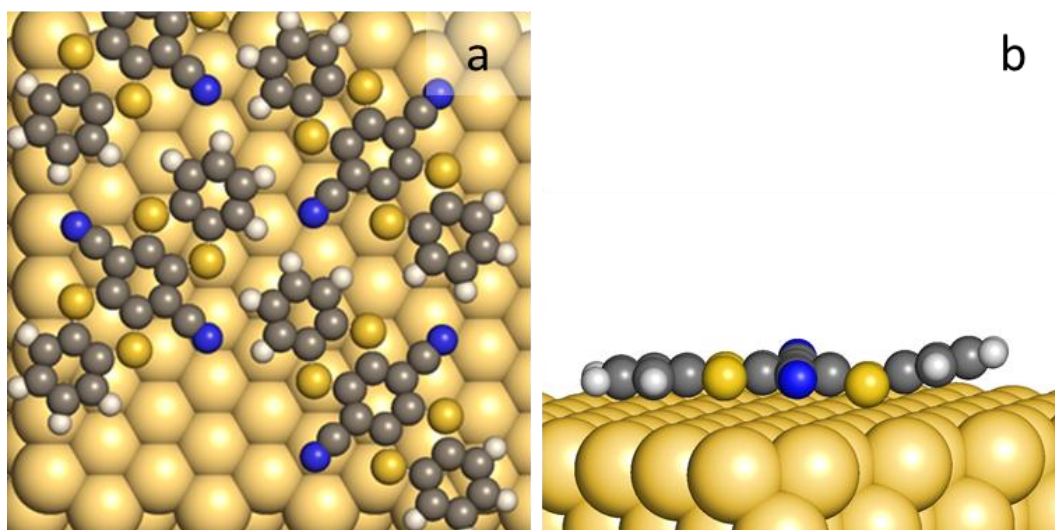


Figure 34: DFT calculated adsorption geometries of bTEpCN in islands on Au(111). (a) Top view (b) Side view showing non-planarity caused by one peripheral benzene ring.

Figure 34 shows the results of the DFT calculations. They demonstrate that the molecules adsorb in the fashion we observed experimentally (Figure 34a), and the asymmetric pear shape appearance is due to one of the peripheral benzene rings adsorbing slightly kinked on the surface (Figure 34b). Although it will be discussed in greater detail in the next sections, we must already point out that the non-planarity on the surface is less severe than in the crystal structure, (Figure 32b), owing to the van der Waals interaction with the gold surface.

7.1.3 Tuning the planarity through vertical manipulation

As discussed in Chapter 3 of this thesis, tip-based manipulation techniques are usually of two kinds: vertical manipulation and lateral manipulation. In the former, the tip is

positioned in one spot and suitable voltage/current parameters are applied to address the molecule or atom directly. Depending on the V/I parameters, this can either mean a weak or strong coupling to the target. Lateral manipulation on the other hand, inscribes a trajectory for the tip to follow and in this method, the voltage applied is usually quite low. In this manner, one can imagine it to be more of a pushing mode in which the target is interacted with and is mediated by atomic forces, e.g., van der Waals. For our experiments with the bTEpCN, we have employed vertical manipulation.

Figure 35 shows the indirect isolation of a bTEpCN molecule. We call it so because instead of performing vertical manipulation on the target molecule, we address the neighbouring molecules instead. All vertical manipulations for controllable molecular pick-up were conducted in constant height mode. The general principle and procedure of this process can be summarized thus:

1. Tip approached close to the molecule with a small bias, e.g., 10 mV.
2. Vertical movement over the molecule, with suitable parameters.
3. Retraction of tip to normal scanning position.
4. Re-deposition or discarding of sacrificial molecule elsewhere.

Onto our case, first the molecule of interest was identified and has been shown with a white arrow in Figure 35a. Next, the molecules marked with an “x” (Figure 35b), were picked up sequentially using the STM tip. After three such manipulations, the target molecule was sitting in isolation and interestingly, the topographic appearance of the molecule had altered. This can be seen in Figure 35c, where the single molecule appears symmetric and planar, as compared to the pear shaped appearance in the islands.

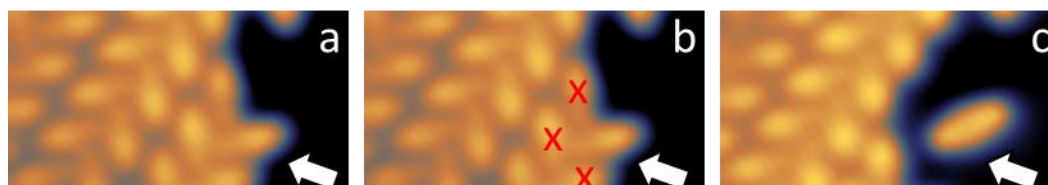


Figure 35. Tuning the nonplanarity of a bTEpCN molecule. (a) The target non-planar molecule located at the edge of the island is marked. (b) Picking up ($V = 10$ mV, $I = 5 - 8$ nA) the three surrounding neighbors (marked with “x”) as an indirect isolation. (c) The remaining target molecule becomes planar. All STM images ($7\text{ nm} \times 3.7\text{ nm}$) were taken under $V = 0.2$ V and $I = 20$ pA.

Indeed, calculations confirmed that the single molecule with no intermolecular interactions is flatter on the surface and loses its non-planar attribute, ie., the terminal ring relaxes onto the surface (Figure 36).

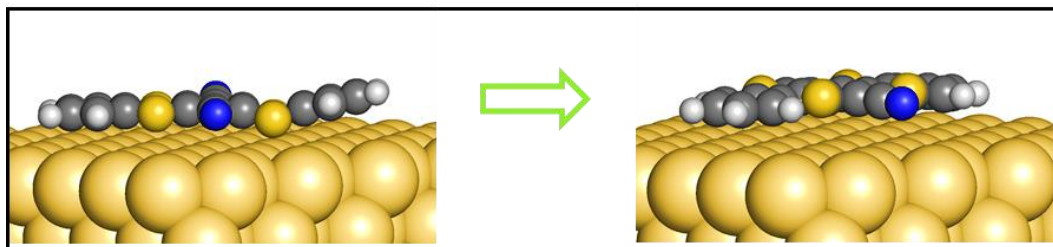


Figure 36: DFT calculated adsorption geometries (side view) of a non-planar and a planarized bTEpCN molecule on Au(111).

This planarization can also be confirmed experimentally, by comparing the linescans taken over the molecule, before and after the tip induced indirect isolation. This has been shown in Figure 37. Figure 37a shows the molecule at the island edge before any vertical manipulation operations around it. The white line indicates where the linescan has been taken. Figure 37b shows the now isolated molecule, with a different appearance as shown earlier and the position over which the linescan was measured. Finally, Figure 37c clearly shows that the red curve, or the linescan over the isolated molecule is lower in apparent height by about 0.05 nm and also more symmetric as compared to the black “before” curve.

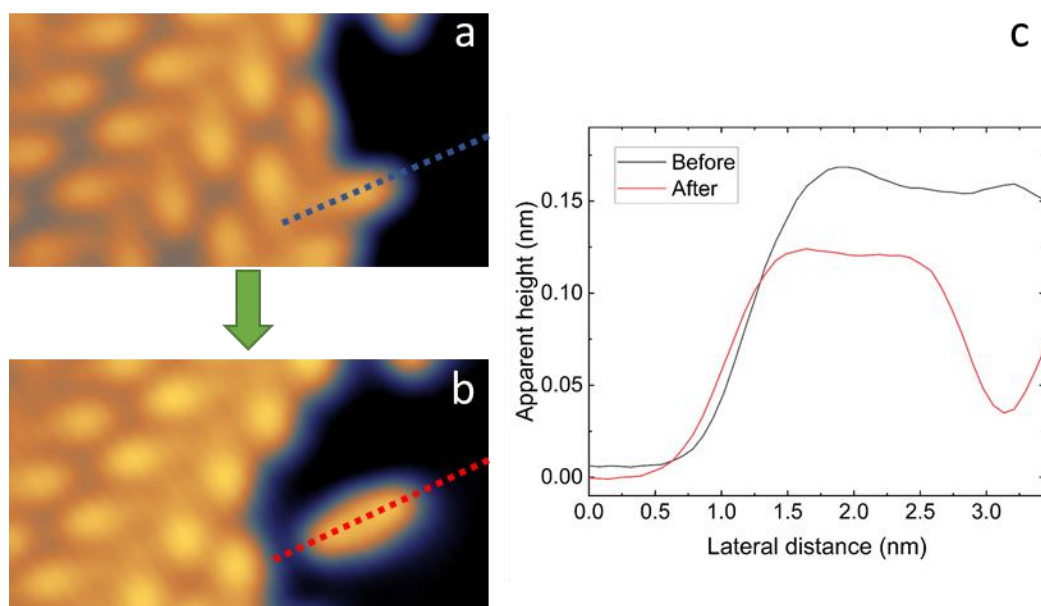


Figure 37: Linescan comparison. (a – b) STM images (7 nm x 3.7 nm) of before and after planarization by STM vertical manipulation (same images as Figure 3). STM images were taken under $V = 0.2$ V and $I = 20$ pA. (c) Line profiles show the different appearances comparing before and after the planarization

We noticed during the controlled removal of neighbouring molecules, that the target molecule did not change appearance, i.e., get planarized when the first or the second molecule was removed. It was only on the third assay, or when it was completely isolated, that we arrived at the second configuration. To test whether the molecule needed to be completely isolated in order to be flat, we repeated the indirect isolation on a molecule well within a densely packed island. The sequence shown in Figure 38 illustrates this process. Six molecules were removed sequentially, and we found that as soon as the molecule only had two neighbours, it switched to the planar configuration. That is to say, for the molecule to maintain its non-planarity, at least three neighbouring molecules have to be in play. It must also be noted that there was no difference between the indirectly isolated molecule shown in Figure 35 and Figure 37 and this one. Moreover, no natively existing single non-planar molecules were observed. The planarity tuning was also irreversible since it was not possible to reintroduce neighbours to an isolated molecule.

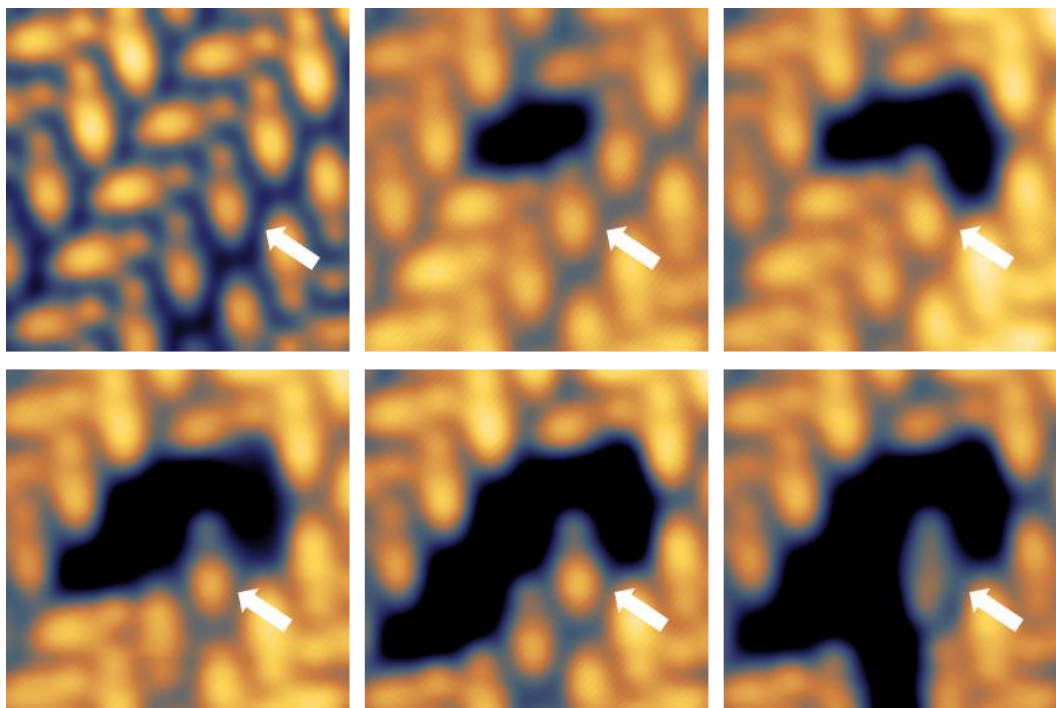


Figure 38: Planarization sequence within an island through indirect isolation. Target non-planar molecule shown with white arrow. The four neighbour molecules are picked up by tip manipulation one by one. The target molecule was planarized after removing the fourth neighbour on its bottom left side. All STM images (4.5 nm x 4.5 nm) were recorded under $V = 0.2\text{V}$ and $I = 20\text{ pA}$. Manipulation parameters: 10mV , $>10\text{nA}$. Figure adapted from [14]

On the basis of the DFT calculations, we know that the C-S-C bending happens on one end of the molecule while the other end remains flat (Figure 35c). The calculated C-S-C dihedral angle is 147° on one side, and the other side is about 180° , confirming that the non-planarity is reduced on the Au(111) surface respect to the gas phase (Figure 31c) due to the van der Waals interaction with the gold surface. The results so far demonstrate that the intermolecular interactions (*e.g.* hydrogen bonds) play a crucial role in promoting the non-planarity. In other words, this may suggest that with if we were to find an area with lower molecular coverage, we might be able to observe different self-assembled structures and conformations.

7.1.4 Quasi 1D chains on Au(111)

We indeed found an area with no large islands, instead we observed a new kind of self-assembly, where the molecules assemble in a one dimensional chains (Figure 39). Unlike in the densely packed islands which did not interact with the herringbone reconstruction, this time around, the molecules formed these chains exclusively on the energetically favourable fcc sites and avoided the soliton (Figure 39a). Taking a close-up STM image allows us to perform some basic analyses about the geometrical setup

of the chains. We find that the angle and inter-molecular distance between the neighbours is 72° and 0.96 nm, respectively (Figure 39b). This is in very good agreement with the calculated adsorption geometries of the quasi-one-dimensional chain, where the angle and the inter-molecular distance between the neighbors with 70° and 1 nm, respectively (Figure 40a and Figure 40b).

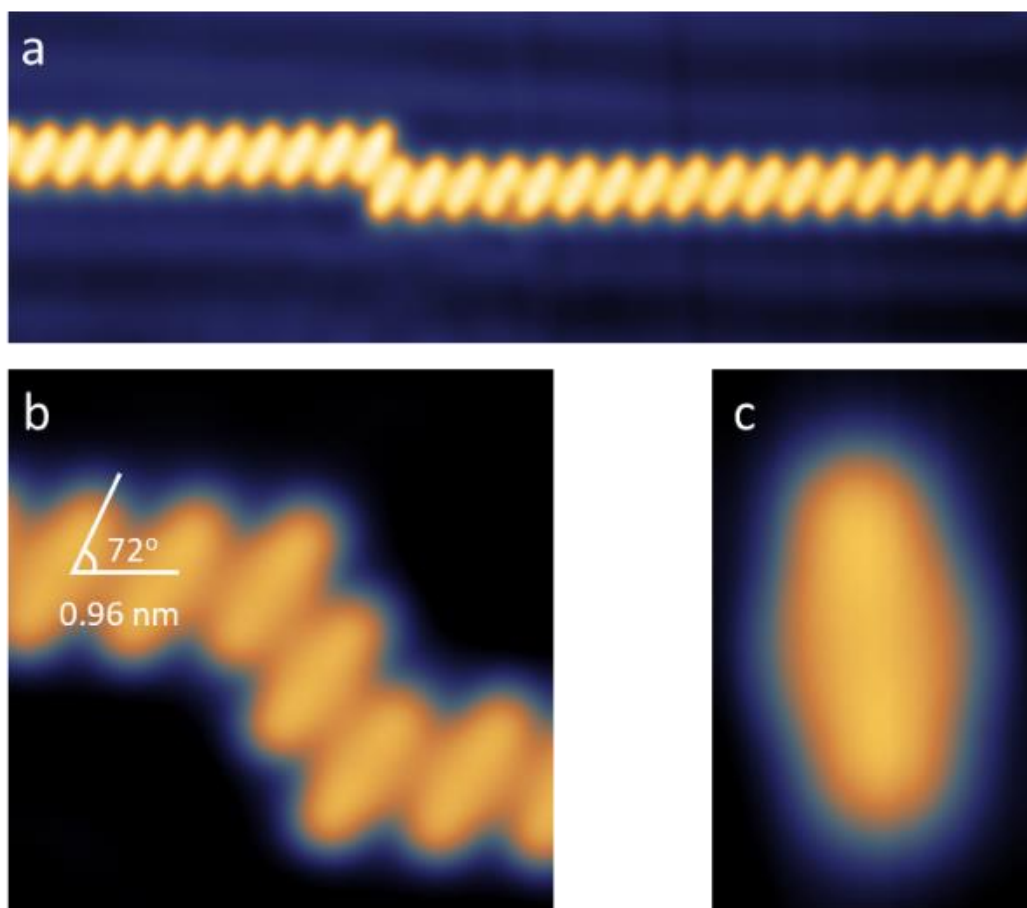


Figure 39: Self-assembled molecular chains and isolated molecule. (a) STM image (25 nm x 8 nm) of a molecular chain along the fcc region of the Au(111) surface. (b) Close-up of a molecular chain (5 nm x 5 nm). (c) An isolated bTEpCN molecule (2.5 nm x 1.5 nm). with same sizes taken at $V = 12$ mV. Constant current STM images were taken under (a) $V = 0.5$ V, $I = 20$ pA, (b, c) $V = 0.2$ V, $I = 20$ pA.

The hypothesis propounded in the previous section was not only that lower coverage might lead to a new self-assembly, but also that due to different intermolecular interactions, the molecules themselves might be in the planar configuration. At a first glance, it does appear so, since the molecules observed so far are symmetric in appearance. By repeating the indirect isolation technique, we successfully isolated a molecule as shown in Figure 39c. The single molecule is also planar and symmetric. Using DFT calculations, we find not only a good agreement of the intermolecular distance and angles as mentioned earlier, but when comparing the adsorption

geometries of molecules in chains (Figure 40a-Figure 40b) and the single molecule (Figure 40c- Figure 40d), we can demonstrate that they are both planar and symmetric. This is also why the STM topographies shown in Figure 39b and Figure 39c have the same appearance.

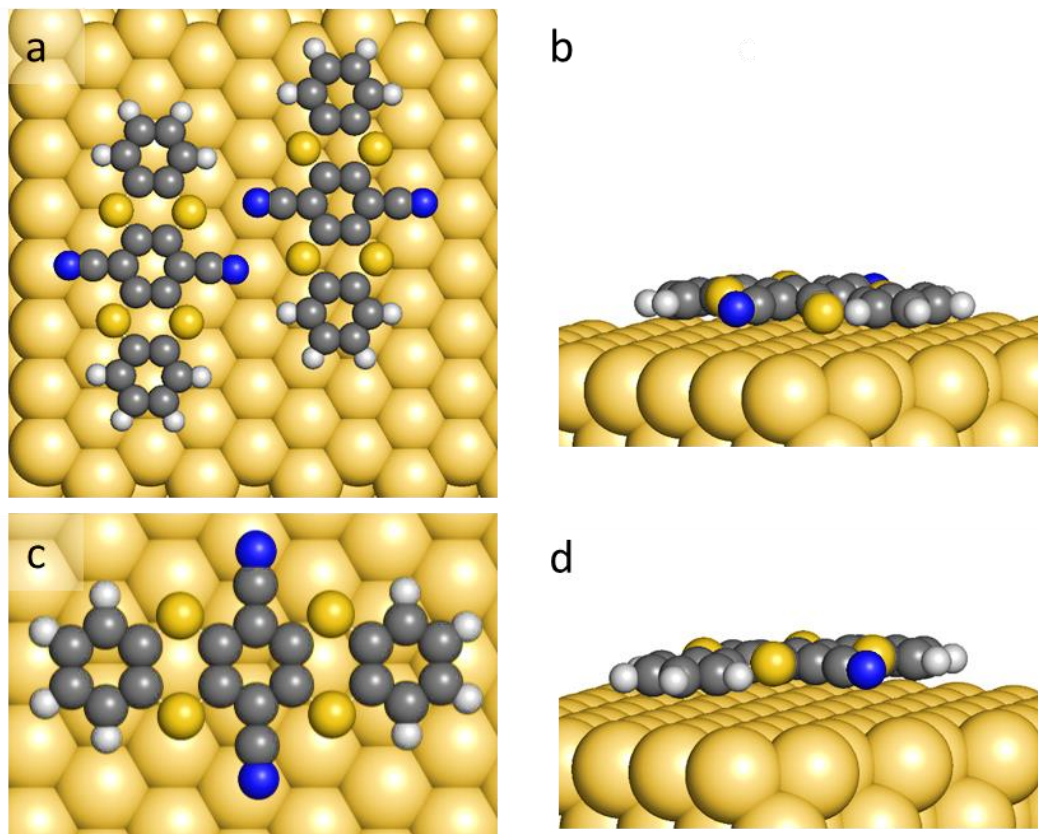


Figure 40: DFT calculated adsorption geometries (top and side views) chain-like self-assembled structures (a – b) and the single molecule (c-d).

We also performed CO tip images in constant height mode on all the available self-assemblies on the surface. This augmented the resolution of the inner structure, especially for the planar conformations.

Figure 41 shows a direct comparison between the two configurations of the molecules. In the island geometry (Figure 41a), the asymmetry is plainly visible. Figure 41b shows the planar molecules that constitute the 1D chains, very different in appearance to that of the islands. Finally, a single isolated molecule is shown in Figure 41c, where we see that it is planar and is the same as those found in the chains. Therefore, we can

unambiguously demonstrate that the difference in planarity is due to intermolecular interactions caused by the self-assembly and nearest neighbor interactions.

Image calculations based on the island adsorption geometry shown Figure 34, and the planar geometry in chains and single molecules (Figure 40) were also performed. These are shown in Figure 41e - Figure 41f. These are metallic tip constant current images and therefore a one to one comparison with the experimental CO constant height is not straightforward. However, there are a few aspects that match moderately well. When comparing the experimental CO image of an island (Figure 41a) with the simulated one (Figure 41d), the asymmetry and the pear shape appearance is discernible. For the planar molecules, both in the chain (Figure 41b) and single (Figure 41c), the corresponding calculated images, viz., Figure 41e for chains and Figure 41f for single, show an overestimation on the contribution of the sulphur atoms to the contrast, but the symmetric appearance is a relatively good match.

We must keep in mind that the disparity between the simulated images and experimental, ones is often due to the overestimation of contrast contributions of certain moieties. In the present case, the simulations show pronounced features around the sulphur atoms in the molecule (Figure 41e -Figure 41f), on account of this overestimation in DFT calculations. Additionally, factors like how the tip is built in the program, atomistic approximations, height offset etc., and also due to the specific functions used for current calculations, in this case the Green function technique [112] could contribute to attributes present in the models and simulated images, that are not observed experimentally.

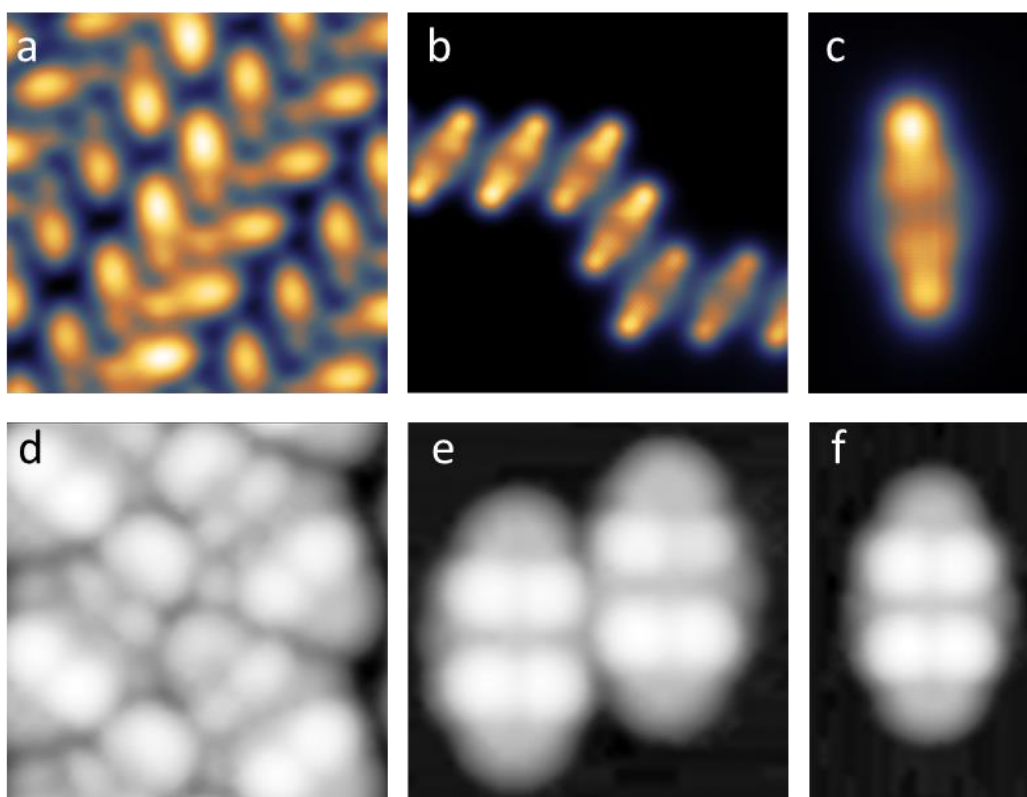


Figure 41: CO-tip constant height images of different self-assemblies and configurations. (a) Island assembly and non-planar configuration. (b) 1D chain and planar configuration. (c) Isolated molecule in planar configuration. Image parameters: $V = 12$ mV; size: (a) and (b) 5 nm x 5 nm, (c) 2.5 nm x 1.5 nm

7.1.5 Electronic properties of planar and non-planar bTEpCN

We first performed differential conductance measurements on an isolated molecule, which means the planar form. As explained in the previous chapter, we first take a dI/dV spectrum on the molecule with a metallic tip, identify the resonances and then take a map to see the spatial charge distribution at these resonances. Figure 42a shows the dI/dV spectrum in red, recorded on the molecule. Three peaks are visible within the range probed by our STS (-2.5 V $< V < 2.5$ V), viz.; -2.30 V, 0.70 V and 1.70 V. There is also a very slight feature observed at -0.85 V.

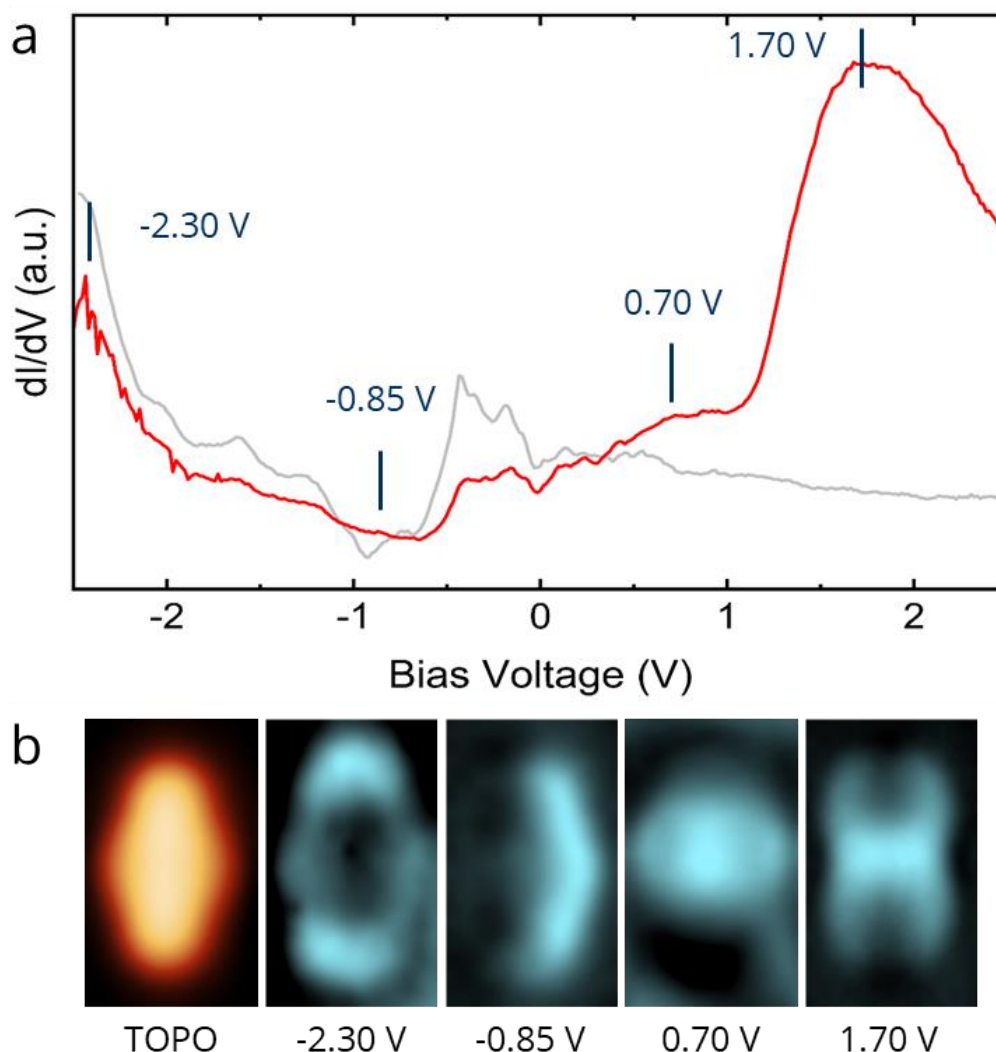


Figure 42: dI/dV spectra and maps of an isolated planar bTEpCN molecule. (a) dI/dV spectrum of the planar (red line) configuration, in grey for comparison the dI/dV spectrum recorded on the clean Au(111). (b) STM topography and the dI/dV maps corresponding to the electronic resonances ($I = 300$ pA).

We recorded dI/dV maps at values obtained from the STS curve of the isolated planar molecule, these are shown in Figure 42b. As mentioned in Chapter 2, the mono-electronic approximation is not completely valid while tunnelling through a molecule. Therefore, multiple molecular orbitals are required to describe electronic tunneling through a molecule and the electronic resonances observed in STS [113]. Usually, the frontier resonances are determined mainly by the HOMO and the LUMO.

The corresponding DFT calculations of the orbitals are shown Figure 43, and are in good agreement with the experimental results. This illustrates that the observed resonances are the molecular orbitals of the planar bTEpCN molecule, i.e., HOMO-1 ($V = -2.30$ V), HOMO ($V = -0.85$ V), LUMO ($V = 0.70$ V) and LUMO+1 ($V = 1.70$ V) respectively.

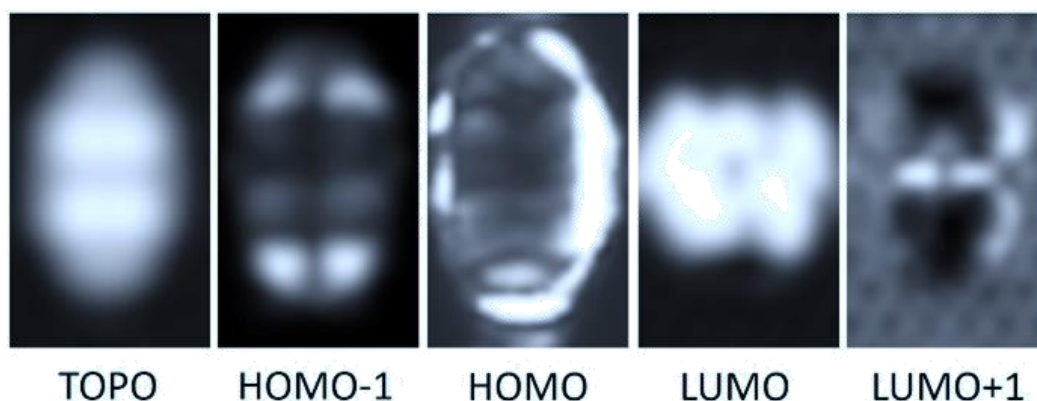


Figure 43: DFT calculated STM topographic image and molecular orbitals.

For the non-planar bTEpCN molecule, we repeated our electronic characterization and found that below the Fermi energy, the resonances are almost unchanged from the planar conformation (Figure 44a). Therefore, the filled states are matching with that of the planar molecule. However, above the Fermi energy, three new resonances are observed, all ensconced within broad, high intensity peaks. These are at 1.50 V, 1.70 V, and 2.45 V respectively, which is well-resolved also in the dI/dV maps. Furthermore, there is a very small feature in the STS at 0.45 V that translates into an intense feature around the Sulphur moieties in the conductance maps (Figure 44b). This is not observed for the isolated planar molecule.

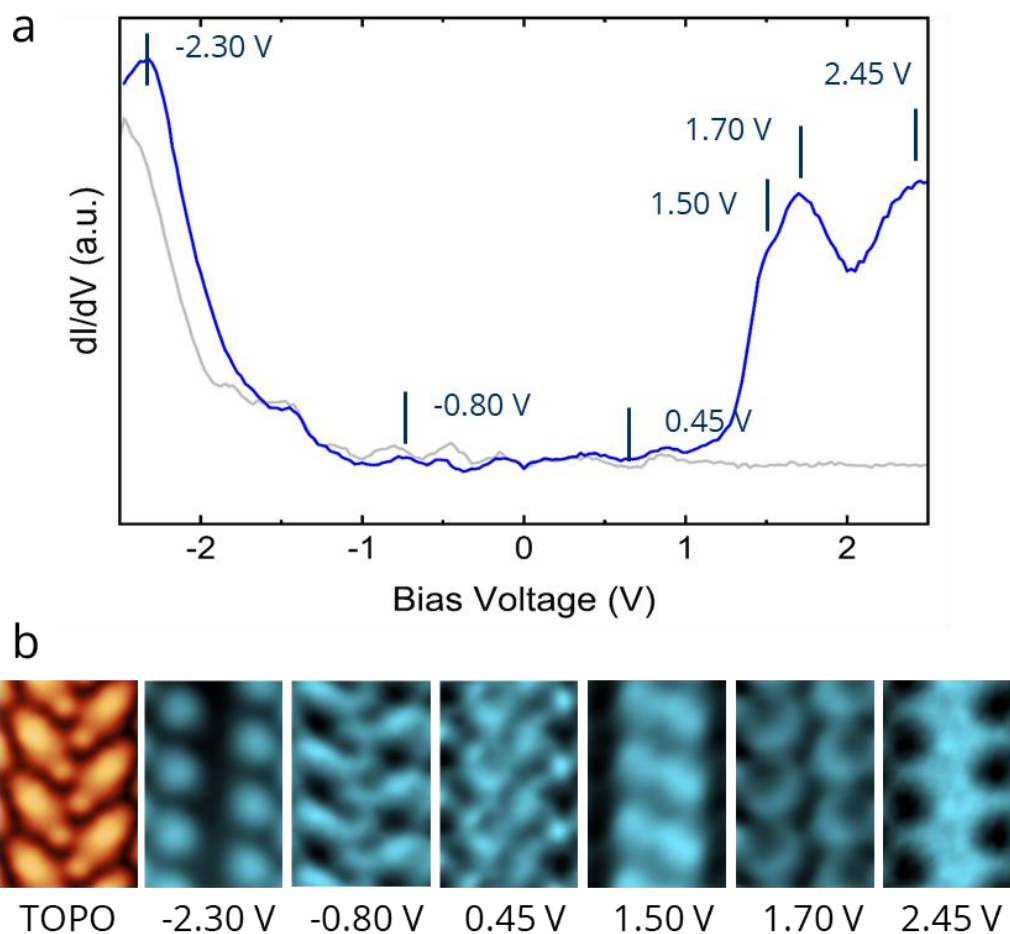


Figure 44: dI/dV spectra and maps of non- planar bTEpCN molecules formed an island. (a) dI/dV spectrum of the non-planar (blue line) configuration, in grey for comparison the dI/dV spectrum on the clean Au(111). (b) STM topography and the corresponding dI/dV maps

It is important to keep in mind that the direct comparison between planar and non-planar bTEpCN is made complex by the intermolecular interactions in the island for the non-planar case. This can influence the observed electronic structure, which is also why comparing the calculated orbitals and the experimental data is not straightforward, therefore, that has not been included.

7.2 Thiophene-based conformational switch

The second molecule presented in this chapter is a Donor-Acceptor-Donor (D-A-D) type molecule called 2,3,7,8-Tetrakis(5-bromo-2-thienyl)pyrazino[2,3-*g*]quinoxaline, or TTPQ as shown in Figure 45. This was synthesized in the X. Feng group in TU Dresden. The thiophene moieties are incorporated to enhance the donor characteristics of the molecule with a pyrazino[2,3-*g*]quinoxaline backbone as the acceptor core. This design also affords rotational flexibility due to the single bonds connecting the four bromothiophene moieties to the rigid backbone.

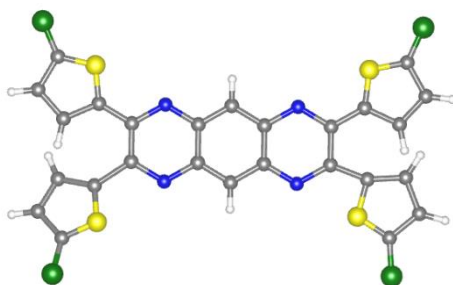


Figure 45: Chemical structure in gas phase. Carbon atoms shown in gray, Hydrogen in white, Nitrogen in blue, Sulphur in yellow and Bromine in green.

7.2.1 Deposition on Au(111)

The evaporation was carried out at 280°C for 30s on an Au(111) surface kept at room temperature (25°C). The molecule which is symmetric, was found to adsorb in two conformations on the Au(111) surface, therefore it is prochiral (Figure 46). Both conformations are in an almost 50/50 ratio. For ease of expression and also because of their topographic shapes, they are dubbed TTPQ-C (Figure 46b in blue) and TTPQ-S (Figure 46c and Figure 46c in green). These congregate in large self-assembled islands (Figure 46a) with a mix of both conformers (Figure 46b and Figure 46c). Sometimes some local domains formed by TTPQ-S are observed, which are hexagonal in geometry. One such example is shown in Figure 46c, with the one TTPQ-S highlighted in green.

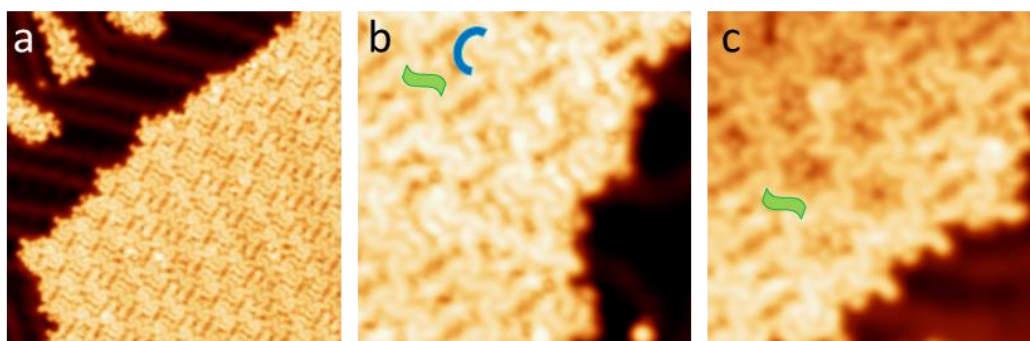


Figure 46: Overview STM images of TTPQ molecules adsorbed on Au (111) after sublimation. (a) Large self-assembled island and smaller islands growing along the FCC sites (b) Close-up of an island with the two molecular conformations superimposed: TTPQ-S in green and TTPQ-C in blue, (c) Close-up of an island with local domains formed by TTPQ-S (shown in green). Image parameters: (a) $V = 0.5\text{ V}$ and $I = 10\text{ pA}$; $40\text{ nm} \times 40\text{ nm}$ (b) $V = 0.1\text{ V}$ and $I = 20\text{ pA}$; $15\text{ nm} \times 15\text{ nm}$ (c) $V = 0.1\text{ V}$ and $I = 20\text{ pA}$; $15\text{ nm} \times 15\text{ nm}$.

7.2.2 Isolation of single molecules through lateral manipulation

Single molecules are vanishingly rare, and therefore, to isolate them, lateral manipulation was employed. This is a well-documented technique that was explained earlier in Chapter 3, where the STM tip is positioned over a user-determined starting point and then moved along a specific trajectory under constant current mode [114] [115, 116]. The voltage and current are kept low in order to be non-destructive. The molecules follow the manipulation path and can be reproducibly addressed. An example of what the tip behaviour looks like during a successful lateral manipulation technique has been shown below.

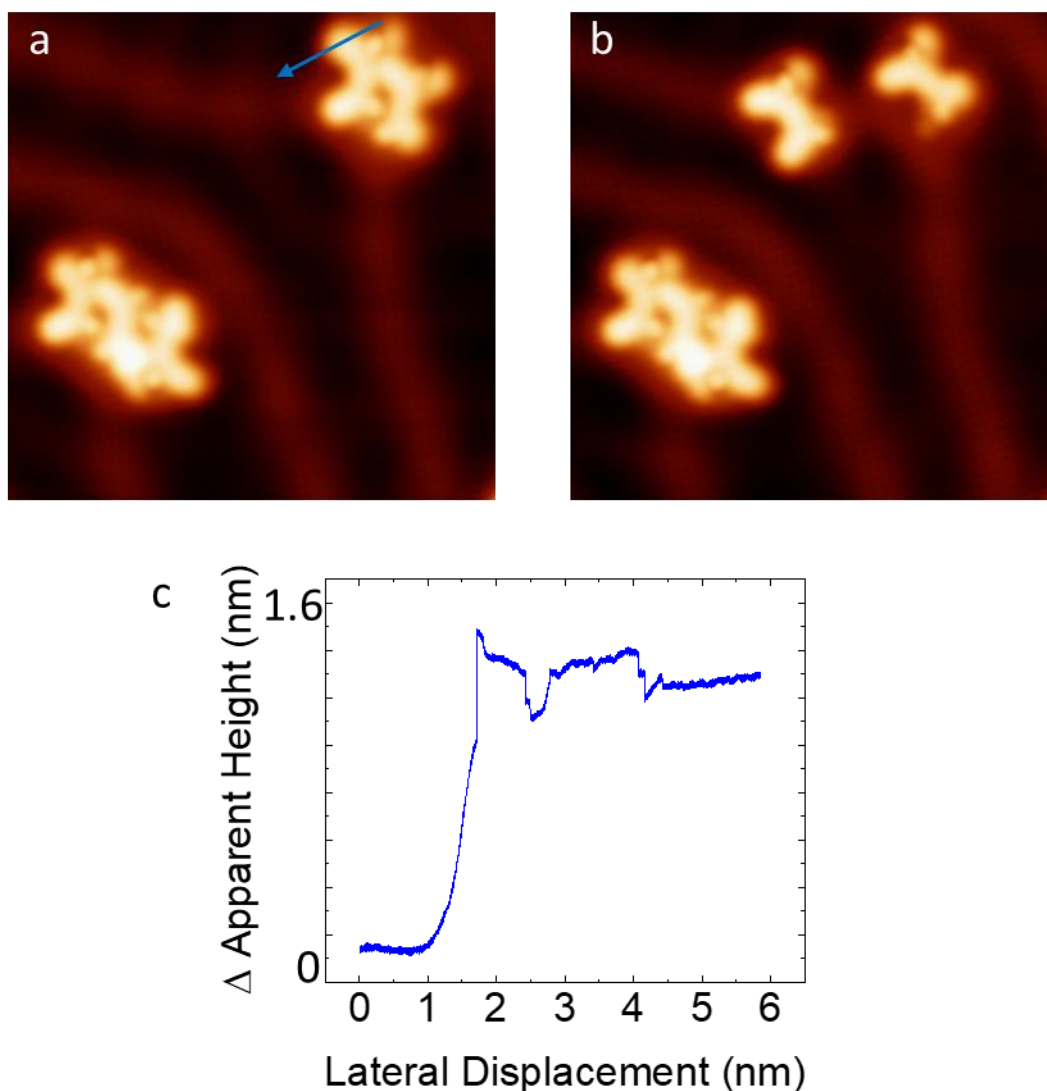


Figure 47: Isolation of single molecule (TTPQ-C). (a) The blue arrow in the image indicates trajectory of lateral manipulation in constant current mode ($V = 10$ mV; $I = 2$ nA). (b) The subsequent image shows that the molecule has been successfully isolated, following the trajectory of the tip. (c) Tip behaviour during manipulation showing tip height vs lateral distance curve. STM images (6 nm \times 6 nm) were obtained under the conditions of $V = 0.1$ V and $I = 50$ pA.

Figure 47a is an example of how lateral manipulation is carried out. First a trajectory is marked for the tip to follow (shown with a blue arrow). With low voltage and current, the manipulation is then executed. The next topography image is recorded, which shows the translation of the molecule along the path defined by the user (Figure 47b). The tip behaviour can be charted by recording a tip height vs. lateral distance curve, which should show the characteristic jumps over the lattice sites, like in Figure 47c.

The sequence in Figure 48, demonstrates the successful separation of molecules from an edge terminus formed by two C form molecules. The target molecules were first separated from the island (Figure 48a) and then from each other (Figure 48b). In some cases, like the one shown in Figure 48c, the single molecules seem to have undergone partial debromination, while in other cases shown in the upcoming sections, all bromines are intact.

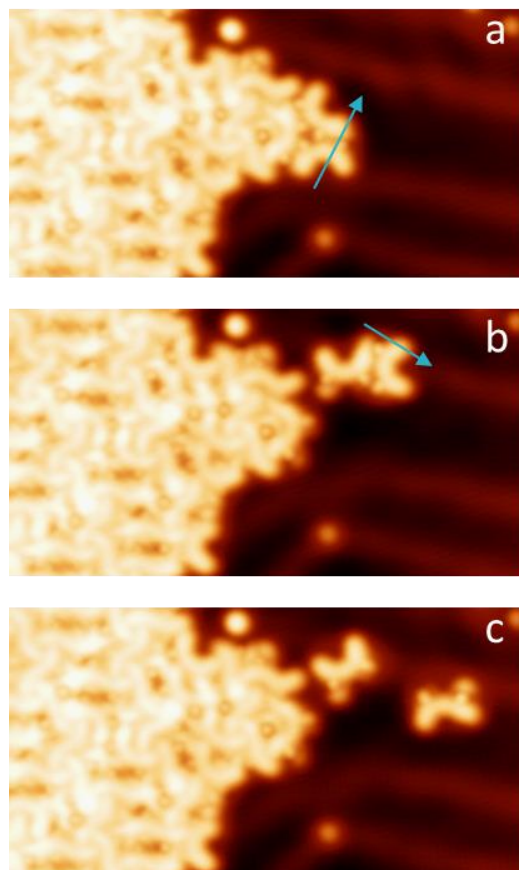


Figure 48: Lateral manipulations of two molecules from an island. (a) STM image of an ordered island self-assembly. Lateral manipulation is performed ($V = 10$ mV, $I = 2$ nA), where the blue arrow indicates the trajectory of the STM tip. (b) Separation of two molecules from the island and further lateral manipulation using the same parameters is applied along the path shown by the arrow. (c) Completely isolated molecules, both of the C-form. Image parameters: $V = 0.5$ V and $I = 10$ pA; $20\text{ nm} \times 8\text{ nm}$

7.2.3 Single molecule characterization

As shown in the previous section, the molecules are easy to isolate, regardless of whether they are adsorbed with only one other molecule (Figure 47) or at the edge of a larger island (Figure 48). Therefore, we were able to fully characterize single, isolated molecules. The first thing to clarify is certainly the emergence of these two conformers, since being a symmetric molecule, only one species was expected to present on the surface. Performing DFT calculations and comparing those with our experimental results presents the solution which has been elucidated in the next figure.

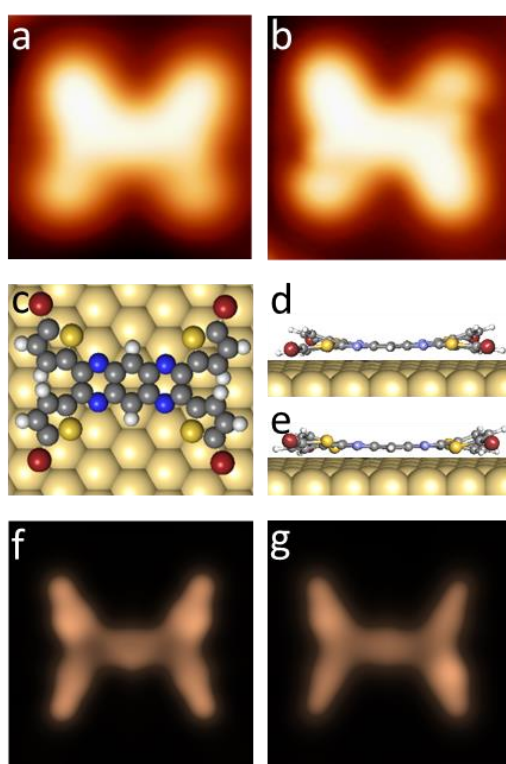


Figure 49: (a) and (b) Experimental STM images of TTPQ-C and TTPQ-S, respectively. Image parameters: $V = 0.1$ V and $I = 10$ pA; 3.0 nm \times 3.0 nm. DFT calculations of adsorption geometry of TTPQ on Au(111): (c) Top view of adsorption geometry (d) Side view of molecular structure showing cis symmetry (TTPQ-C) (e) Side view of molecular structure showing the trans symmetry (TTPQ-S). (f) and (g) Simulated STM images of TTPQ-C and TTPQ-S, respectively. Figure adapted from [5]

Figure 49a and Figure 49b show experimental STM images of intact TTPQ-C and TTPQ-S, respectively. The top view of the adsorption geometry as calculated by DFT is shown in Figure 49c. This demonstrates that all the sulphur moieties are pointing away from the molecular backbone. So far, the molecule would appear to be symmetric with only one adsorption geometry possible, however, taking a look at the side view, finally

clarifies the differences between the two forms. A closer inspection of the bromothiophene groups reveals that they can adsorb either close or slightly elevated from the surface below. This gives rise to two possibilities. When the two upper groups point away from the surface, the two lower bromothiophenes are inevitably closer to the surface, due to steric hindrance of the adjacent hydrogen atoms. This gives rise to the TTPQ-C form, which can be considered the cis-conformer, as shown in Figure 49d. The second possibility as illustrated by Figure 49e, is when only one of the top bromothiophenes is adsorbed closer to the surface, while the other points away, and the adjacent bottom bromothiophene adsorption is yet again dictated by steric hindrance. This generates the TTPQ-S or trans conformer. The corresponding calculated STM images of the TTPQ-C and TTPQ-S respectively, are shown in Figure 49f and Figure 49g, and are in excellent agreement with the experimental STM image. This proves conclusively that the aforementioned geometries are indeed correct. In conclusion, the two observed conformations of TTPQ on the Au(111) surface are due to the very slight rotation of two adjacent bromothiophene groups.

7.2.4 Electronic properties of TTPQ-S and TTPQ-C

To investigate the electronic structure of the molecule, the STS was performed. Figure 50a shows the dI/dV spectra of both forms of the molecule and (in the inset) the position at which the spectra were taken. Below the Fermi energy, both conformers show a slight electronic offset with respect to each other, the first peak appearing around -0.6 V, which we ascribe to the filled state or HOMO. Above the Fermi energy, two resonances are visible, at 1.2 V for TTPQ-C, and owing to a shift of 0.2 V, at 1.4 V for the TTPQ-S. This shift is seen at both HOMO and LUMO resonances and can be attributed to the conformational difference[6]. However, the peaks are relatively broad, indicating that the tunneling electron resonance is formed by the superposition of several peaks. We ascribe the resonance peak at 1.2 V as the unfilled states or LUMO. With this assignation of the frontier molecular orbitals, we arrive at a bandgap of 1.8 V, which falls within the range of typical D-A-D molecules [117, 118].

We would like to mention at the very outset, that we did not find much electronic differences between TTPQ-C and TTPQ-S, the change that is so clearly visible in the topography is purely conformational in nature, as is the switching between them. A detailed description of the spatial distribution of charge densities follows.

Figure 50f - Figure 50i show dI/dV maps recorded at the resonances discussed previously, i.e., at -0.6 V and 1.2 V. Following the STM topographies shown in Figure 50b - Figure 50e allows us to discern where the electronic densities are localized. As shown in Figure 50g and Figure 50i, there is a localization of LUMO resonances on the bromothiophenes that are in plane with the pyrazinoquinoxaline-core. In other words, around the sulphur moieties that are shifted away from the Au(111) surface

(differentiated lobes in the topographies shown in Figure 50c-e), as compared to the sulphur moieties that are closer to the surface (maxima in the topographies shown in Figure 50c-e). The spatial localization of the HOMO resonance also appears to be restricted to the bromothiophene groups but is less affected by the exact orientation of the sulphur-moiety (Figure 50f and Figure 50h). A contribution of the central rigid quinoxaline core to the contrast in all maps is also observed. The slight change in STM topography between the images is due to the fact that in Figure 50d all bromines are intact, while in the other cases a bromine atom has dissociated. The Br dissociation does not appear to affect energy or spatial localization of the electronic resonances.

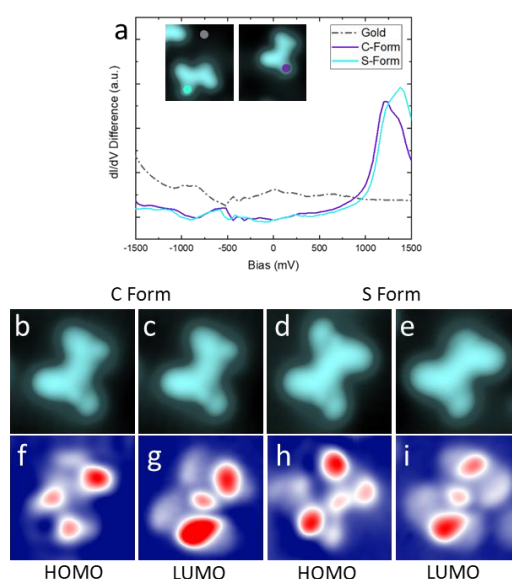


Figure 50: (a) STS spectra of both forms of the molecule (Inset). (b)-(e) topographical STM images ($V = 0.5$ V and $I = 20$ pA), with (d) having all Br intact. (f)-(i) corresponding dI/dV maps taken in constant current mode at (f)-0.6 V (g) 1.2 V (h)-0.6 V (i) 1.2V. All images 3.5 nm \times 3.5 nm

7.2.5 Voltage pulse induced conformational switching

The two molecular conformations on the Au(111) surface prompted us to explore the possibility of switching the molecule between them. In order to do so, the tip was positioned over the target molecule in constant height mode and a voltage pulse of 2 V was applied for 5 seconds. This technique induces tunneling electrons to travel from the tip to the sample, and a small percentage of these can inelastically excite the molecule to induce conformational changes [119]. The sequence shown in Figure 51 demonstrates the reversible switching between TTPQ-C and TTPQ-S. As shown in Figure 51a, the tip is first placed above TTPQ-C, specifically, over one of the bromothiophene groups pointing away from the surface, as evidenced by the differentiated lobe in the topography (in the spot designated with the red star) and

then pulsed. Upon taking an image after the pulse, we observe this pulse to have triggered the rotation of the opposite bromothiophene group, as shown in Figure 51b. The next pulse is applied to the switched bromothiophene group shown in shown in the same figure and we record a current drop indicating that another switching event has occurred. The next STM topography shown in Figure 51c confirms this, where we find that the opposite leg has switched, producing TTPQ-C again. Figure 51d and Figure 51e show the behaviour of the tip during the first and second pulse, respectively. After each pulse, a drop in current of around 3 nA is recorded, signifying an event under the tip, in this case, a successful pulsing event.

The voltage required to trigger the switching lies beyond the LUMO resonance of 1.2 V, suggesting that the switching could be caused by inelastic electron tunnelling (IET) through excited electronic states. In IET manipulation, part of the tunneling electron energy is transferred to the molecule through the excited states, which leads to vibrational, rotational, or electronic excitations [120]. The molecule subsequently relaxes, transforming the excitation energy into movement on the surface or, as in the present case, into an intramolecular conformational change. The position of the voltage pulse on the molecule does not necessarily correspond to the part of the molecule which is going to move or to change configuration after relaxation, but more to the position where the electronic or vibrational mode can be excited [39]. In our case, the LUMO localization around the raised sulphur moieties matches with the pulse location for successful events, further confirming the excitation of electronic resonances.

Therefore, it is safe to conclude that by pulsing on the raised sulphur moieties, we induce its tilting towards the surface, causing the rotation of the adjacent bromothiophene group due to steric hindrance.

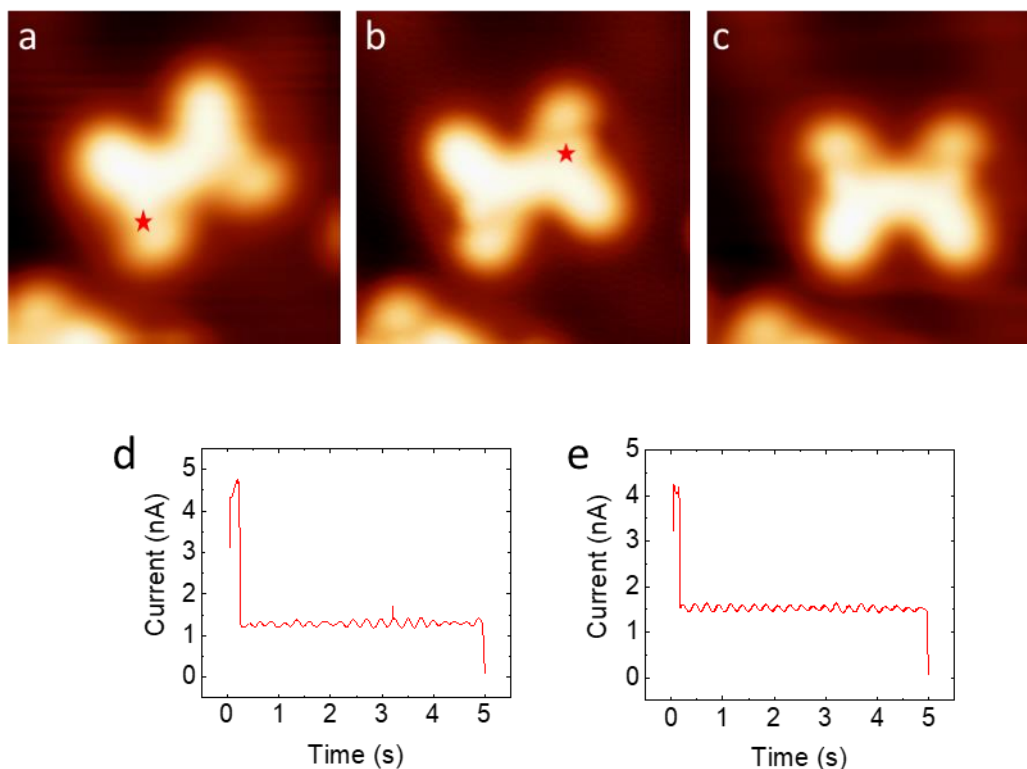


Figure 51: On-surface reversible switching event of the C-form of molecule. (a) A voltage pulse ($V = 2.0$ V, 5 seconds; marked position) is applied above the molecule that was isolated. (b) A slight lateral displacement was induced, and the appearance of the molecule has changed to the S-form. (c) Upon a further pulse in the marked position, the molecule switches back to C-form. (d) - (e) Current vs. time curve showing the tip response during the first and second pulse, respectively. Image parameters: $V = 0.1$ V and $I = 20$ pA.; 4.5 nm \times 4.5 nm. Figure adapted from [5]

This switching mechanism can be better understood graphically by following Figure 52. This shows a close-up of the calculated adsorption geometry of the TTPQ molecule, highlighting the sideview of the bromothiophene groups. The red and green arrows indicate the flip-flopping of the adjacent hydrogen atoms. This explains the lack of intermediate switched structures, since it is always the reciprocal change in the adsorption site of the bromothiophene groups that causes the switching.

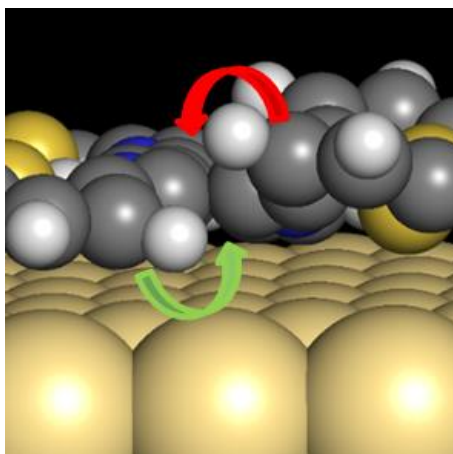


Figure 52: DFT calculation of the bromothiophene groups. The arrows indicate the rotational direction

Nudged Elastic Band (NEB) transition state calculations show that the barrier for going from TTPQ-S to TTPQ-C is around 0.04 eV confirming that the two conformations are very close in energy and that a switch is very likely to take place. These energy profiles have been shown in Figure 53.

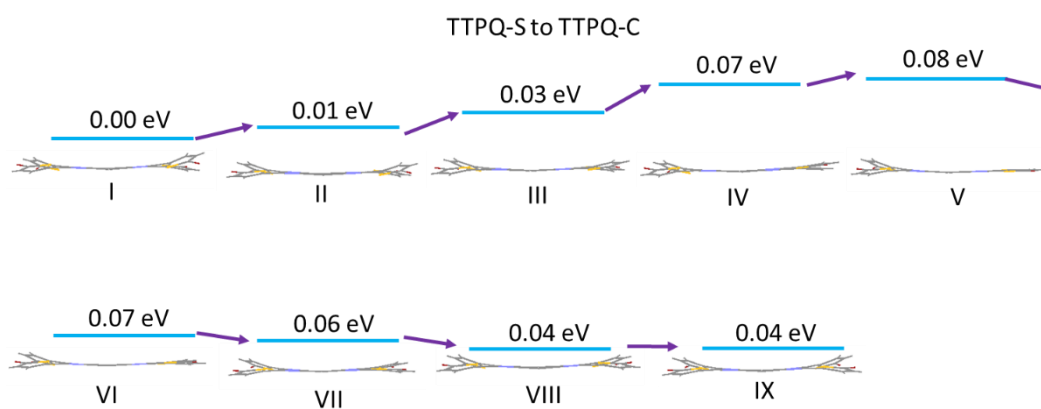


Figure 53: Energy profiles at different states and the corresponding adsorption geometries. Side view of the simulated adsorption geometries, calculated by DFT, starting from TTPQ-S (state I), through intermediate states (II-VIII) to TTPQ-C (state IX). The corresponding reaction energy profiles (in eV) are calculated by the nudged elastic band (NEB) method. Figure adapted from [5].

7.2.6 Role of substrate: Molecular adsorption on Ag (111)

We deposited the TTPQ molecules on Ag(111) as well, and found that on this surface, the molecules adsorb only in one conformation (Figure 54). We also found evidence of on-surface debromination and linkages, as has been well-reported in literature[97].

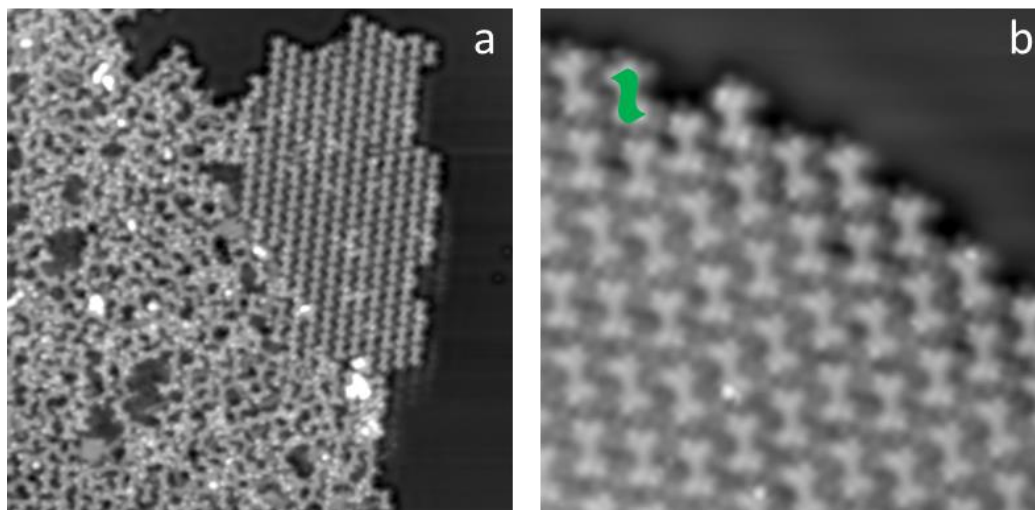


Figure 54: (a) Self-assembly upon evaporation onto RT Ag(111) showing linkages and single molecules. (b) Single molecules surrounded by dissociated bromines. Image parameters: $V = 0.5$ V and $I = 10$ pA; (a) 80 nm x 80 nm (b) 12 nm x 12 nm.

Figure 54a shows a large scan area of the Ag(111) surface, with single molecules and disordered molecular structures. The single molecules are dotted with dissociation bromines and are restricted to their trans conformer or TTPQ-S (marked with green in Figure 54b).

Since we found evidence of only one conformer on Ag(111), it means that this was the energetically favourable form on this particular substrate. As a result, we could not switch this molecule to any other conformation.

7.3 Summary

The first part of this chapter was dedicated to the on-surface investigation of single bTEpCN molecules on Au(111). We found that this molecule can adsorb in two conformations, one slightly more non-planar than the other, and this difference in planarity is dictated by intermolecular interactions stemming from the two kinds of

self-assemblies. Isolated molecules, or molecules in chains, with only two nearest neighbours were demonstrated to be planar, while molecules in islands with at least three nearest neighbours were non-planar. Furthermore, we showed that the surface mitigates the degree of non-planarity, as the crystalline structure is reported to have a larger dihedral angle. Using tip-based manipulation techniques to modify the self-assembly, we successfully planarized the molecule and probed the electronic structure of both conformations.

The second molecule, TTPQ, was found to be not only prochiral on Au(111), but could be switched reversibly between its two chiralities. We discovered that the switching had no effect on the electronic properties of the molecule, therefore it was a purely conformational switch. Additionally, the effect of the substrate on the adsorption geometry was illustrated experimentally, by probing the behaviour of molecules on Ag(111), where the molecules showed a strong preference to only one conformation and therefore switching was not possible.

In short, while both the molecules demonstrated ordered self-assemblies on Au(111), in one case, the tip induced conformational change was due to intermolecular interactions, while in the second, due to intramolecular interactions.

8 On-surface synthesis of long acenes

The on-surface synthesis of long acenes and acene analogues, continues to be of interest to the surface science community. This chapter presents the tip-based synthesis of a novel undecacene analogue and the attempted on-surface synthesis of tetradecacene from two different precursors.

8.1 Polycyclic aromatic hydrocarbons

Acenes are polycyclic aromatic hydrocarbons (PAHs) that are formed by linearly fused benzene rings and can be considered the narrowest form of graphene nanoribbons. Given their highly reactive nature, not only does in-solution chemistry yield poor results in synthesizing longer acenes [121, 122], we also lack a complete understanding of the electronic ground state of acenes longer than hexacene [69]. On-surface synthesis has proven to be efficient both in the generation and characterization of the higher acenes [123-130]. So much so, that in our group, a 12 ring acene has been experimentally generated and studied to show the re-opening of the bandgap [131]. Recent papers on the generation of 13-cene have presented contrasting electronic structures [132] [133], pushing the envelope further to generate and study other PAHs. For example, heteroatom substitution in long acenes [134-137] has paved the way to introducing n-type doping, thereby increasing the appeal of these molecules.

Not only that, considerable effort has also been expended in developing acene analogues, like introducing substituents in the polycyclic systems, especially at the periphery, [24], new kinds of conjugation like quinoidal, [25] or even introducing structural elements to completely or partially break the conjugation, resulting in a variation of the number of Clar's sextets, promoting more stability in the 1D molecular framework [32-35].

The first section of this chapter will be dedicated to the on-surface synthesis and investigation of an analogue of undecacene. Non-benzoid moieties and quinodimethane units are incorporated in the chemical structure to modify the conjugation. This is the first time such structural changes have been incorporated in a PAH, and thus provides an admirable opportunity to probe the relationship between aromaticity and electronic properties.

The second part of the chapter will focus on the attempted synthesis of tetradecacene on surface. This is an extension of the long acene project, wherein the stability and properties of ever-longer acenes are being studied. Two different precursors were investigated, and will be presented in detail. All precursor molecules were synthesized by the group of Diego Peña in Centro de Investigación en Química Biolóxica e Materiais Moleculares (CiQUS) and Departamento de Química Orgánica Universidade de Santiago de Compostela, Spain.

All DFT calculations and simulations were performed by Roberto Robles and Nicolás Lorente in Centro de Física de Materiales CFM/MPC (CSIC-UPV/EHU) and Centro de Física de Materiales CFM/MPC (CSIC-UPV/EHU) and Donostia International Physics Center, Spain.

8.2 On-surface synthesis of isoundecacene

Pure undecacene is the linear *cata*- fusion of eleven benzene rings. The isomer of undecacene that we would like to synthesize on the surface of Au(111), is an organic substitution with two sp^2 hybridized *para*-quinodemethanes (*p*-QDM) and two four membered ring motifs in the form of cyclobutadiene units. The length of an acene is very closely related to its stability, the longer the chain, the less stable the acene. This can be understood on the basis of Clar's π -sextet rule[5]. Therefore, compared to pure undecacene, the isomer proposed should be much more stable as it has five Clar sextets instead of just one. Secondly, the introduction of the (*p*-QDM) units and non-benzoid moieties should play a significant role in altering the electronic structure of the isomer when compared to pure undecacene.

On-surface reactions can be triggered in several ways, through thermal treatment of the surface, photo-catalysis or using the tip to pulse away chemical moieties, for example, halogen, oxygen or as in this case, hydrogen. One of the main benefits of tip-based on-surface syntheses is that one can trigger and probe each step of the reaction, something not accessible through in-solution chemistry. This is how this present experiment has been carried out. After each tip-induced dehydrogenation, the full arsenal of SPM techniques has been used to understand the reaction pathway on the surface starting from the precursor, intermediate species and the final desired molecule. This will be expanded upon in the upcoming sections.

The aryne based synthesis of the precursor molecule is in and of itself a new technique, that has been recently published by our collaborating chemists [138]. The precursor has been shown in Figure 55.

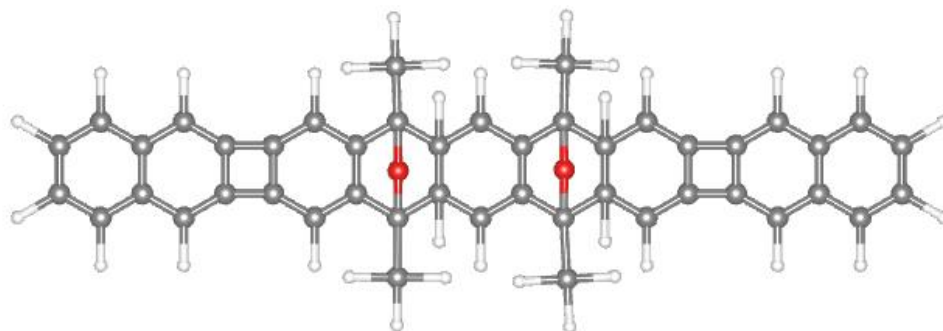


Figure 55: Chemical structure of precursor. Carbon atoms shown in gray, Oxygen in red and Hydrogen in white.

Since this is a large molecule, standard Knudsen cell based thermal evaporation is not feasible. Therefore, the molecules were deposited using a technique called rapid or flash evaporation from a Silicon wafer [16,47]. A suitable current and bias are applied to the wafer with the molecules, and due to Silicon's innate properties, the wafer is heated to very high temperatures in a matter of milliseconds. Therefore, it is possible to sublime large molecules quickly, as they reach vapour pressure without decomposing completely.

As to the molecule that adsorbs on the surface, we had two contenders. One, that the precursor was intact, or two that the epoxy groups had cleaved, as is also known from literature [16]. With the help of our theory collaborators who performed DFT calculations, we found that in order for the epoxy protected acenes to be planar on the surface, it would necessitate a shift of the oxygen atoms around the chemical structure, as shown in Figure 56.

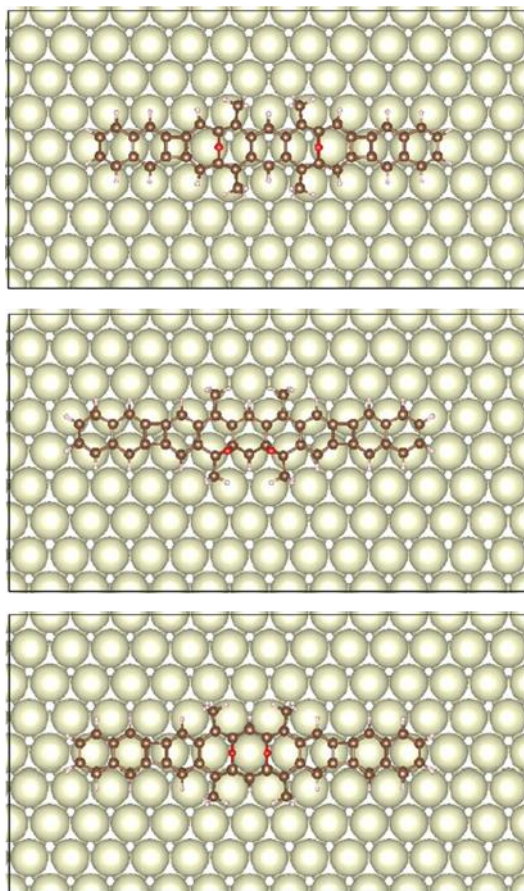


Figure 56: DFT calculations of oxygenated precursors on the surface showing incompatible chemical structure.

Therefore, the molecule that is deposited on the Au(111) surface is the deoxygenated precursor, designated as **I** and shown in Figure 57.

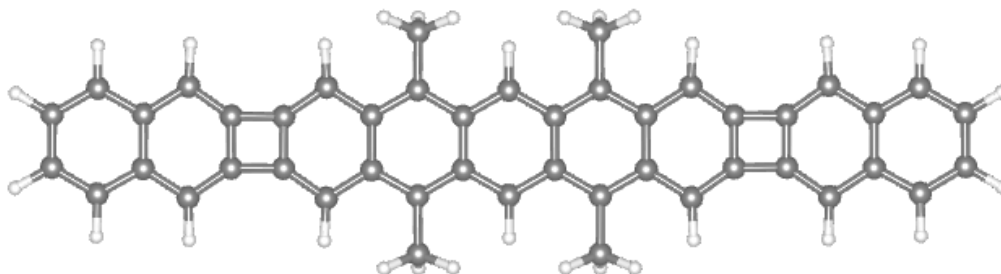


Figure 57: Deoxygenated precursor on the surface.

8.2.1 Flash deposition on Au(111)

An overview of the surface after deposition is shown in Figure 58a. We find that the molecules adsorb as single isolated units, mostly linear in shape (yellow rectangles in Figure 58a), with a few bent molecules. The kinked or bent molecules shown in the red rectangles in Figure 58a were suggested to be precursor molecules where the cyclobutadiene units have undergone and opening and reclosing with a twist, causing this shape. We do find that to be true when looking at the sub-molecular resolution of the nc-AFM image shown in Figure 58b.

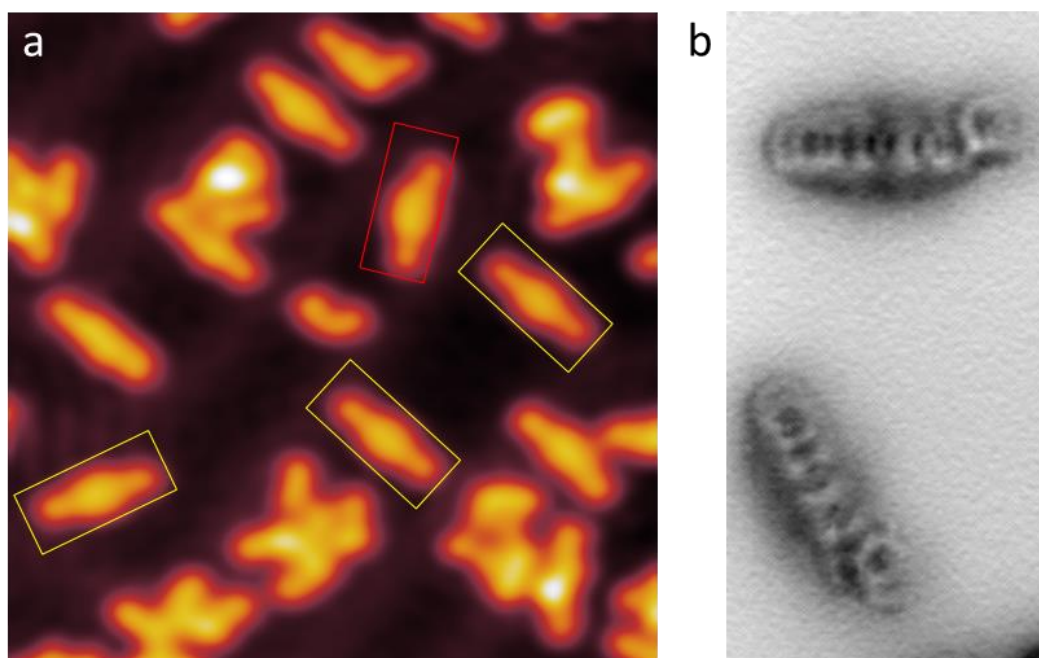


Figure 58: Au(111) surface after deposition: (a) Overview showing linear molecules (in yellow rectangles) and a few kinked molecules (red rectangle). (b) nc-AFM image of two kinked molecules. Image parameters: (a) $V = 0.5$ V and $I = 20$ pA. Image size: 15 nm x 15 nm (b) Image parameters: Amplitude = 150 pm, $V = 1$ mV, size: 6.4 nm x 2.9 nm

The linear molecules are the deoxygenated precursors **I** and have an apparent length of 30 Å (Figure 59b). The bright maxima in the centre of the single molecule shown in Figure 59a can be resolved as two lobes that are attributed to the four methyl groups in the precursor structure.

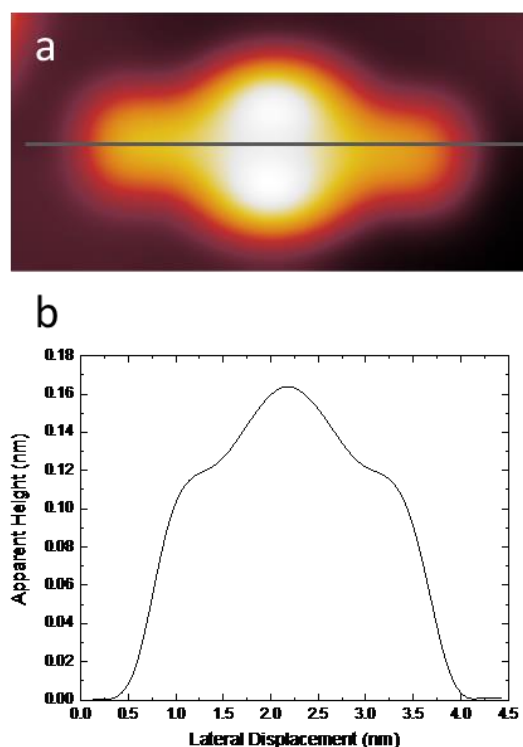


Figure 59: (a) Image of a single molecule with linescan taken over black line. (b) Line profile showing the length and height of the molecule. Image parameters: (a) $V = -1$ V and $I = 20$ pA . Image size: 4.5 nm x 2 nm.

8.2.2 Pulse-induced sequential double dehydrogenation reaction

As mentioned earlier, the goal is to attempt to remove hydrogens from **I**, in a controlled and precise manner. Of course, we must focus on the moieties that are designed to be dehydrogenated, in this case the four methyl units. The reaction schematic is shown in Figure 60. The first pulse should remove one hydrogen each from the targeted methyl groups, generating the intermediate molecular species **II**. The second pulse should again dehydrogenate **II**, by taking two hydrogens, one from each remaining methyl groups, giving us the final product **III**. Therefore, the total number of hydrogen atoms removed step by step is four.

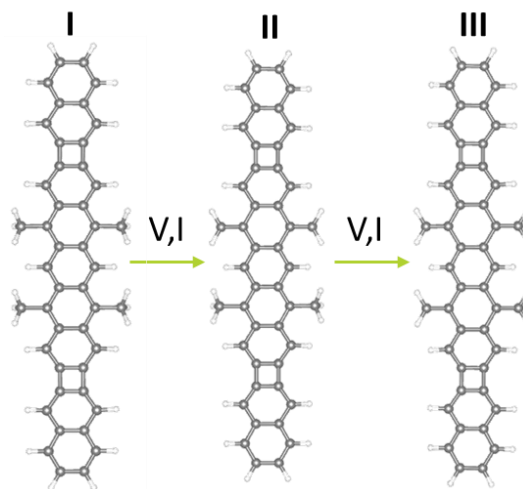


Figure 60: Tip-induced dehydrogenation and conversion from precursor to final molecule.

Figure 61 shows the experimental realization of the quadruple dehydrogenation. For this pulsing sequence, the tip was functionalised with CO, so as to be able to take concurrent constant height images. The chemical structure over each column in the image shows the state of the molecule. First, the tip is positioned over one of the lobes of the precursor molecule **I**. This, as discussed previously, should mean that we are over one of the methyl groups. Indeed, as visible in constant height image shown in Figure 61a, we see four protrusions in the centre of the molecule, demonstrating that we were correct in assigning the lobes to the methyl groups. The red star in Figure 61d marks the position at which a pulse of 2 V and around 1.2 nA is given in constant height mode. Recording the tip behaviour as we do so, shows a current change, signifying an event occurring between the tip and the molecule junction (Figure 61g).

Now, the next constant height CO image is recorded (Figure 61b), showing a very distinct change in the molecular structure. At the pulse position, we now see the emergence of two well-defined lobes, rather than a diffused protrusion, indicating that we have removed two hydrogens with one pulse. Following the chemical structure on the top row, we see that we have arrived at the intermediate species **II**, where two methyl groups have already converted to *p*-QDM units. This is also borne out by the asymmetric constant current topography image, showing the pulsed half of the molecule to be planar and without the maximum (Figure 61e). The next pulse is given at the position being marked with a star (Figure 61e) and elicits a current of 1 nA (Figure 61h).

We hope to have achieved full conversion of the molecule into the final product **III** and this is found to be the case, as evidenced by the next set of images. The constant height

image now shows four very well-defined central lobes attributed to the *p*-QDM units (Figure 61c). The constant current image is also much more symmetric and planar as well (Figure 61f), indicating that the on-surface reaction of the conversion from *p*-dimethylbenzene to *p*-QDM (Figure 61i) has been successfully achieved.

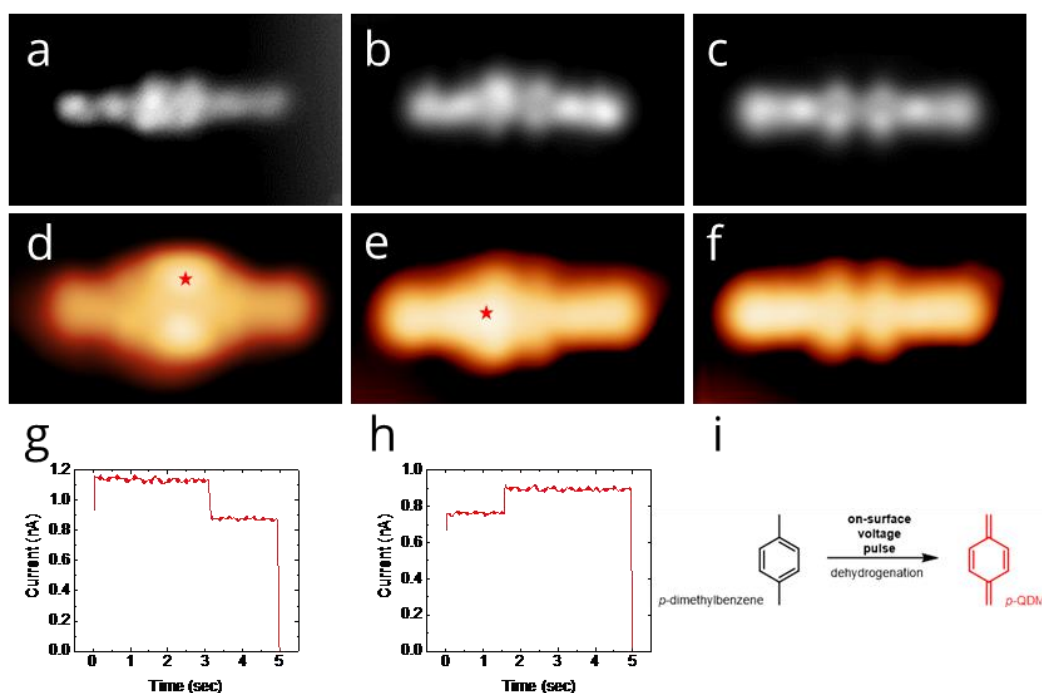


Figure 61: Pulse-induced dehydrogenation (a) - (c) Constant height CO images of taken after each pulse. Image parameters: $V = 10$ mV, size : 3.5 nm x 2.0 nm. (d) - (f) Constant current STM images with a CO tip showing pulse position (red star). Image parameters: $V = -1$ V, $I = 100$ pA, size: 3.5 nm x 2 nm. (g) - (h): Current vs. time curve showing tip response after each pulse. Pulse parameters: 2 V, 5 seconds. (i) Reaction summary.

8.2.3 DFT calculations of adsorption geometry and image simulations

DFT calculations of the adsorption geometries of **I**, **II** and **III** are shown in Figure 62. They illustrate that the deoxygenated precursor **I** adsorbs flat on the surface (Figure 62a). After the first pulse, the dimethylbenzene that has converted to *p*-QDM has a slightly stronger interaction with the surface as compared to the unreacted one. Therefore, the intermediate species, **II** is mildly non-planar and asymmetric (Figure 62b). The quadruple dehydrogenated final molecule **III** has a stronger interaction with the surface than the precursor **I**, but is symmetric (Figure 62c).

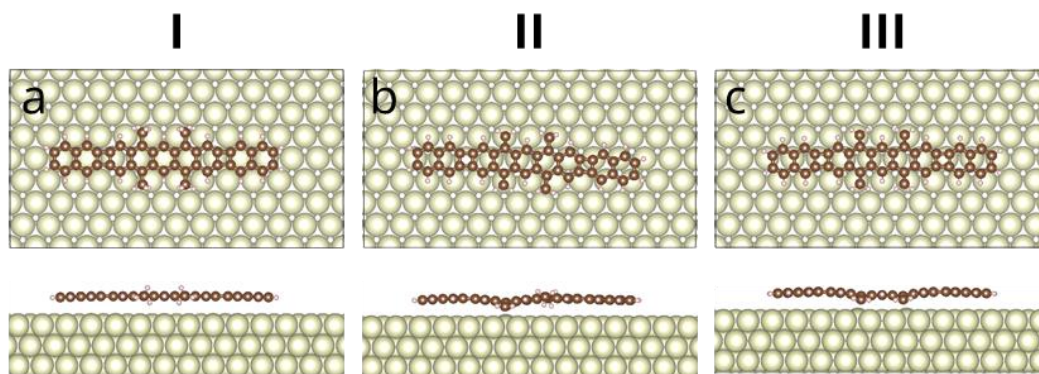


Figure 62: Adsorption geometries and image calculations: (a) - (c) Top and side vies of each molecular species' adsorption geometry on Au(111).

Based on the calculations, STM topographies were simulated, again of all three species of the molecule. These are shown in Figure 63. There is an excellent match with the experimental images, if one compares it with Figure 61d - Figure 61f. The central lobes in the precursor molecule were correctly attributed to the methyl groups and the progression of the tip-induced topography change is quite clearly what we also see experimentally.

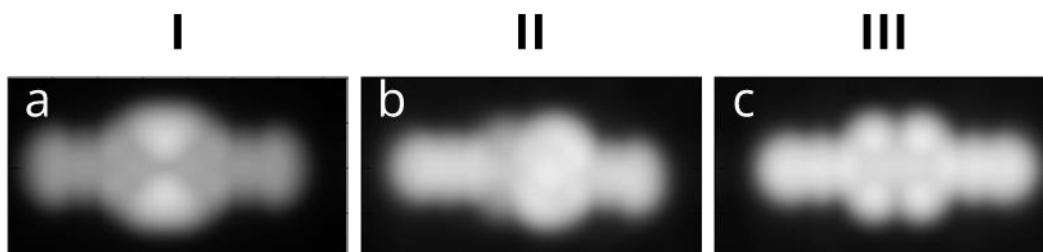


Figure 63: Calculated STM topographies.

8.2.4 nc-AFM with qPlus sensor

The intermediate species **II** and the final molecule **III** were investigated using nc-AFM as well, since we wanted to probe the sub-molecular structural changes that came with the chemical conversion. This was not accessible by constant height images with a CO tip, although they were sufficient to ascribe the chemical structure.

We now switched the STM tip with the qPlus tip, since as explained in Chapter 2, this would allow us to take STM as well as AFM measured. We functionalized our qPlus tip with CO, because there is no such thing as too much resolution.

The images of **II** and **III** are shown in Figure 64. We were, if I may use the superlative here, delighted to find that the images not only showed clearly the benzene rings, but also the square cyclobutadiene units. Furthermore, Figure 64a shows two intense maxima as the periphery of the molecule, which is due to the unconverted methyls. The slight non-planarity, as theorized by the DFT calculations (Figure 62b) is very much in evidence here. In contrast, **III** (Figure 64b) is symmetric with the central rings displaying a very slight lowering of contrast, due to its structure being depressed towards the surface, again in agreement with the calculations (Figure 62c).

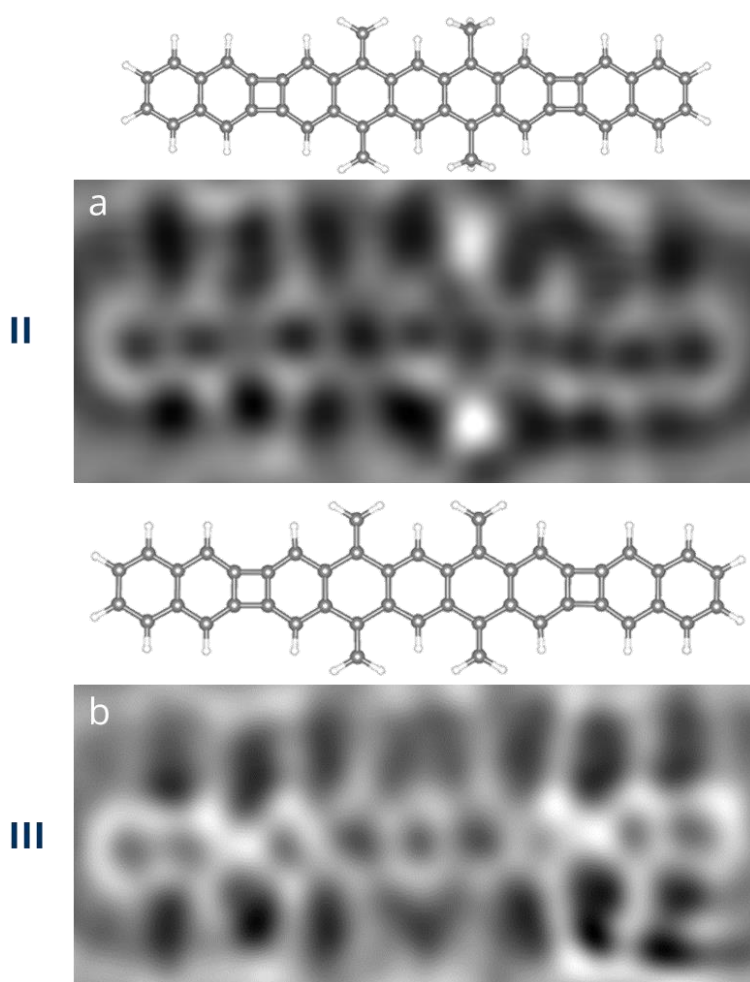


Figure 64: (a) Laplace filtered nc-AFM image with CO functionalized tip of the partially reacted **II**. (b) Laplace filtered nc-AFM image with CO functionalized tip of the final product, **III**. Image parameters: (a) Amplitude = 300 pm, $V = 1$ mV, size = 4.0 x 1.7 nm (b) Amplitude = 150 pm, $V = 1$ mV, size 4.0 nm x 1.7 nm.

This is unambiguous proof that we succeeded in the on-surface reaction via tip-based manipulations, a rather efficient conversion as it took one pulse per double dehydrogenation. We were able to repeat this over many molecules, and all that was needed to be done now was to probe the electronic properties of all three species. This will be the subject of discussion in the upcoming sections.

8.2.5 Electronic properties: **I**

Figure 65 shows the electronic characterization of precursor **I**. The spectrum was taken with a metallic tip at the edge of the molecule, as shown in Figure 65a. On the negative side, we see a shoulder at around -1.5 V and one the positive side, two very broad and intense peaks at around 1.5 V and 2.5 V. The chemical structure is shown in Figure 65b. Taking conductance maps at the biases recorded from the STS (Figure 65c), gives us an idea of what **I** looks like electronically. Since on the negative side, i.e., below Fermi energy, the STS showed a shoulder feature, we recorded maps at two positions, one at the onset of the curve, and one at the maximum. We discovered that these are indeed coming from the contribution of two different orbitals, since the features around the dimethylbenzene units are changing. At -1.40 V, they are much sharper and well defined, while at -1.55 V, they diminish in contrast almost completely and instead the benzene rings beyond the cyclobutadiene units are quite well-resolved.

Above the Fermi energy, we mapped the spatial distribution of charges at 1.50 V and 2.40 V, both of which were the peak maxima from the STS curve. The states are much more diffused here, along the molecular structure, with some localization around the central benzene ring at 1.50 V and the naphthalene units at 2.40 V.

The calculated dI/dV maps also shown in Figure 65c are in good agreement with the experimental results, however, we refrain from ascribing these resonances to orbitals, since we did not measure any intermediate maps at incremental bias steps as we did for **II** and **III**. These have been discussed in the next sections.

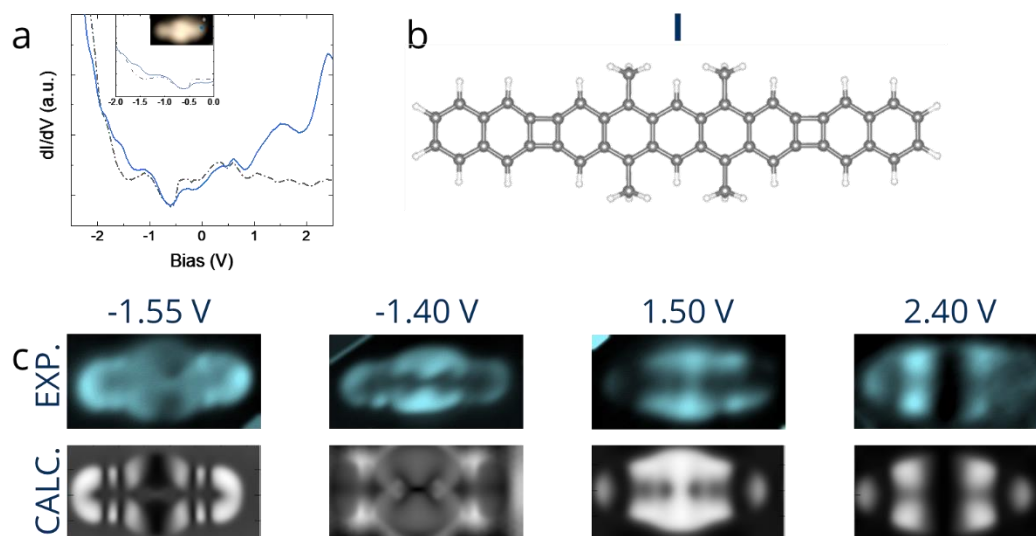


Figure 65: STS and constant current conductance maps of **I**. (a) Constant height STS. Spectra were recorded at the positions shown in the inset. Image parameters: Inset $V = -2$ V, $I = 20$ pA, image size: 4 nm x 2 nm. (b) Chemical structure of deoxygenated precursor. (c) Conductance maps: Top row: Experimental maps. Bottom row: Calculated maps. Image parameters: $I = 200$ pA, size of all images: 3.5 nm x 1.7 nm.

8.2.6 Electronic Properties: II

The intermediate species, or **II**, was quite interesting because of its asymmetry and also due to the different hybridization on the carbons. In the case of the dehydrogenated *p*-QDM, the carbon is sp^2 hybridized, whereas in the hydrogenated dimethylbenzene, it is sp^3 . The STS were taken at either end of the molecule with a metallic tip, and the spectra are shown in Figure 66.

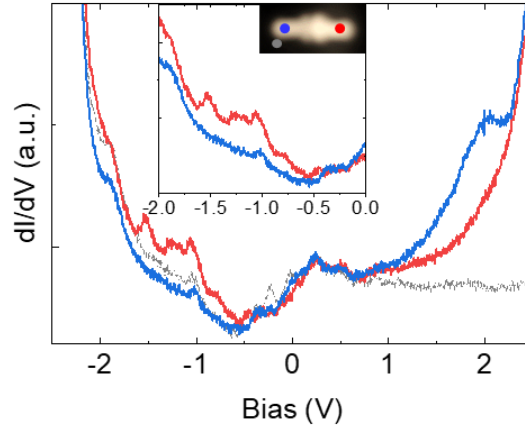


Figure 66: Constant height STS on **II**. Spectra were recorded at the positions shown in the inset. Image parameters: Inset $V = -2$ V, $I = 20$ pA, image size: 4 nm x 2 nm.

Since we found several close-packed and low intensity peaks below Fermi energy and quite broad peaks above, we performed what we will call a bias sweep. After determining the maximum of each peak of the STS curve, we increased the bias in small steps around this value and recorded conductance maps at each of these incremental values. We did this for both the positive and the negative side. The negative sweep is shown in Figure 67.

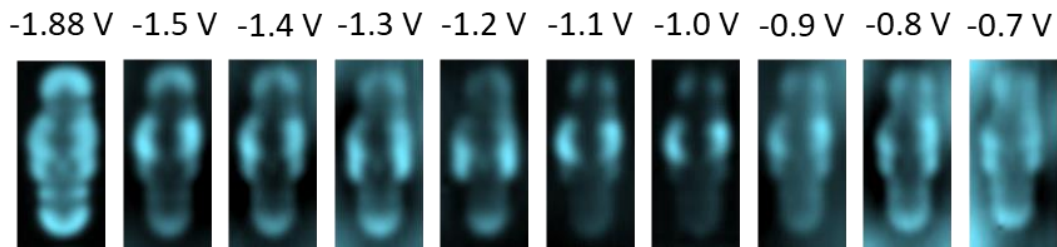


Figure 67: Constant current conductance maps of **II** taken below Fermi energy at incremental bias steps. Image parameters: $I = 200$ pA, size: 1.7 nm x 3.5 nm.

We find that in general, the contrast is localized around the dimethybenzenes and the *p*-QDM, with edge states visible that are characteristic of acenes. The contrast in the maps correspond well to the values gleaned from the STS curves, i.e., -1 V, -1.5 V and -1.88 V.

On the positive side however, we see a strong contrast at 1.84 V and at 2.04 V, which is the peak maximum from the STS curve, a different localization of states, meaning that it is another orbital. At the position of the second peak from the curve, i.e., at 2.45V, we again discover that the local densities of states are distributed differently, signifying that this is from the contribution of another orbital.

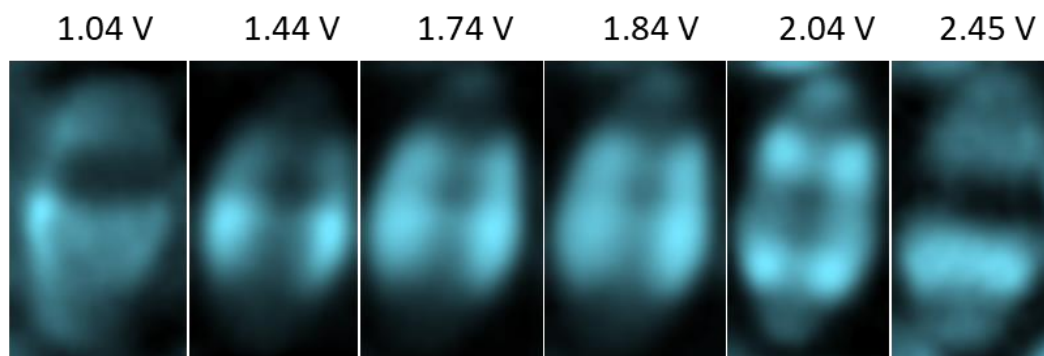


Figure 68: Conductance maps taken below Fermi energy at incremental bias steps. Image parameters: $I = 200$ pA, size: 1.6 nm x 3.5 nm.

Figure 69a shows the chemical structure of the intermediate species II and the experimental dI/dV maps that we selected to be the ones describing the orbitals as shown in the top row of Figure 69b. The filled states are as found in the STS curve in Figure 66 and are ascribed as -1 V for HOMO, -1.53 V for HOMO -1 and -1.88 V for HOMO-2. The unfilled states are ascribed based on where the contrast was brightest in the sweep, rather than simply the peak maxima as discussed. Therefore, 1.74 V is the LUMO, 2.04 V is the LUMO+1 and 2.45 V is the LUMO+2. This is also in relatively good agreement with the calculated maps, shown in the bottom row of Figure 69b.

Below the Fermi energy, the states are localized strongly around the dimethylbenzenes and only the HOMO-1 shows clear contrast on the molecular 1D framework. What is important to note is the asymmetric shape of this charge distribution, which would of course make sense. The unfilled states similarly show an asymmetry, and apart from that, the localization remains much the same as the precursor I shown in Figure 65c.

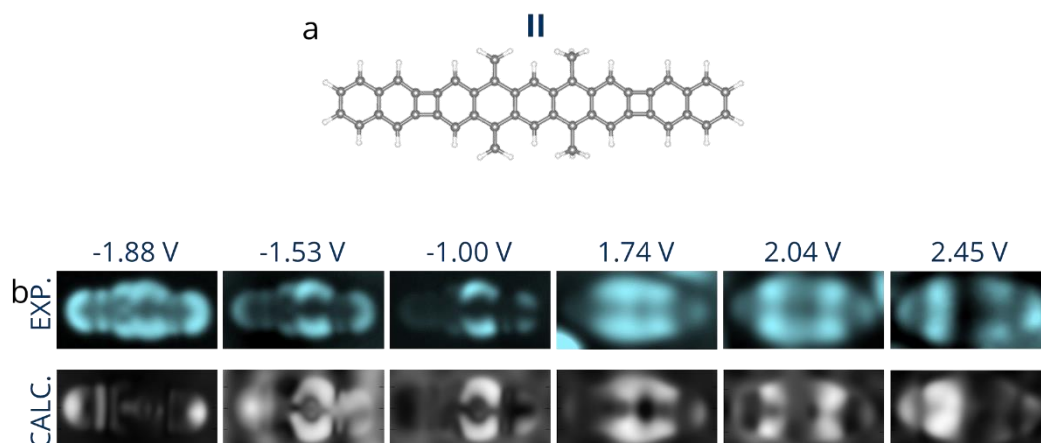


Figure 69: (a) Chemical structure of intermediate molecule **II**. (b) Conductance maps: Top row: Experimental maps. Bottom row: Calculated maps. Image parameters: $I = 200$ pA, size of all images: 3.5 nm x 1.7 nm.

8.2.7 Electronic Properties: III

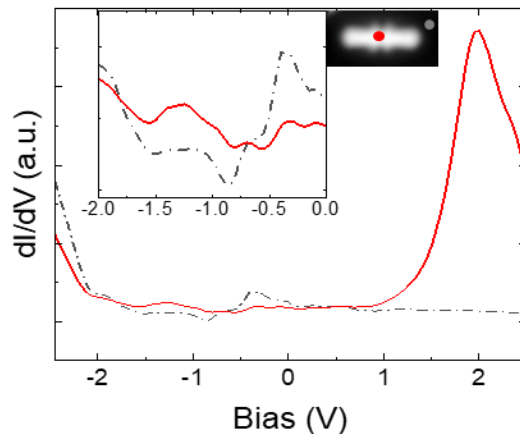


Figure 70: Constant height STS on **III**. Spectra were recorded at the positions shown in the inset. Image parameters: Inset $V = -2$ V, $I = 20$ pA, image size: 4 nm x 2 nm. (b) Chemical structure of deoxygenated precursor. (c) Conductance maps: Top row: Experimental maps. Bottom row: Calculated maps. Image parameters: $I = 200$ pA, size of all images: 3.5 nm x 1.7 nm.

Finally, we have arrived at the quadruple dehydrogenated end product, **III**. The STS shown in Figure 70 illustrates that there is a very intense and again, broad peak at 2 V. The negative resonances are difficult to discern and have therefore been magnified in

the same image and show a peak starting at around -1 V whose maximum lies at -1.25V. We performed the bias sweep again, as described in the previous section.

The conductance maps recorded below the Fermi energy are shown in Figure 71. It is immediately apparent that there is only one kind of charge localization, and that the highest contrast is at -1.05 V. Moving away from this bias value only diminishes the contrast.

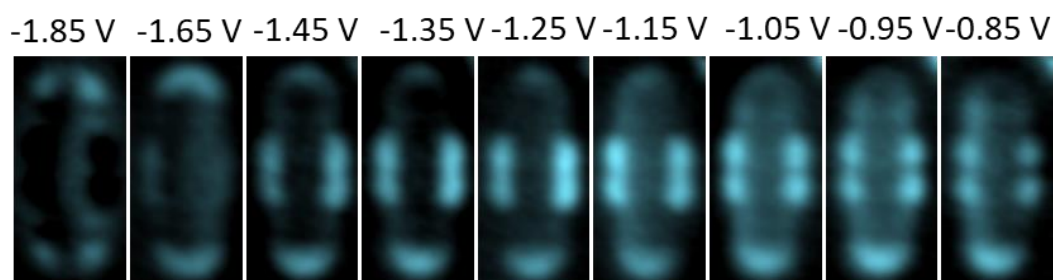


Figure 71: Constant current conductance maps of **III** taken below Fermi energy at incremental bias steps. Image parameters: $I = 100$ pA, size: 1.7 nm x 3.5 nm.

Above the Fermi energy, we see similar behaviour as **II**, where the resonances translate to different charge localizations under the broad 2 V peak from the STS curve (Figure 70). This time, however, we see no asymmetry in the structure, in accordance with the symmetric nature of the final molecule. The maps have been shown in Figure 72.

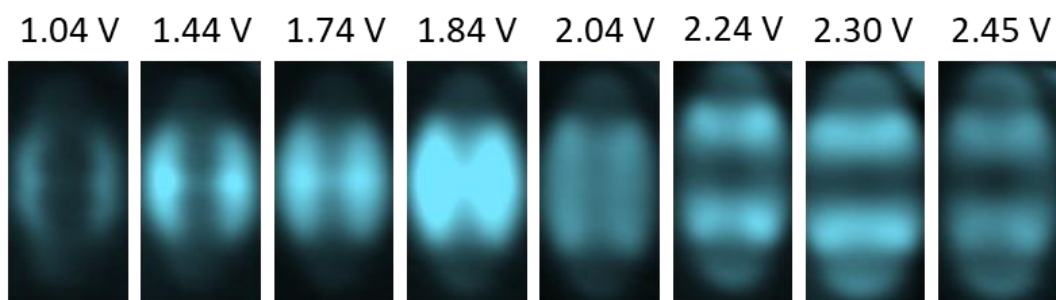


Figure 72: Constant current conductance maps taken above Fermi energy at incremental bias steps. Image parameters: $I = 200$ pA, size: 1.7 nm x 3.5 nm.

Based on these sweeps, we were able to ascribe the HOMO and LUMO states depending on where we saw the highest contrast in the conductance maps, rather than the peak maxima, similar to what we did with **II**. This has been shown in Figure 73. Following the structure shown in Figure 73a, we can clearly see that the HOMO is localized

strongly around the *p*-QDM units and the characteristic acene states are also visible (Figure 73b). The LUMO is at 1.84 V, LUMO+1 at 2.04 V and LUMO+2 at 2.30 V. The localization is very similar to that of **II**, in fact, as are the resonance positions (Figure 69 and Figure 66). The calculated dI/dV maps shown in the bottom row of Figure 73b, are once again in good agreement with the experimental results, illustrating that our assignation of orbitals is correct.

We notice a very small opening of the bandgap when comparing **II** and **III**, which can be explained due to the increased aromaticity of **III**.

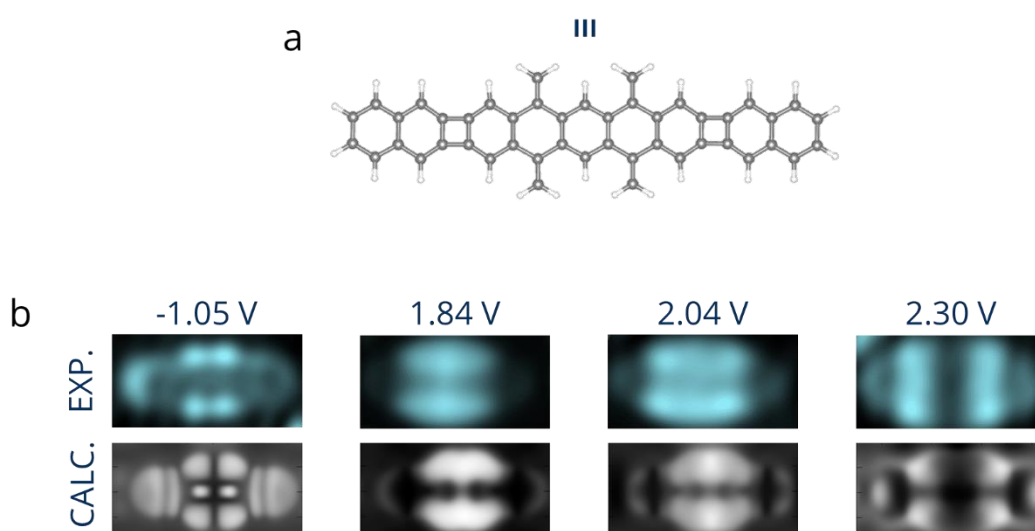


Figure 73: (a) Chemical structure of final molecule **III**. (b) Constant current conductance maps: Top row: Experimental maps. Bottom row: Calculated maps. Image parameters: $I = 200$ pA, size of all images: 3.5 nm x 1.7 nm.

8.2.8 Conclusion

In this part of the chapter, we demonstrated the tip-based transformation of two dimethylbenzenes into *p*-QDM units, thereby generating not only a new analogue of undecacene, but we have been able to study the effect of anti-aromatic moieties like cyclobutadiene and the change of hybridization of the functional groups, on the 1D framework of the molecule. While the isoundecacene is only a structural isomer of undecacene, this incorporation of non-benzenoid structures provided us with an opportunity of studying the relation between the interruption of aromaticity and electronic properties. This can be summarized by studying the anisotropy of induced current density (ACID) plots, as illustrated in Figure 74. ACID plots are used to

understand and visualize the delocalization and conjugation of all electronic states in a molecule [139].

The presence of clockwise currents in the naphthalene units of both **I** and **III** as shown in Figure 74a and Figure 74b respectively, indicates their aromatic nature, while a counter clockwise current in the four-membered rings, their anti-aromatic nature. For the final molecule **III**, we see a clockwise ring current around the pentacene unit, especially strong around the three central rings (Figure 74b), indicating once again the aromatic characteristics. This is in contrast with the precursor **I** (Figure 74a), where this feature is observed only locally on non-contiguous rings, and no significant directional current in the *p*-QDM units, suggestive of an interruption of aromaticity. This change in aromaticity is also observed experimentally, in the form of the slight widening of the bandgap as discussed in the previous section.

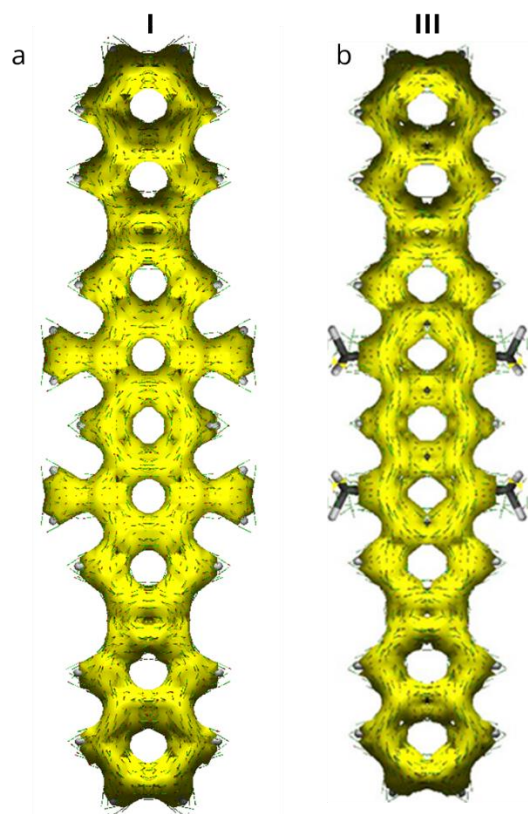


Figure 74: ACID plots. (a) Deoxygenated precursor **I**. (b) Final product **III**.

Therefore, we were successful in our goal of on-surface synthesis of isoundecacene, characterizing each reaction step and demonstrating experimentally the structure-conjugation properties.

8.3 On-surface synthesis of tetradecacene: 6-epoxy precursor

The precursor design follows the same principle of epoxy protection, which proved successful for the on-surface generation of dodecacene [131], and the isoundecacene presented in the previous section. However, since we have an additional naphthalene unit, it also means that we have an extra epoxy ring. The chemical structure of the precursor is shown in Figure 75.

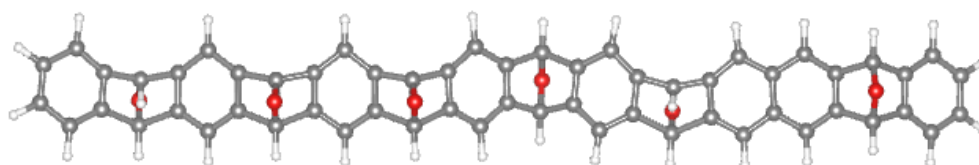


Figure 75: Tetradecacene precursor. Carbon atoms shown in grey, hydrogen in white and oxygen in red.

All rings are hexagonal benzene rings, the apparent distorted shape is due to non-planarity caused by the epoxy bridges.

8.3.1 Deposition on Au(111)

The molecules are flashed from a Silicon wafer as explained in the previous section. An overview of the surface is shown in the image below.

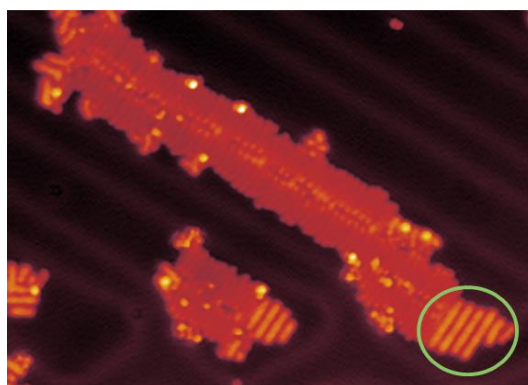


Figure 76: Overview of Au(111) after deposition of tetradecacene precursors. Image parameters: $V = 0.5$ V, $I = 30$ pA, size = 35 nm x 25 nm. Stack of tetradecacene precursors shown in green.

We observe that the coverage of the molecules is low and also that there is some chemical contamination present, as is common with this deposition technique.

Importantly, the molecules arrange themselves in stacks, as shown in the green circle in Figure 76.

We decided to take a closer look at these stacks, using a CO tip. The results are shown in Figure 77. The low bias constant current image with the functionalized tip is shown in Figure 77a. Its corresponding constant height image (Figure 77c) illustrates that not all the rings in the molecular structure are the same size. This could be due to the epoxy bridges, or in case of their cleaving like seen with the isoundecacene precursor, due to intermolecular interactions. In order to identify the position for pulsing, one must record a high bias STM topography, as has been done in the past for other acene precursors [131]. The high bias STM topography shows bright protrusions on each molecule, one of which has been highlighted by a red star (Figure 77b). We applied a constant height pulse at 2.5 V for five seconds at this position, as immediately recorded a post-pulse constant height image. This is shown in Figure 77d. We can see some subtle differences now in the molecular structure, namely that there are some low-energy states emerging near the pulse position, which could be indicative of dehydrogenation or spin states [140]. This could be caused by some intermediate and unanticipated reaction during pulsing, due to the intermolecular interactions within the stack.

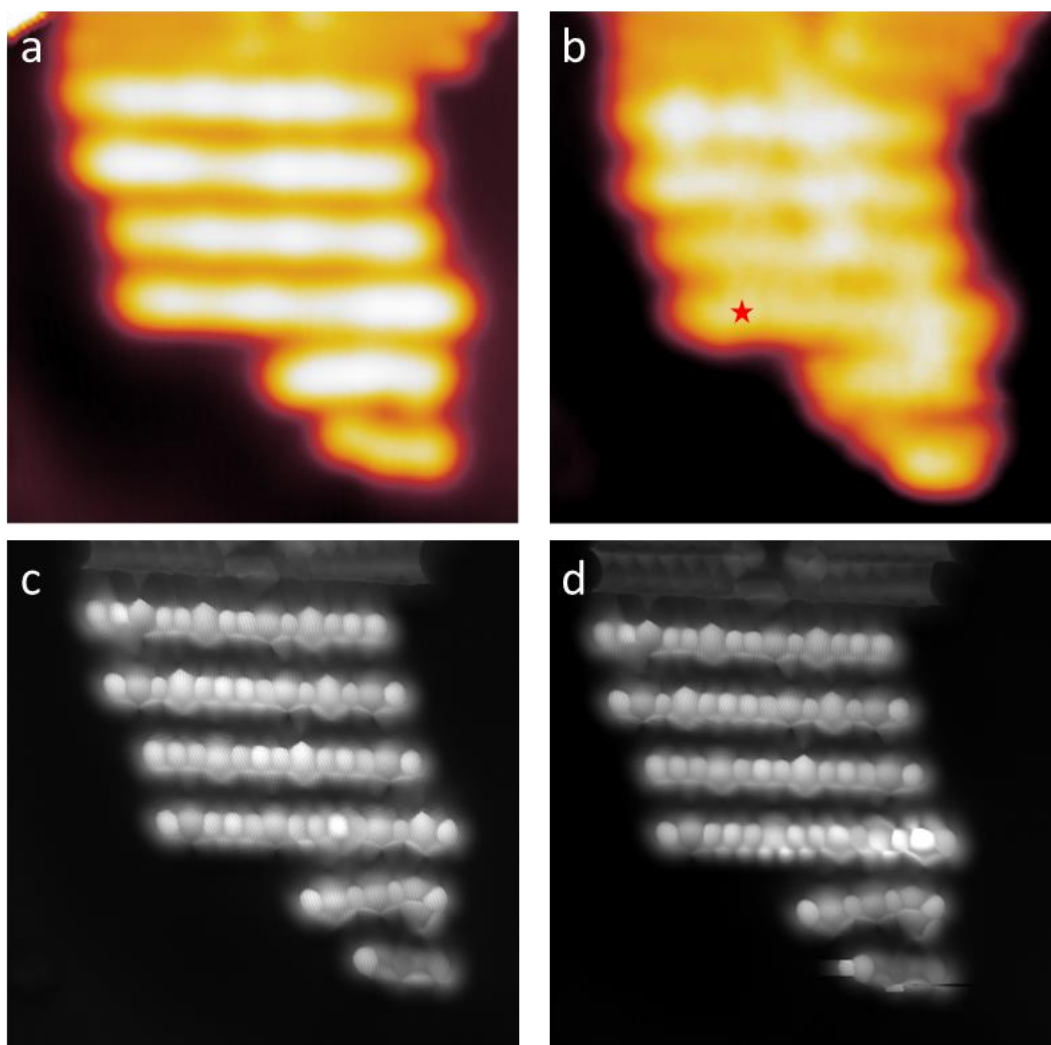


Figure 77: Close-up of a stack of tetradecacene precursors. (a) Constant current image with a CO-tip. Image parameters: $V = 0.5$ V, $I = 30$ pA. (b) Higher bias constant current image with a CO-tip showing position of pulse (red star). Image parameters: $V = 2$ V, $I = 30$ pA (c) Constant height image with CO-tip, before pulsing. (d) Post-pulse constant height image with CO-tip. Constant height pulse parameters: 2.5 V, 600 pA. Image parameters for (c) and (d): $V = 6$ mV. All images size: 5.5 nm^2

Therefore, we decided to isolate the molecules via lateral manipulation first, before any pulsing operations.

Figure 78 shows an isolated molecule. The high bias constant current image shows four features, which can be described as protrusions or bumps. These have been shown with arrows in Figure 76a. The corresponding constant height CO image further illustrates that these bumps translate to enlarged rings in the molecular structure, clearly visible in Figure 76c. The arrows also indicate the position of the constant height pulse (2.5 V, 400 pA, 5 seconds) that we applied to the molecule. The post pulse constant current image shown in Figure 76b shows that only one bump (green arrow in Figure 76a) has been removed. The corresponding CO image shown in Figure 78d also demonstrates that the previously enlarged ring (Figure 76c shown with green triangle) has been converted to a benzene ring, signifying that the pulse-induced chemical conversion has worked. However, all the other enlarged rings (Figure 76d) shown by red triangles) remain unchanged, even after repeated pulsing operations.

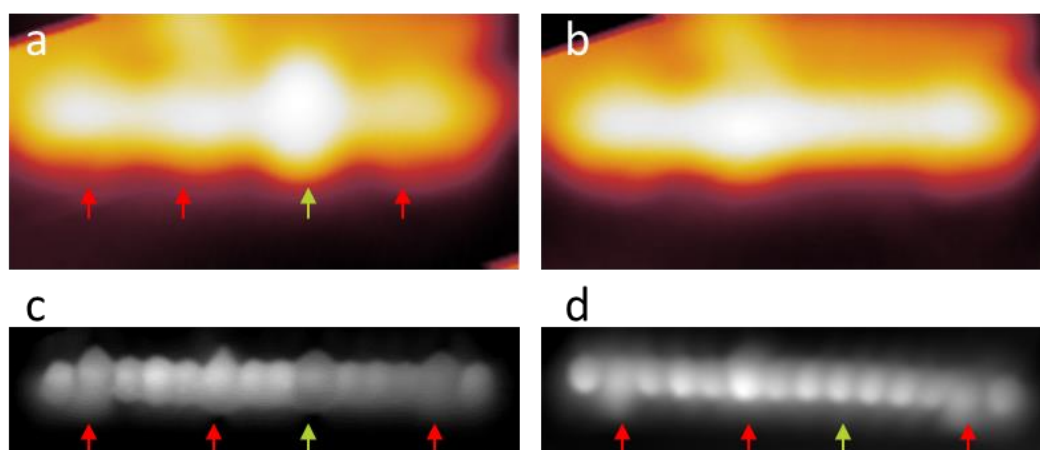


Figure 78: Pre and post-pulse images of isolated molecule. (a) Pre-pulse constant current image showing pulse positions with arrows. (b) Post-pulse constant current image showing only the bump at the position of the green arrow in (a) disappearing. (c) Pre-pulse constant height image. (d) Post-pulse constant height image, with the conversion of one ring from large to small (green arrow). Image parameters: (a) - (b): $V = 2\text{ V}$, $I = 30\text{ pA}$, size: $4\text{ nm} \times 2\text{ nm}$. (c) - (d): $V = 5\text{ mV}$, size: $4\text{ nm} \times 1\text{ nm}$. Pulse parameters: Constant height pulse, $V = 2.5\text{ V}$, $I = 400\text{ pA}$.

We will now summarize the work of many weeks, where we isolated and pulsed several molecules, always to find that there was one or more unpulsable protrusions that appeared as enlarged rings in the bond-resolved STM images. As demonstrated in Figure 79, the position and number of these enlarged or distorted rings (red arrows) varied, and no molecules were ever observed without at least one of these distorted features. Of note was also our observation that quite often, the distorted rings corresponded to the position of the epoxy bridges in the precursors. The simplified chemical structure provided in Figure 79 demonstrates this fact.

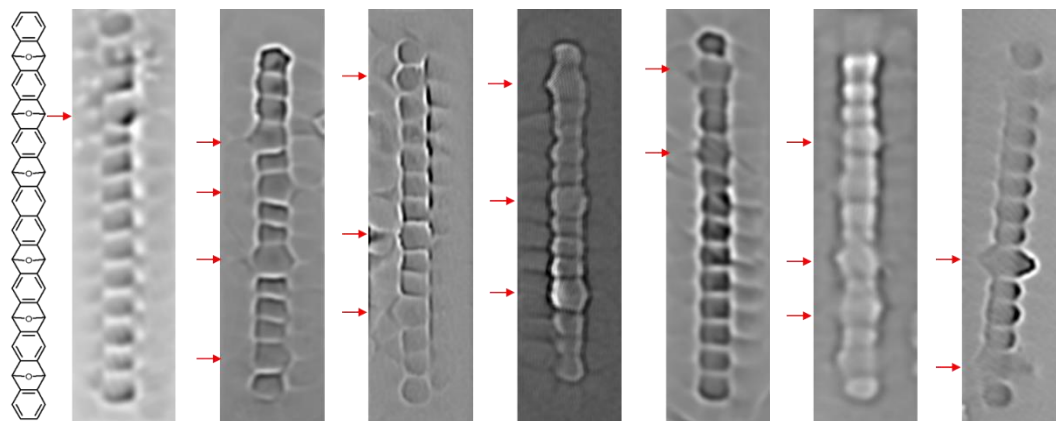


Figure 79: Simplified chemical structure and Laplace filtered constant height images with CO tip showing multiple molecules. Red arrows mark the position of distorted rings. Image parameters: $V = -1$ mV, size: 4 nm x 1 nm

8.3.2 nc-AFM images of tetradecacene precursors

To gain further information about the molecules and the enlarged rings that we observed on every molecule performed nc-AFM using the qPlus sensor on a pulsed molecule. The results have been shown in Figure 80. The post-pulse constant current STM image, recorded with a CO functionalized tip (Figure 80a) shows the same features we had observed previously. The molecule has loop-like features, as the position of enlarged rings, shown with red arrows in the nc-AFM image with a CO-tip (Figure 80b), which is also evident in the constant height CO image, shown in Figure 80c. This means that all the distortions we observed in Figure 79 are the same as what we observe in the purely topographical nc-AFM image (Figure 80b). There is also a defect next to the molecule, as marked with the red asterisk, whether this is causing the ring distortion is unclear, but the other two distortions are not due to any nearby defects, rather they exist natively.

Another important conclusion from this figure is that, the distortions are not caused by pulsing, since as we saw in the pre- and post-pulse comparison (Figure 78), the precursors have these defects as deposited.

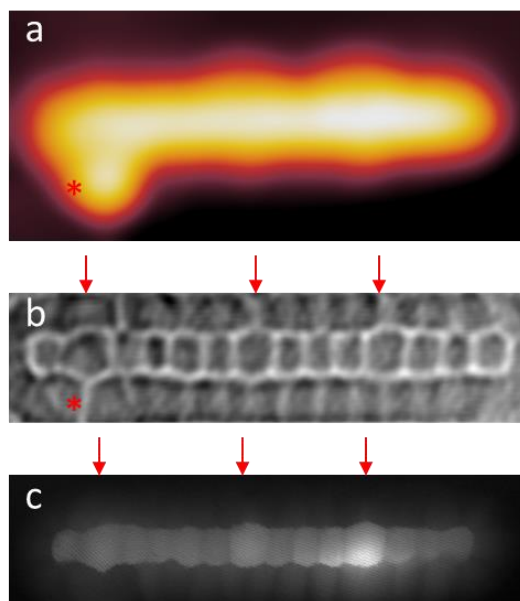


Figure 80: Post-pulse molecule. (a) Constant current image with CO tip recorded at $V = 0.1$ V, $I = 100$ pA. (b) nc-AFM with a CO tip: 4.5×1.5 nm

8.3.3 Electronic properties of tetradecacene precursors

Since the electronic properties of acenes, especially the bandgap is of vital importance to investigate, we performed STS and dI/dV measurements on the pulsed precursors. We also wanted to see if and how the conjugation was affected by the distorted rings. The results of this investigation on a molecule with one distortion have been shown in Figure 81. The STS was recorded over many positions on the pulsed molecule, an example has been shown in Figure 81a. There were several low intensity and broad peaks present, and therefore a bias sweep was performed when measuring the dI/dV maps. This process has been explained in the previous section of isoundecacene. The conductance maps shown in Figure 81b are the ones which had the highest contrast and incidentally match with the peak maxima. It is unfortunately quite clear, that there are localized electronic states at the position of the distortion, effectively breaking the conjugation. This means that the distorted rings not only affect the structural, but also electronic properties of the molecule.

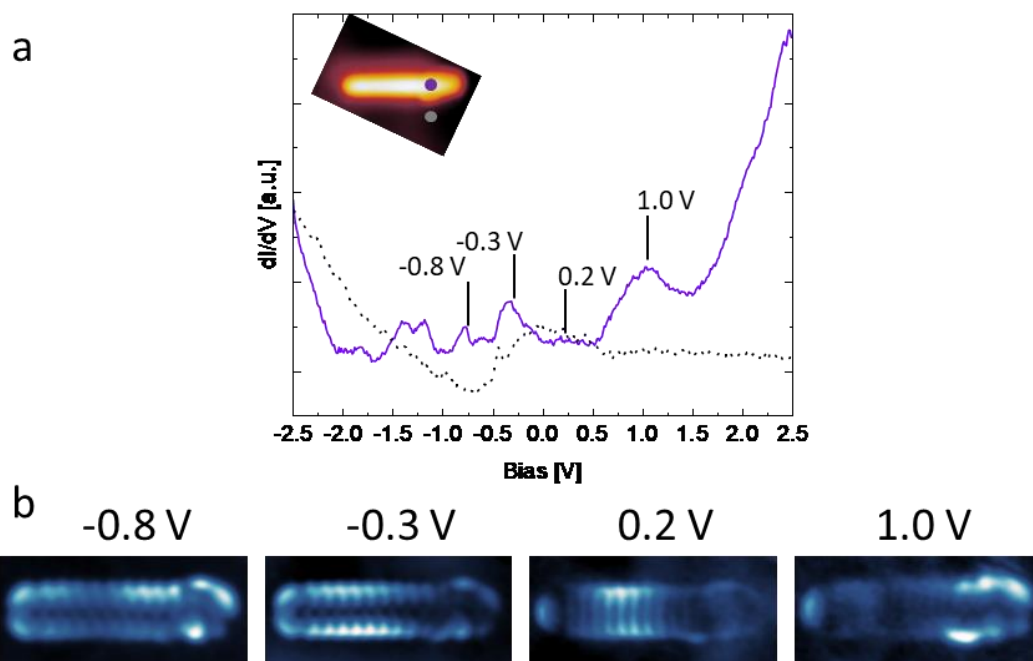


Figure 81: STS and dI/dV maps one molecule with one distortion. (a) Constant height STS recorded at positions marked in the inset. (b) Constant current dI/dV maps showing broken conjugation. Image parameters: Inset in (a): $V = 0.1$ V, $I = 300$ pA. (b) $I = 300$ pA. All images 4.5 nm \times 2 nm.

We performed STS measurements on multiple molecules, with varying number and position of distortions, with always the same result, i.e., the conjugation was broken and localized electronic states were present at the position of the distortion.

Figure 82 shows a molecule that has been pulsed and has two loop-like features or distortions remaining. The high bias constant current topography image in Figure 82a shows the profiles along which the line scans were taken and the results of the line scans themselves are illustrated in Figure 82b. We can clearly prove that these features have no contribution to the apparent height and are electronic in nature, stemming from the ring distortions clearly visible in all BR-SPM images.

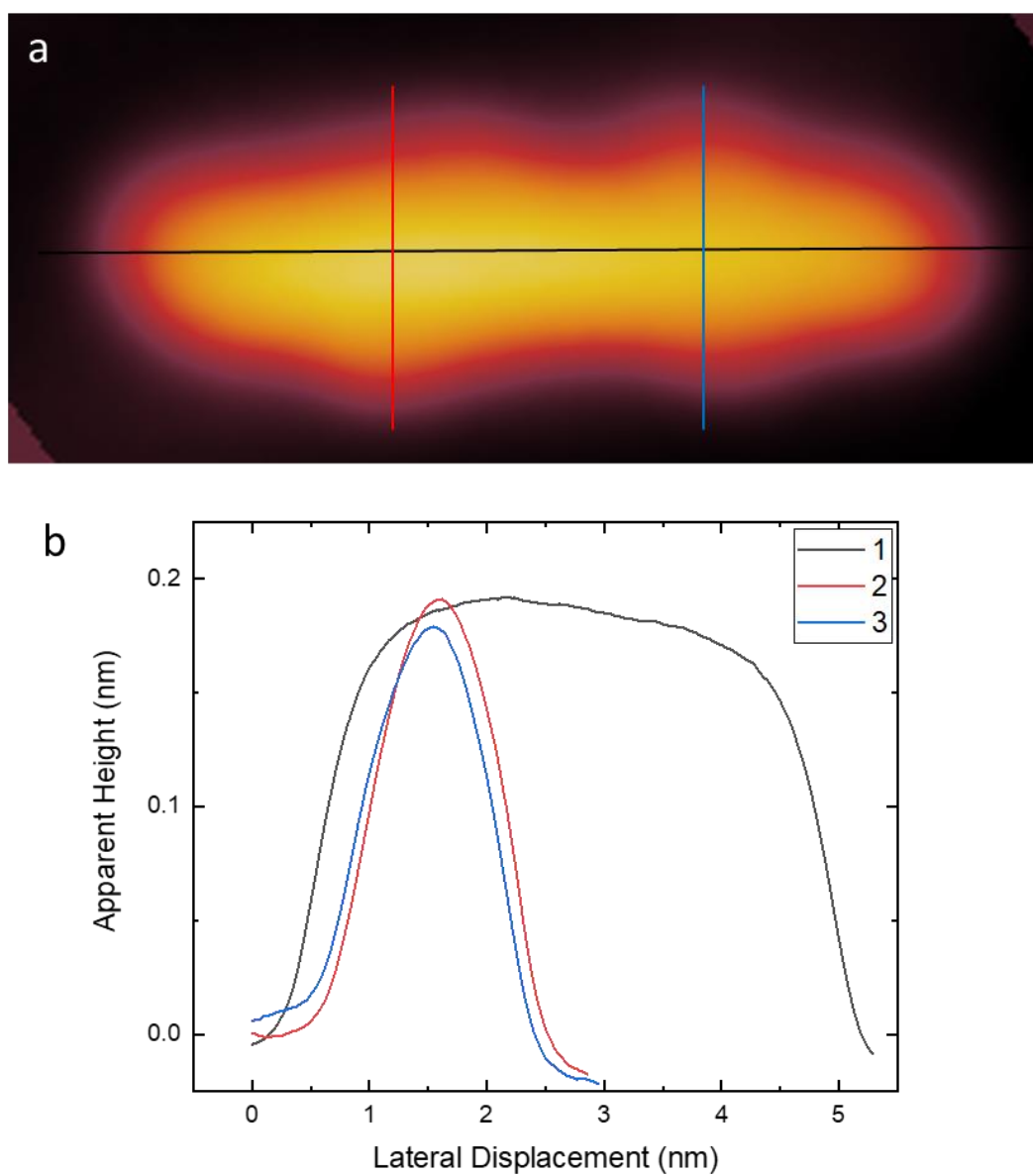


Figure 82: Line scan over pulsed molecule with two distortions. (a) Line scan taken along molecule and over the loop-like distortions. (b). Line profiles showing no contribution of the loop-like features to the apparent height. Image parameters: (a) $V = 2$ V, $I = 30$ pA, size: 5.3 nm x 2.3 nm

8.3.4 Discussion on enlarged rings

The origin of this electronic and structural disruption was the subject of much debate and a few possibilities have been presented in this section.

Epoxy to ketone conversion

One possibility is that one or more of the epoxy bridges were converting to a ketone, as shown in Figure 83. This would mean that we would not be able to pulse it away, and of course, there would be a contribution of the double bond towards the localization of electronic states. However, this conversion would necessitate the creation of a radical state in the molecule, since the valence requirements of the carbon will no longer be met, and experimentally this should manifest as a Kondo peak [140, 141] or spin-flip transition [142]. We found no evidence of either. However, it is possible that if the exchange coupling of the spin transition states is too low, or the radical character is being quenched by the interaction with the Au(111) surface, we will not see it electronically. Thus, while unlikely, we cannot absolutely rule out this conversion.

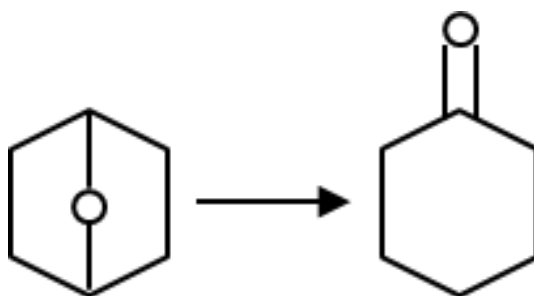


Figure 83: Simplified schematic of epoxy to ketone conversion. Double bonds and hydrogens have been excluded.

Epoxy to stereo hydrogen conversion

In this scenario, the precursor would be presumably lose the epoxy bridges and the participating carbon atoms would have either one or more pairs of stereo hydrogens, illustrated schematically in Figure 84. This possibility is easier to dispel, since it is very well-known that stereo hydrogens are easily pulsed away, often even scanning the molecule at higher biases suffices [130, 133, 143, 144]. However, in our case, we cannot get rid of these distortions even by pulsing at extremely high bias and current parameters.

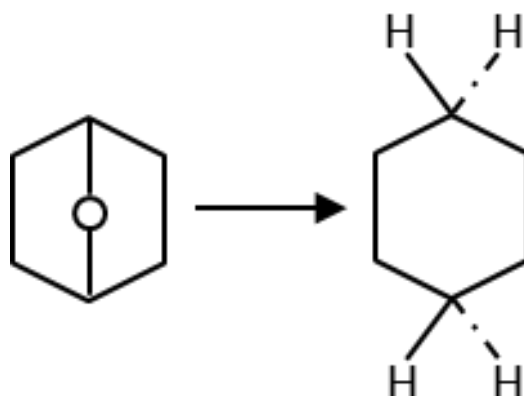


Figure 84: Simplified schematic of epoxy conversion to ring with one or more stereo hydrogens.

Multiple Clar sextets

It has been theorized that longer acenes should have an open shell character [145-147], and recent results have corroborated this experimentally as well [132, 133]. Another hypothesis is that with increasing the 1D length, the probability of having more than one Clar sextet is promoted [148]. This would give rise to much more stable molecular species based on the Clar's sextet rule [149]. This would entail a different on-surface reaction pathway, as illustrated in Figure 85.

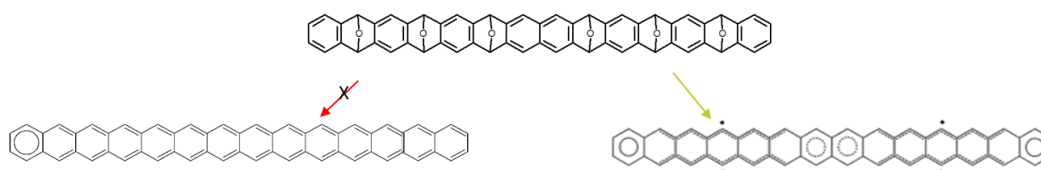


Figure 85: Simplified schematic representation of possible reaction pathway.

The empirical confirmation of this is hard to come by, since it is the structure shown via the green arrow is only one of the many possible resonant structures. Additionally, it is very difficult to conclusively prove that additional Clar sextets would manifest as larger rings; which is what we repeatedly observe in our molecules.

While it is challenging to quantitatively diagnose the nature of our distorted rings, the series of constant height CO tip images and the nc-AFM images shown in Figure 79 and, respectively, pointed to a probable correlation between the position of the epoxy groups and the distortions. This led us to believe that possibly such a high number of epoxy groups was prevaricating us from completing a successful on-surface reaction and therefore, we decided to redesign the precursor for tetradecacene.

8.4 4 epoxy tetradecacene precursor

After much brainstorming, our chemistry collaborators implemented a new design, wherein they reduced the number of epoxy groups, and incorporated stereo hydrogens in two of the benzene rings. This new structure has been shown in Figure 86. This redesign was guided in part by the fact that we found a close correlation between epoxy bridges and distortions (Figure 79), and also due to the successful on-surface synthesis of dodecacene, which had fewer of these epoxy protection groups [131].

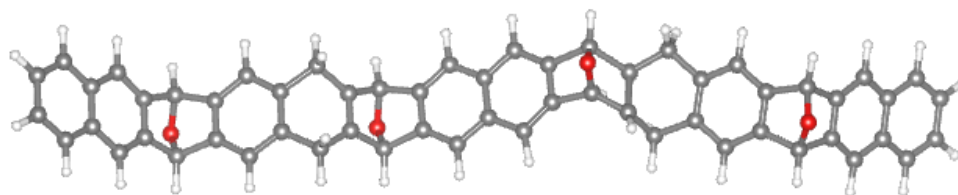


Figure 86: Chemical structure of new precursor.

8.4.1 Deposition on Au(111)

Evaporated similarly from an Si wafer, the new precursors adsorb the same way as the six epoxy version. An overview is shown in Figure 87. They are once again self-assembled in stacks, and molecules had to be isolated by lateral manipulations.

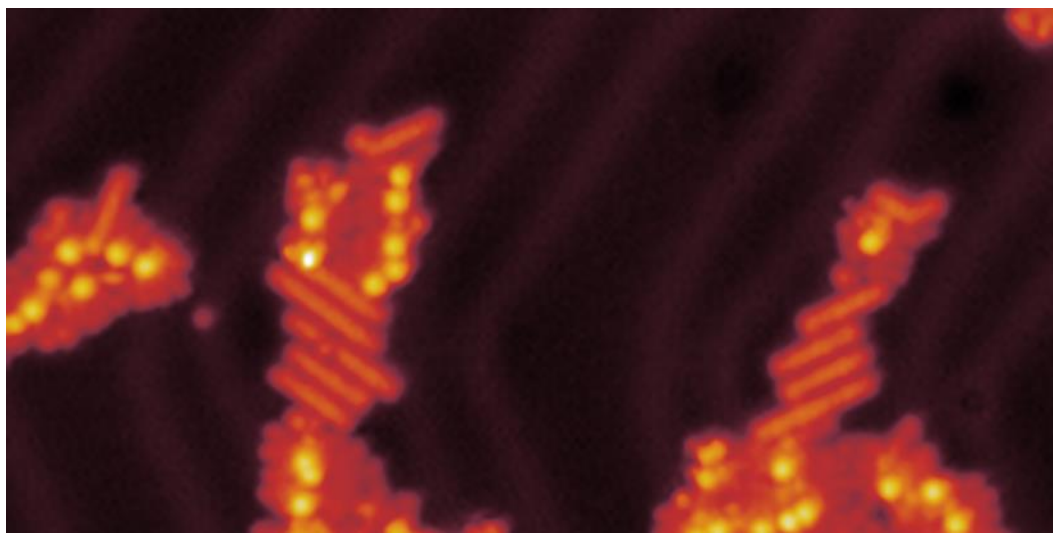


Figure 87: STM over after deposition. Constant current image recorded at $V = 0.5$ V, $I = 10$ pA, size: 30 nm x 15 nm.

8.4.2 Attempts at on-surface synthesis

Figure 88 shows our attempts at the on-surface synthesis of tetradecacene from this new precursor. The molecule is first isolated and a low bias CO-tip constant current topography image recorded, and is shown in Figure 88a. We proceed in the usual way, where we take a high bias image next, to identify the position of the protrusions, in order to pulse them away. This has been shown in Figure 88b. We can already observe that while there are protrusions (shown via the green stars), that are well-defined and bright, we also see the loop-like features that we have come to recognize as distortions and unpulsable. The constant height CO tip image taken before the pulse is shown in Figure 88c. The simplified chemical structure added to the bottom of the column shows a good agreement with the experimentally observed enlarged rings, and the epoxy groups in the molecule.

We performed a constant height pulse at 2.5 V for 5 seconds, which elicited a current of 600 pA, the results of which are shown in the right column of Figure 88. No change is discernible in the CO-tip constant current image taken at low bias, as illustrated by Figure 88d. The high bias image in Figure 88e, however, shows clearly that the protrusions or pulsable bumps that had been designated by the green stars in Figure 90b, have indeed been pulsed away. The loop-like features remain, and even with very high bias and current pulses, we were not able to get rid of them. Lastly, we see from Figure 88f that at the position of the successful pulses, two of the enlarged rings have been converted to smaller benzene rings while the distortions continue to manifest as

larger rings. Additionally, we see evidence of low energy states on the left side of the molecule, meaning that we might have a radical at that position [140].

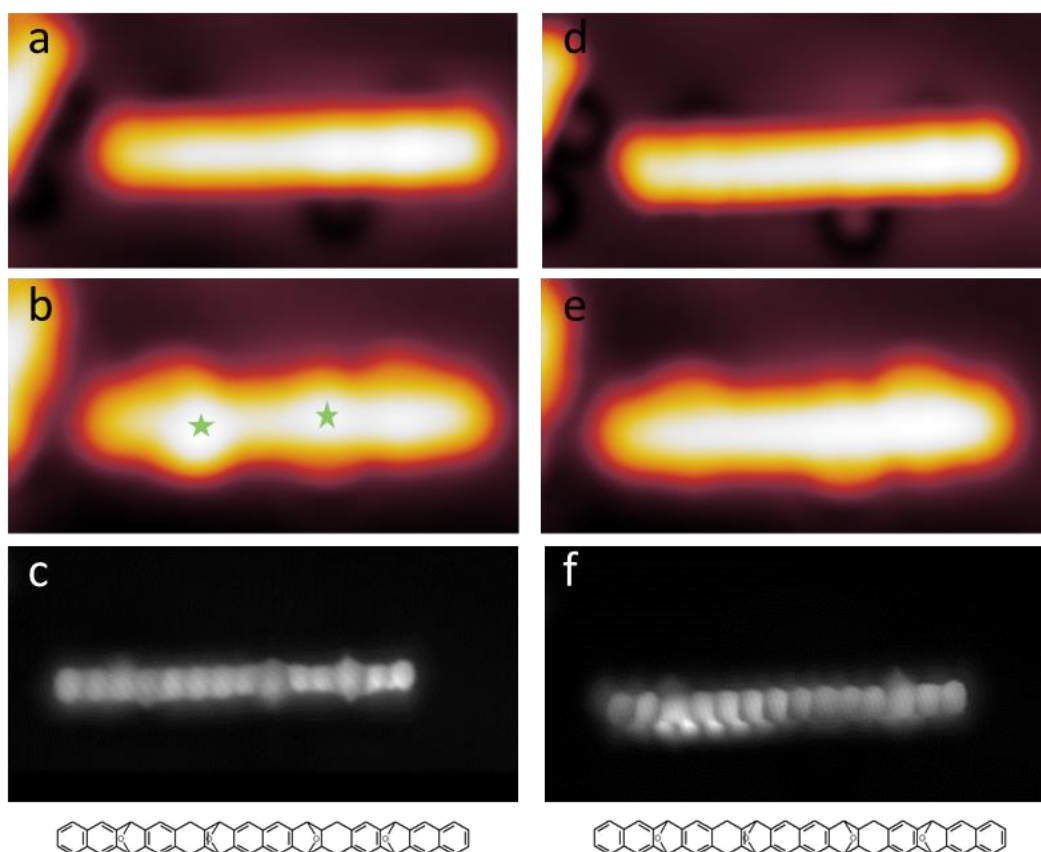


Figure 88: Pre and post-pulse images of isolated molecule with simplified chemical structure of precursor molecule. (a) - (c) Pre-pulse images. (a) Low bias constant current image. (b) High bias constant current image showing pulsable bump with green star and already existing distortions. (c) Pre-pulse constant height image. (d)- (f) Post-pulse images. (d) Low bias constant current image. (e) High bias constant current image showing the pulsable bump disappearing. (f) Post-pulse constant height image with CO tip. Image parameters: (a), (d): $V = 0.1$ V, $I = 100$ pA. (b), (e): $V = 2$ V, $I = 100$ pA. (c), (f): $V = -1$ mV. All images size: 5 nm x 2.5 nm. Pulse parameters: Constant height pulse, $V = 2.5$ V, $I = 400$ pA.

8.4.3 Electronic properties of new tetradecacene precursors

Performing STS on the molecule described above, we find that the spectrum shows broad peaks (Figure 89a). We performed an incremental bias sweep and found that the brightest conductance maps were recorded at resonances found at -0.3 V and 1.6V. These maps have been shown in Figure 89b. We see quite clearly that above Fermi energy, there are localized states at three points along the molecule, each

corresponding to the three distortions we found on this molecule (shown in the inset of Figure 89a). Below Fermi energy, we do not observe such strong localizations, however, we do notice that the conjugation is broken.

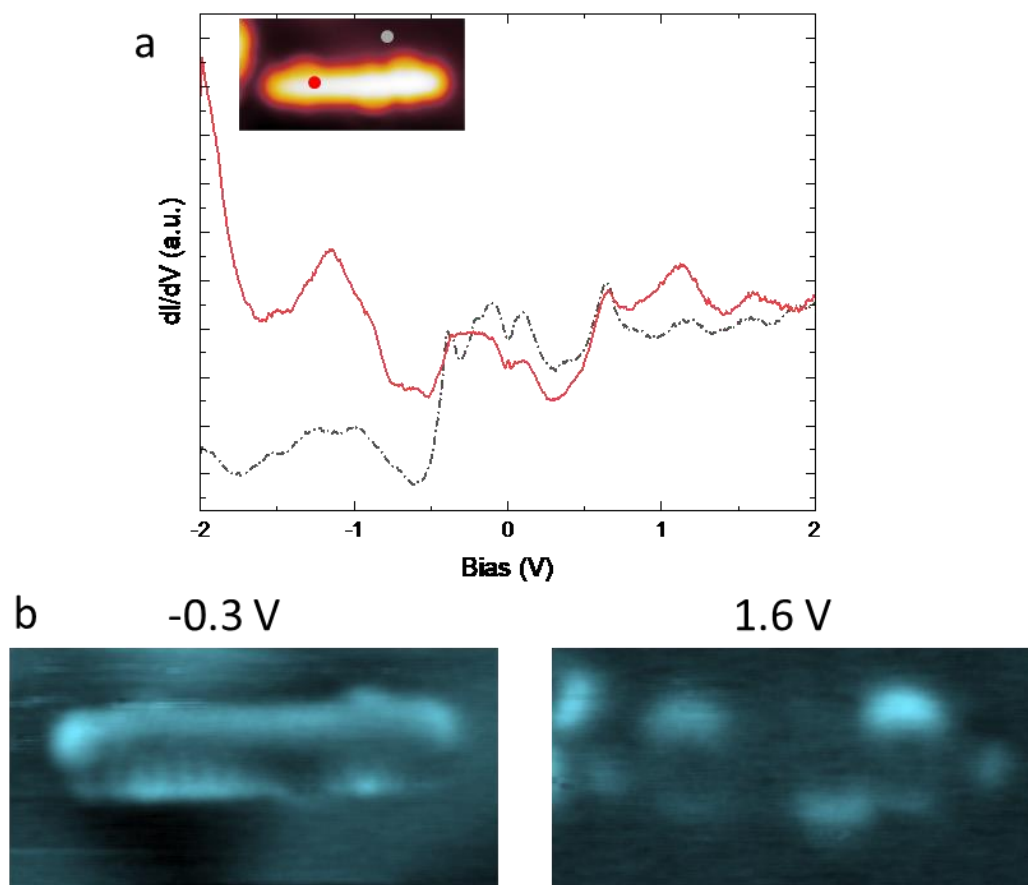


Figure 89: STS and dI/dV maps one molecule with three distortions. (a) Constant height STS recorded at positions marked in the inset. (b) Constant current dI/dV maps showing broken conjugation at positions of distorted rings. Image parameters: Inset in (a): $V = 2$ V, $I = 300$ pA. (b) $I = 300$ pA. All images 5 nm \times 2.5 nm.

We tried the isolation and pulsing operations on multiple other molecules, an example of which is shown in Figure 90. The left column are the pre-pulse images and the right column, the post-pulse. The low bias CO-tip constant current image is the usual planar and featureless in appearance (Figure 90a), while the high bias image shows three pulsable bumps this time, marked with green stars in Figure 90b. These are also the position where sequential constant height pulses are administered at 2.5 V for 5 seconds. We also observe loop-like features, in close proximity to the pulsable bumps. Finally, the constant height CO-tip image in Figure 90c shows us through the aid of the

simplified chemical structure that most of the enlarged rings correspond yet again to epoxy groups in the precursor.

Post pulsing, the low bias constant current image shows a small but distinct change in the molecular topography (Figure 90d). The high bias image (Figure 90e) again shows us the distortions, this time two in number, and the disappearance of the three bright protrusions or bumps, meaning that at least at the position marked by the three green stars in Figure 90b, our pulsing was successful. We already know now from long experience that the loop-like features are impossible to remove through pulses.

The CO-tip constant height image in Figure 90f shows us two things; some of the rings are reduced in size as they responded to pulses, this is borne out in both constant height and constant current images as discussed, and secondly, we observe low energy states yet again, indicative of one or more radicals.

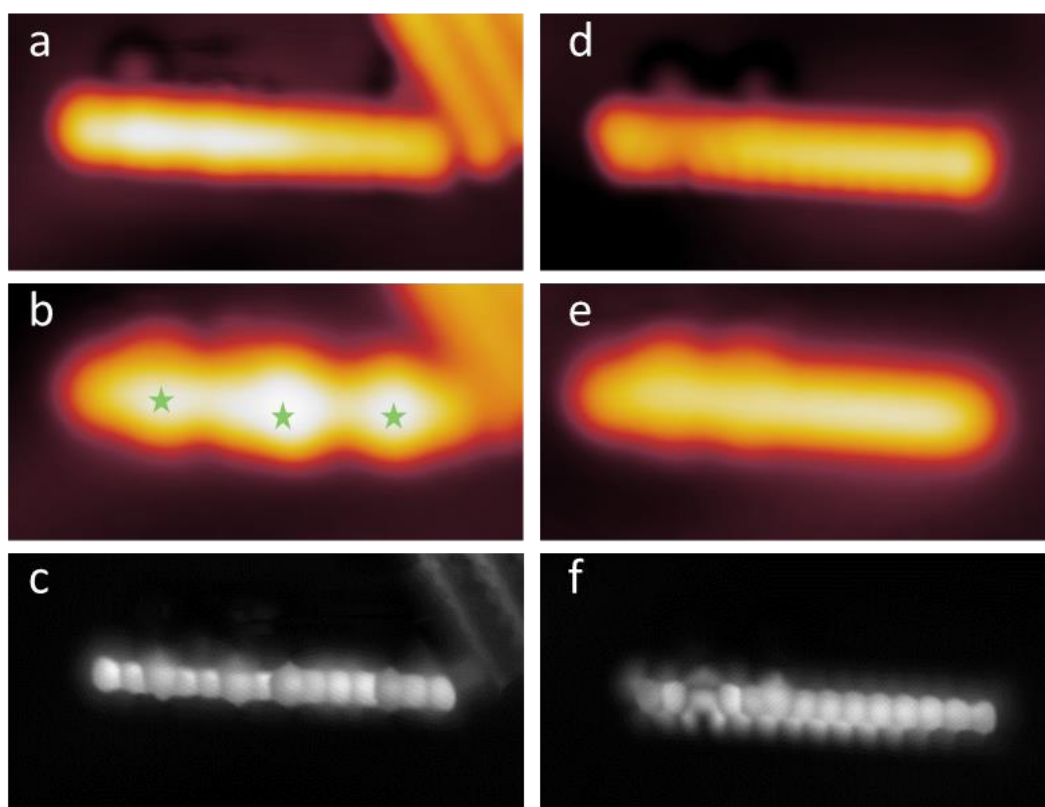


Figure 90: Pre and post-pulse images of isolated molecule with simplified chemical structure of precursor. (a) - (c) Pre-pulse images. (a) Low bias constant current image. (b) High bias constant current image showing pulsable bumps with green stars and already existing distortions. (c) Pre-pulse constant height image. (d)- (f) Post-pulse images. (d) Low bias constant current image. (e) High bias constant current image showing the pulsable bump disappearing. (f) Post-pulse constant height image with CO tip. Image

parameters: (a), (d): $V = 0.1$ V, $I = 100$ pA. (b), (e): $V = 2$ V, $I = 100$ pA. (c), (f): $V = -1$ mV. All images size: 5 nm x 2.5 nm. Pulse parameters: Constant height pulse, $V = 2.5$ V, $I = 500$ pA.

The electronic investigation of this molecule yielded a surprise. The STS curve shown in Figure 91a was taken at the position of the red dot shown in the inset image and shows the by now standard multiple broad peaks. However, a narrow spectrum taken at the position marked with the black dot, shows a symmetric step-like feature, centred around the Fermi energy (Figure 91b). We would like to point out that this spectrum was taken at the position of the low energy states visible in Figure 91d and Figure 91f.

For the first time, we observed experimental evidence of an open shell attribute in our molecule, as evidenced by the symmetric peaks found after taking a second derivative of the STS curve from Figure 91b, that has been shown in Figure 91c. The position of the peak maximum/minimum is at ± 42 mV, and these features are attributed to the spin transition or flip, through inelastic excitation from the ground singlet state to the excited triplet state. This phenomenon was recently reported by two different groups that successfully synthesised tridecacene [133] [132]. However, they reported contrasting singlet-triplet, as well as electronic gaps. Our singlet-triplet gap is quite small, around 84 mV.

This molecule, was quite mobile and therefore the constant current conductance maps had to be recorded at relatively low current values (Figure 91d and Figure 91e). This affected the resolution and intensity of features, but as discernible in Figure 91d, the conjugation is yet again broken, and we see localized states at the position of the distortions.

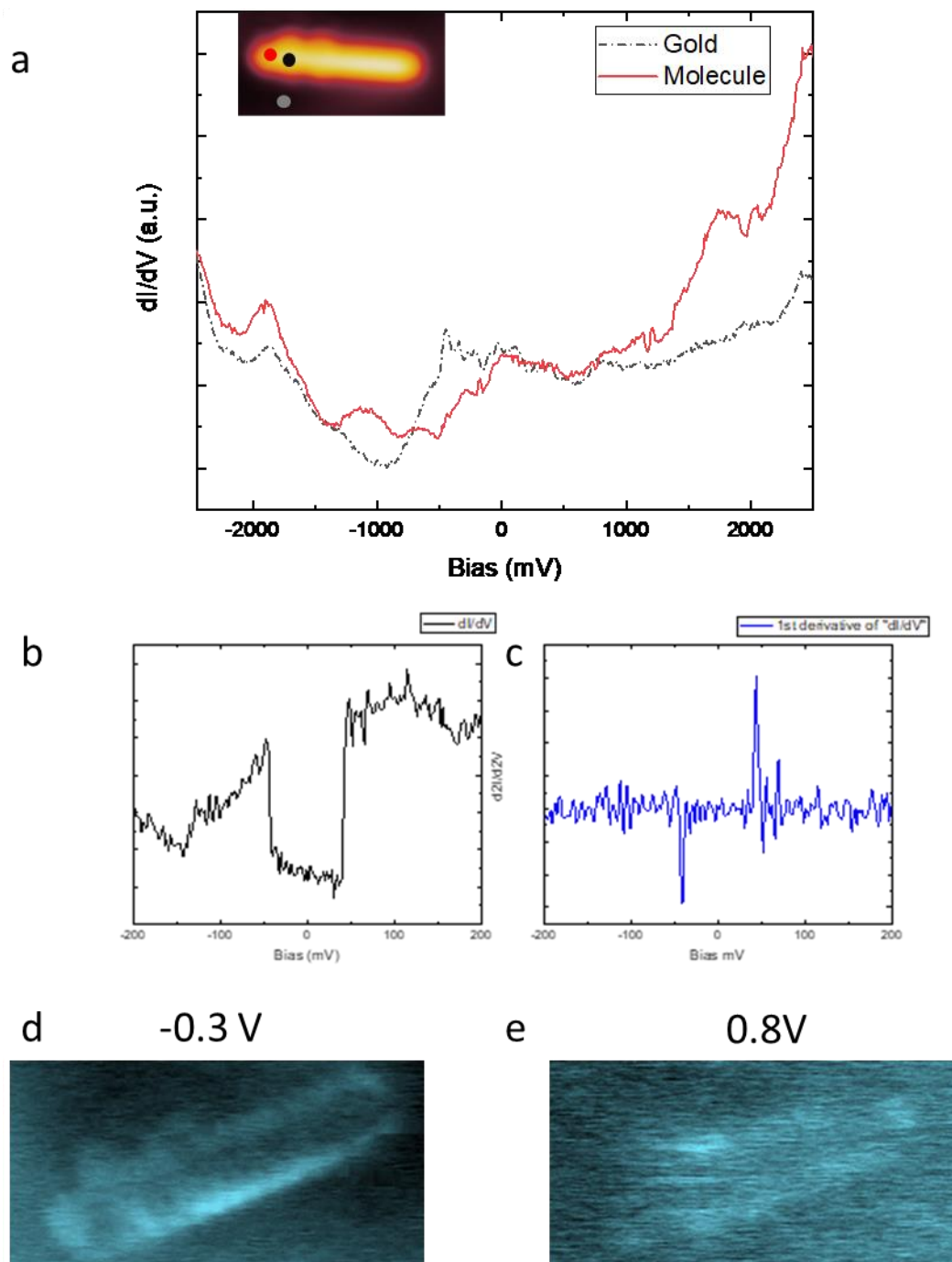


Figure 91: STS and dI/dV maps molecule with two distortions. (a) Constant height STS recorded at positions marked in the inset. (b) Narrower bias range of (a) showing a specific feature around zero bias. (c) Second derivative of (b) showing the spin excitation at 42 mV, either side of zero bias. (d) - (e): Constant current dI/dV maps showing broken conjugation at positions of distorted rings. Image parameters: Inset in (a): $V = 2$ V, $I = 100$ pA. (d) and (e): $I = 50$ pA. All images 5 nm x 2.5 nm.

8.5 Summary

The voltage pulse induced on-surface synthesis of the isoundecacene isomer was a success and we were able to probe the structure and electronic properties of the molecule, starting from the as-deposited precursor, intermediate species and the final target molecule.

The same pulse-induced synthesis of tetradecacene starting from two different precursors ran into similar roadblocks. We were able to unambiguously correlate the distortions in the molecular structure to the breaking of conjugation, and never found any molecule without at least one such distortion.

We were also able to demonstrate that these distortions existed on the molecules as deposited and were not induced as a result of tip-based manipulations.

As discussed, trickier is the assignation of these distortions to any chemical species. Since it corresponds relatively well to the epoxy groups in the precursor, it is perhaps possible that the epoxies are undergoing an unwanted chemical conversion during synthesis or deposition, into ketones or pyrillium moieties. These are, after all a highly unstable and reactive class of molecules.

A way forward could be depositing these molecules in an atmosphere of atomic Hydrogen, or even attempting post-annealing operations in the same atmosphere. Hydrogen passivation is a well-known technique to protect dangling bonds at carbon atoms [144, 150] and quench radical states [151], therefore ameliorating any effects of uncontrolled epoxy to ketone conversions or other unexpected reactions.

9 Summary and outlook

As rightly said, whatever has a beginning, must have an end and this chapter presents a summary of the experimental work undertaken in this thesis.

Chapter 6 presented two different molecules, both interesting in their self-organisation on an Au(111) surface, but as demonstrated not well-suited towards 2D-COFs.

Chapter 7 demonstrated the successful use of tip-based manipulation techniques to conformational change two donor-acceptor type molecules, in the first case by tuning the planarity and in the other, reversibly switching conformations. For the first case of the thianthrene based molecule, electronic investigations also revealed that the two different kinds of self-assemblies observed by virtue of the two different kinds of planarities of the molecules within this self-assembly, also manifested as a difference in the electronic properties as well. For the second case of the thiophene based molecules, we were able to show that the electronic properties remain unchanged across the two conformers.

Chapter 8 was exclusively dedicated to the on-surface synthesis of long acenes and acene analogues. The undecacene analogue with non-benzoid moieties was successfully synthesised via tip-induced dehydrogenation. By racking each step of the reaction with SPM techniques, we could demonstrate the creation of the intermediate and final reaction product and also understand how the electronic properties change with the change in aromaticity. This chapter also presented the attempted synthesis of tetradecacene from two different precursors, which although not entirely successful, yielded interesting results showing a correlation between enlarged rings and an interruption in conjugation. The chemical nature of this enlarged ring has also been discussed and a few possibilities put forth.

As an outlook, focus should be put on the generation of tetradecacene, perhaps through hydrogen passivation techniques as mentioned in Chapter 8. The electronic properties of long acenes are extremely interesting and it would be ideal to continue this group's tradition of synthesizing the longest acenes.

When it comes to the successful creation of 2D-COFs via bottom-up synthesis, much more rational design and dialogue between collaborating groups would be beneficial. This field of research is full of possibilities of designing novel materials and even when not completely successful, we still learn more about the native nature of molecules on surfaces, as illustrated by the homochirality of one of the molecules in Chapter 6.

An interesting avenue for long range order in on-surface synthesis of 2D-monolayers could be exploring metal-organic frameworks (2D-MOFs), as opposed to purely covalently linked frameworks. This can be done in several ways, either by choosing precursors with metal incorporation, co-deposition of metal atoms on to the substrate, or even extraction of surface atoms, and adatom mediated linkages [152, 153] [154] . This combines the bottom-up approach of 2D-COFs but with an increased modular approach, since the metal atoms or ions can be changed, giving rise to multiple nano-architectural options.

10 Bibliography

- [1] G. Binnig, H. Rohrer, C. Gerber, E. Weibel, "Surface Studies by Scanning Tunneling Microscopy", *Physical Review Letters*, **49** (1982) 57-61.
- [2] G. Binnig, C.F. Quate, C. Gerber, "Atomic Force Microscope", *Physical Review Letters*, **56** (1986) 930-933.
- [3] S.-W. Hla, K.-F. Braun, K.-H. Rieder, "Single-atom manipulation mechanisms during a quantum corral construction", *Physical Review B*, **67** (2003) 201402.
- [4] L.E.P. López, A. Rosławska, F. Scheurer, S. Berciaud, G. Schull, "Tip-induced excitonic luminescence nanoscopy of an atomically resolved van der Waals heterostructure", *Nature Materials*, **22** (2023) 482-488.
- [5] S. Sarkar, K.H. Au-Yeung, T. Kühne, A. Waentig, D.A. Ryndyk, T. Heine, G. Cuniberti, X. Feng, F. Moresco, "Adsorption and reversible conformational change of a thiophene based molecule on Au(111)", *Scientific Reports*, **13** (2023) 10627.
- [6] M. Alemani, M.V. Peters, S. Hecht, K.-H. Rieder, F. Moresco, L. Grill, "Electric Field-Induced Isomerization of Azobenzene by STM", *Journal of the American Chemical Society*, **128** (2006) 14446-14447.
- [7] S.-W. Hla, L. Bartels, G. Meyer, K.-H. Rieder, "Inducing All Steps of a Chemical Reaction with the Scanning Tunneling Microscope Tip: Towards Single Molecule Engineering", *Physical Review Letters*, **85** (2000) 2777-2780.
- [8] Q. Fan, J.M. Gottfried, J. Zhu, "Surface-Catalyzed C-C Covalent Coupling Strategies toward the Synthesis of Low-Dimensional Carbon-Based Nanostructures", *Accounts of Chemical Research*, **48** (2015) 2484-2494.
- [9] *Single Molecule Mechanics on Surface: Gears, Motors and Nanocars*, Springer Charm2022.
- [10] X. Zhang, C. Wolf, Y. Wang, H. Aubin, T. Bilgeri, P. Willke, A.J. Heinrich, T. Choi, "Electron spin resonance of single iron phthalocyanine molecules and role of their non-localized spins in magnetic interactions", *Nature Chemistry*, **14** (2022) 59-65.
- [11] B. Doppagne, T. Neuman, R. Soria-Martinez, L.E.P. López, H. Bulou, M. Romeo, S. Berciaud, F. Scheurer, J. Aizpurua, G. Schull, "Single-molecule tautomerization tracking through space- and time-resolved fluorescence spectroscopy", *Nature Nanotechnology*, **15** (2020) 207-211.
- [12] J. Cai, P. Ruffieux, R. Jaafar, M. Bieri, T. Braun, S. Blankenburg, M. Muoth, A.P. Seitsonen, M. Saleh, X. Feng, K. Müllen, R. Fasel, "Atomically precise bottom-up fabrication of graphene nanoribbons", *Nature*, **466** (2010) 470-473.

- [13] J.V. Barth, G. Costantini, K. Kern, "Engineering atomic and molecular nanostructures at surfaces", *Nature*, **437** (2005) 671-679.
- [14] K.H. Au-Yeung, S. Sarkar, S. Haldar, P. Das, T. Kühne, D.A. Ryndyk, P. Bhauriyal, S. Kaskel, T. Heine, G. Cuniberti, A. Schneemann, F. Moresco, "Tuning the Planarity of an Aromatic Thianthrene-Based Molecule on Au(111)", *The Journal of Physical Chemistry C*, **128** (2024) 1855-1861.
- [15] J. Homberg, A. Weismann, R. Berndt, "Making closed-shell lead phthalocyanine paramagnetic on Pb(100)", *Physical Review B*, **109** (2024) 165426.
- [16] F. Crick, *What Mad Pursuit*, Basic Books, New York, 1988.
- [17] B. Voigtländer, Introduction, in: B. Voigtländer (Ed.) *Scanning Probe Microscopy: Atomic Force Microscopy and Scanning Tunneling Microscopy*, Springer Berlin Heidelberg, Berlin, Heidelberg, 2015, pp. 1-11.
- [18] D.M. Eigler, E.K. Schweizer, "Positioning single atoms with a scanning tunnelling microscope", *Nature*, **344** (1990) 524-526.
- [19] N. Bohr, "The Quantum Postulate and the Recent Development of Atomic Theory¹", *Nature*, **121** (1928) 580-590.
- [20] A. Bukharaev, "Scanning Tunneling Microscopy. Edited by R. Wiesendanger and H.-J. Guntherodt", *Applied Magnetic Resonance*, **6** (1994) 601-602.
- [21] B. Voigtlaender, "Scanning Probe Microscopy: Atomic Force Microscopy and Scanning Tunneling Microscopy Bert Voigtländer", *MRS Bulletin*, **41** (2016) 165-166.
- [22] J. Bardeen, "Tunnelling from a Many-Particle Point of View", *Phys. Rev. Lett.*, **6** (1961) 57-59.
- [23] P.A.M. Dirac, "The Quantum Theory of Emission and Absorption of Radiation", *Proceedings of the Royal Society A*, **114** (1927) 243-265.
- [24] J. Tersoff, D.R. Hamann, "Theory of the scanning tunneling microscope", *Physical Review B*, **31** (1985) 805-813.
- [25] L. Gross, N. Moll, F. Mohn, A. Curioni, G.A. Meyer, F. Hanke, M. Persson, "High-resolution molecular orbital imaging using a p-wave STM tip", *Physical review letters*, **107** **8** (2011) 086101.
- [26] J. Fischer, M. Wendland, "On the history of key empirical intermolecular potentials", *Fluid Phase Equilibria*, **573** (2023) 113876.
- [27] J.E. Jones, S. Chapman, "On the determination of molecular fields.—I. From the variation of the viscosity of a gas with temperature", *Proceedings of the Royal Society of London. Series A, Containing Papers of a Mathematical and Physical Character*, **106** (1924) 441-462.

- [28] F.J. Giessibl, "High-speed force sensor for force microscopy and profilometry utilizing a quartz tuning fork", *Applied Physics Letters*, **73** (1998) 3956-3958.
- [29] F.J. Giessibl, "The qPlus sensor, a powerful core for the atomic force microscope", *Review of Scientific Instruments*, **90** (2019) 011101.
- [30] D. Sobel, *Longitude: The true story of a lone genius who solved the greatest scientific problem of his time*, Macmillan 2005.
- [31] I. Hickman, *Analog Electronics: Analog Circuitry Explained*, Elsevier Science 2013.
- [32] C.J. Chen, *Introduction To Scanning Tunneling Microscopy*, Oxford University Press 1993.
- [33] T.R. Albrecht, P. Grütter, D. Horne, D. Rugar, "Frequency modulation detection using high-Q cantilevers for enhanced force microscope sensitivity", *Journal of Applied Physics*, **69** (1991) 668-673.
- [34] S. Jaekel, R. Stoll, F. Berger, S. Hecht, L. Grill, "Azobenzene isomerization on a reactive copper surface by efficient decoupling with bulky side groups", *Surface Science*, **744** (2024) 122468.
- [35] A.S. Kumar, T. Ye, T. Takami, B.-C. Yu, A.K. Flatt, J.M. Tour, P.S. Weiss, "Reversible Photo-Switching of Single Azobenzene Molecules in Controlled Nanoscale Environments", *Nano Letters*, **8** (2008) 1644-1648.
- [36] L. Grill, "Large molecules on surfaces: deposition and intramolecular STM manipulation by directional forces", *Journal of Physics: Condensed Matter*, **22** (2010) 084023.
- [37] F. Moresco, G. Meyer, K.-H. Rieder, H. Tang, A. Gourdon, C. Joachim, "Recording Intramolecular Mechanics during the Manipulation of a Large Molecule", *Physical Review Letters*, **87** (2001) 088302.
- [38] N. Lorente, C. Joachim, Rotations of Adsorbed Molecules Induced by Tunneling Electrons, in: C. Joachim (Ed.) *Building and Probing Small for Mechanics*, Springer International Publishing, Cham, 2020, pp. 181-194.
- [39] K.H. Au-Yeung, S. Sarkar, T. Kühne, O. Aiboudi, D.A. Ryndyk, R. Robles, N. Lorente, F. Lissel, C. Joachim, F. Moresco, "A Nanocar and Rotor in One Molecule", *ACS Nano*, **17** (2023) 3128-3134.
- [40] K.H. Au-Yeung, S. Sarkar, T. Kühne, O. Aiboudi, D.A. Ryndyk, R. Robles, F. Lissel, N. Lorente, C. Joachim, F. Moresco, "Thermal with Electronic Excitation for the Unidirectional Rotation of a Molecule on a Surface", *The Journal of Physical Chemistry C*, **127** (2023) 16989-16994.

- [41] F. Eisenhut, C. Durand, F. Moresco, J.-P. Launay, C. Joachim, "Training for the 1st international nano-car race: the Dresden molecule-vehicle", *Eur. Phys. J. Appl. Phys.*, **76** (2016) 10001.
- [42] C. Joachim, G. Rapenne, "Molecule Concept Nanocars: Chassis, Wheels, and Motors?", *ACS Nano*, **7** (2013) 11-14.
- [43] A. van Venrooy, V. García-López, J.T. Li, J.M. Tour, A.V. Dubrovskiy, "Nanocars with Permanent Dipoles: Preparing for the Second International Nanocar Race", *J. Org. Chem.*, **85** (2020) 13644-13654.
- [44] A. Nickel, T. Lehmann, J. Meyer, F. Eisenhut, R. Ohmann, D.A. Ryndyk, C. Joachim, F. Moresco, G. Cuniberti, "Electronically Driven Single-Molecule Switch on Silicon Dangling Bonds", *Journal of Physical Chemistry C*, **120** (2016) 27027-27032.
- [45] F. Eisenhut, T. Kühne, J. Monsalve, S. Srivastava, D.A. Ryndyk, G. Cuniberti, O. Aiboudi, F. Lissel, V. Zobač, R. Robles, N. Lorente, C. Joachim, F. Moresco, "One-way rotation of a chemically anchored single molecule-rotor", *Nanoscale*, **13** (2021) 16077-16083.
- [46] T. Kühne, K.H. Au-Yeung, F. Eisenhut, O. Aiboudi, D.A. Ryndyk, G. Cuniberti, F. Lissel, F. Moresco, "STM induced manipulation of azulene-based molecules and nanostructures: the role of the dipole moment", *Nanoscale*, **12** (2020) 24471-24476.
- [47] G.J. Simpson, M. Persson, L. Grill, "Adsorbate motors for unidirectional translation and transport", *Nature*, **621** (2023) 82-86.
- [48] G.J. Simpson, V. García-López, A.D. Boese, J.M. Tour, L. Grill, "Directing and Understanding the Translation of a Single Molecule Dipole", *The Journal of Physical Chemistry Letters*, **14** (2023) 2487-2492.
- [49] L. Bartels, G. Meyer, K.H. Rieder, D. Velic, E. Knoesel, A. Hotzel, M. Wolf, G. Ertl, "Dynamics of Electron-Induced Manipulation of Individual CO Molecules on Cu(111)", *Physical Review Letters*, **80** (1998) 2004-2007.
- [50] L. Gross, F. Mohn, N. Moll, P. Liljeroth, G. Meyer, "The Chemical Structure of a Molecule Resolved by Atomic Force Microscopy", *Science*, **325** (2009) 1110-1114.
- [51] L. Gross, F. Mohn, N. Moll, B. Schuler, A. Criado, E. Guitián, D. Peña, A. Gourdon, G. Meyer, "Bond-Order Discrimination by Atomic Force Microscopy", *Science*, **337** (2012) 1326-1329.
- [52] L. Gross, N. Moll, F. Mohn, A. Curioni, G. Meyer, F. Hanke, M. Persson, "High-Resolution Molecular Orbital Imaging Using a p-Wave STM Tip", *Physical Review Letters*, **107** (2011) 086101.
- [53] R. Temirov, S. Soubatch, O. Neucheva, A.C. Lassise, F.S. Tautz, "A novel method achieving ultra-high geometrical resolution in scanning tunnelling microscopy", *New Journal of Physics*, **10** (2008) 053012.

- [54] C. Weiss, C. Wagner, C. Kleimann, M. Rohlfing, F.S. Tautz, R. Temirov, "Imaging Pauli Repulsion in Scanning Tunneling Microscopy", *Physical Review Letters*, **105** (2010) 086103.
- [55] G. Kichin, C. Weiss, C. Wagner, F.S. Tautz, R. Temirov, "Single Molecule and Single Atom Sensors for Atomic Resolution Imaging of Chemically Complex Surfaces", *Journal of the American Chemical Society*, **133** (2011) 16847-16851.
- [56] R. Wiesendanger, *Scanning Probe Microscopy and Spectroscopy: Methods and Applications*, Cambridge University Press, Cambridge, 1994.
- [57] G. Meyer, "A simple low-temperature ultrahigh-vacuum scanning tunneling microscope capable of atomic manipulation", *Rev. Sci. Instrum.*, **67** (1996) 2960-2965.
- [58] K. Besocke, "An easily operable scanning tunneling microscope", *Surf Sci.*, **181** (1987) 145-153.
- [59] B. Voigtländer, *Scanning Probe Microscopy Designs*, in: B. Voigtländer (Ed.) *Scanning Probe Microscopy: Atomic Force Microscopy and Scanning Tunneling Microscopy*, Springer Berlin Heidelberg, Berlin, Heidelberg, 2015, pp. 65-76.
- [60] P. Li, F. Ding, "Origin of the herringbone reconstruction of Au(111) surface at the atomic scale", *Science Advances*, **8** eabq2900.
- [61] D. Nečas, P. Klapetek, "Gwyddion: an open-source software for SPM data analysis", *Open Phys.*, **10** (2012) 181-188.
- [62] H. Brune, "Microscopic view of epitaxial metal growth: nucleation and aggregation", *Surface Science Reports*, **31** (1998) 125-229.
- [63] Z. Zhang, M.G. Lagally, "Atomistic processes in the early stages of thin-film growth", *Science*, **276** (1997) 377-383.
- [64] J.V. Barth, "Transport of adsorbates at metal surfaces: from thermal migration to hot precursors", *Surface Science Reports*, **40** (2000) 75-149.
- [65] L.K. Thomas, A. Kühnle, S. Rode, U. Beginn, M. Reichling, "Monolayer Structure of Arachidic Acid on Graphite", *The Journal of Physical Chemistry C*, **114** (2010) 18919-18924.
- [66] A.B. Ricks, K.E. Brown, M. Wenninger, S.D. Karlen, Y.A. Berlin, D.T. Co, M.R. Wasielewski, "Exponential Distance Dependence of Photoinitiated Stepwise Electron Transfer in Donor-Bridge-Acceptor Molecules: Implications for Wirelike Behavior", *Journal of the American Chemical Society*, **134** (2012) 4581-4588.
- [67] Y. Olivier, M. Moral, L. Muccioli, J.-C. Sancho-García, "Dynamic nature of excited states of donor-acceptor TADF materials for OLEDs: how theory can reveal structure-property relationships", *Journal of Materials Chemistry C*, **5** (2017) 5718-5729.

- [68] Q. Shen, H.-Y. Gao, H. Fuchs, "Frontiers of on-surface synthesis: From principles to applications", *Nano Today*, **13** (2017) 77-96.
- [69] C. Tönshoff, H.F. Bettinger, "Pushing the Limits of Acene Chemistry: The Recent Surge of Large Acenes", *Chemistry – A European Journal*, **27** (2021) 3193-3212.
- [70] S. Clair, D.G. de Oteyza, "Controlling a Chemical Coupling Reaction on a Surface: Tools and Strategies for On-Surface Synthesis", *Chemical Reviews*, **119** (2019) 4717-4776.
- [71] R. Lindner, A. Kühnle, "On-Surface Reactions", *ChemPhysChem*, **16** (2015) 1582-1592.
- [72] P. Ledwon, "Recent advances of donor-acceptor type carbazole-based molecules for light emitting applications", *Organic Electronics*, **75** (2019) 105422.
- [73] T. Wang, Q. Fan, L. Feng, Z. Tao, J. Huang, H. Ju, Q. Xu, S. Hu, J. Zhu, "Chiral Kagome Lattices from On-Surface Synthesized Molecules", *ChemPhysChem*, **18** (2017) 3329-3333.
- [74] L. Grill, M. Dyer, L. La, "erentz, M. Persson, MV Peters and S. Hecht", *Nat. Nanotechnol*, **2** (2007) 687.
- [75] A. Wiengarten, K. Seufert, W. Auwärter, D. Eciija, K. Diller, F. Allegretti, F. Bischoff, S. Fischer, D.A. Duncan, A.C. Papageorgiou, F. Klappenberger, R.G. Acres, T.H. Ngo, J.V. Barth, "Surface-assisted Dehydrogenative Homocoupling of Porphine Molecules", *Journal of the American Chemical Society*, **136** (2014) 9346-9354.
- [76] L. Lafferentz, V. Eberhardt, C. Dri, C. Africh, G. Comelli, F. Esch, S. Hecht, L. Grill, "Controlling on-surface polymerization by hierarchical and substrate-directed growth", *Nature Chemistry*, **4** (2012) 215-220.
- [77] Y.-P. Lin, O. Ourdjini, L. Giovanelli, S. Clair, T. Faury, Y. Ksari, J.-M. Themlin, L. Porte, M. Abel, "Self-Assembled Melamine Monolayer on Cu(111)", *The Journal of Physical Chemistry C*, **117** (2013) 9895-9902.
- [78] B. Fu, J. Geng, Z. Yang, Y. Zhang, S. Sun, Z. Ruan, H. Zhang, W. Xiong, G. Niu, Y. Zhang, L. Chen, L. Gao, J. Lu, J. Cai, "Coverage Modulated Transformation of the Supramolecular Assembly Structure of Brominated N-Heterocyclic Molecules on Au(111) Surfaces", *The Journal of Physical Chemistry C*, **127** (2023) 5833-5840.
- [79] O. Ourdjini, R. Pawlak, M. Abel, S. Clair, L. Chen, N. Bergeon, M. Sassi, V. Oison, J.-M. Debierre, R. Coratger, L. Porte, "Substrate-mediated ordering and defect analysis of a surface covalent organic framework", *Physical Review B*, **84** (2011) 125421.
- [80] H.-Y. Gao, H. Wagner, D. Zhong, J.-H. Franke, A. Studer, H. Fuchs, "Glaser Coupling at Metal Surfaces", *Angewandte Chemie International Edition*, **52** (2013) 4024-4028.

- [81] F. Ullmann, "Ueber symmetrische Biphenylderivate", Justus Liebigs Annalen der Chemie, **332** (1904) 38-81.
- [82] M. Lackinger, "Surface-assisted Ullmann coupling", Chemical Communications, **53** (2017) 7872-7885.
- [83] F. Moresco, J. Krüger, Unimolecular Reactions on Metal Surfaces, Reference Module in Chemistry, Molecular Sciences and Chemical Engineering, Elsevier 2018.
- [84] J. Repp, G. Meyer, S. Paavilainen, F.E. Olsson, M. Persson, "Imaging Bond Formation Between a Gold Atom and Pentacene on an Insulating Surface", Science, **312** (2006) 1196-1199.
- [85] N. Pavliček, B. Schuler, S. Collazos, N. Moll, D. Pérez, E. Guitián, G. Meyer, D. Peña, L. Gross, "On-surface generation and imaging of arynes by atomic force microscopy", Nature Chemistry, **7** (2015) 623-628.
- [86] D.G. de Oteyza, P. Gorman, Y.-C. Chen, S. Wickenburg, A. Riss, D.J. Mowbray, G. Etkin, Z. Pedramrazi, H.-Z. Tsai, A. Rubio, M.F. Crommie, F.R. Fischer, "Direct Imaging of Covalent Bond Structure in Single-Molecule Chemical Reactions", Science, **340** (2013) 1434-1437.
- [87] S. Kawai, V. Haapasilta, B.D. Lindner, K. Tahara, P. Spijker, J.A. Buitendijk, R. Pawlak, T. Meier, Y. Tobe, A.S. Foster, E. Meyer, "Thermal control of sequential on-surface transformation of a hydrocarbon molecule on a copper surface", Nature Communications, **7** (2016) 12711.
- [88] N. Kocić, X. Liu, S. Chen, S. Decurtins, O. Krejčí, P. Jelínek, J. Repp, S.-X. Liu, "Control of Reactivity and Regioselectivity for On-Surface Dehydrogenative Aryl-Aryl Bond Formation", Journal of the American Chemical Society, **138** (2016) 5585-5593.
- [89] A. Riss, S. Wickenburg, P. Gorman, L.Z. Tan, H.-Z. Tsai, D.G. de Oteyza, Y.-C. Chen, A.J. Bradley, M.M. Ugeda, G. Etkin, S.G. Louie, F.R. Fischer, M.F. Crommie, "Local Electronic and Chemical Structure of Oligo-acetylene Derivatives Formed Through Radical Cyclizations at a Surface", Nano Letters, **14** (2014) 2251-2255.
- [90] Z. Majzik, A.B. Cuenca, N. Pavliček, N. Miralles, G. Meyer, L. Gross, E. Fernández, "Synthesis of a Naphthodiazaborinine and Its Verification by Planarization with Atomic Force Microscopy", ACS Nano, **10** (2016) 5340-5345.
- [91] M. Treier, C.A. Pignedoli, T. Laino, R. Rieger, K. Müllen, D. Passerone, R. Fasel, "Surface-assisted cyclodehydrogenation provides a synthetic route towards easily processable and chemically tailored nanographenes", Nature chemistry, **3** (2011) 61-67.
- [92] J. Björk, C. Sánchez-Sánchez, Q. Chen, C.A. Pignedoli, J. Rosen, P. Ruffieux, X. Feng, A. Narita, K. Müllen, R. Fasel, "The Role of Metal Adatoms in a Surface-Assisted Cyclodehydrogenation Reaction on a Gold Surface", Angewandte Chemie International Edition, **61** (2022) e202212354.

- [93] Q. Zhong, J. Jung, D. Kohrs, L.A. Kaczmarek, D. Ebeling, D. Mollenhauer, H.A. Wegner, A. Schirmeisen, "Deciphering the Mechanism of On-Surface Dehydrogenative C–C Coupling Reactions", *Journal of the American Chemical Society*, **146** (2024) 1849-1859.
- [94] K. Kaiser, L.M. Scriven, F. Schulz, P. Gawel, L. Gross, H.L. Anderson, "An sp-hybridized molecular carbon allotrope, cyclo[18]carbon", *Science*, **365** (2019) 1299-1301.
- [95] N. Pavliček, P. Gawel, D.R. Kohn, Z. Majzik, Y. Xiong, G. Meyer, H.L. Anderson, L. Gross, "Polyynes formation via skeletal rearrangement induced by atomic manipulation", *Nature Chemistry*, **10** (2018) 853-858.
- [96] Q. Zhong, A. Mardyukov, E. Solel, D. Ebeling, A. Schirmeisen, P.R. Schreiner, "On-Surface Synthesis and Real-Space Visualization of Aromatic P₃N₃", *Angewandte Chemie International Edition*, **62** (2023) e202310121.
- [97] M. Fritton, D.A. Duncan, P.S. Deimel, A. Rastgoo-Lahrood, F. Allegretti, J.V. Barth, W.M. Heckl, J. Björk, M. Lackinger, "The Role of Kinetics versus Thermodynamics in Surface-Assisted Ullmann Coupling on Gold and Silver Surfaces", *Journal of the American Chemical Society*, **141** **12** (2019) 4824-4832.
- [98] J.F. Dienstmaier, A.M. Gigler, A.J. Goetz, P. Knochel, T. Bein, A. Lyapin, S. Reichlmaier, W.M. Heckl, M. Lackinger, "Synthesis of Well-Ordered COF Monolayers: Surface Growth of Nanocrystalline Precursors versus Direct On-Surface Polycondensation", *ACS Nano*, **5** (2011) 9737-9745.
- [99] A. Kinikar, M. Di Giovannantonio, J.I. Urgel, K. Eimre, Z. Qiu, Y. Gu, E. Jin, A. Narita, X.-Y. Wang, K. Müllen, P. Ruffieux, C.A. Pignedoli, R. Fasel, "On-surface polyarylene synthesis by cycloaromatization of isopropyl substituents", *Nature Synthesis*, **1** (2022) 289-296.
- [100] S. Clair, S. Pons, A.P. Seitsonen, H. Brune, K. Kern, J.V. Barth, "STM Study of Terephthalic Acid Self-Assembly on Au(111): Hydrogen-Bonded Sheets on an Inhomogeneous Substrate", *The Journal of Physical Chemistry B*, **108** (2004) 14585-14590.
- [101] S. Haldar, M. Wang, P. Bhauriyal, A. Hazra, A.H. Khan, V. Bon, M.A. Isaacs, A. De, L. Shupletsov, T. Boenke, J. Grothe, T. Heine, E. Brunner, X. Feng, R. Dong, A. Schneemann, S. Kaskel, "Porous Dithiine-Linked Covalent Organic Framework as a Dynamic Platform for Covalent Polysulfide Anchoring in Lithium–Sulfur Battery Cathodes", *Journal of the American Chemical Society*, **144** (2022) 9101-9112.
- [102] B. Zhang, M. Wei, H. Mao, X. Pei, S.A. Alshimri, J.A. Reimer, O.M. Yaghi, "Crystalline Dioxin-Linked Covalent Organic Frameworks from Irreversible Reactions", *J. Am. Chem. Soc.*, **140** (2018) 12715-12719.
- [103] J. Guo, Y. Xu, S. Jin, L. Chen, T. Kaji, Y. Honsho, M.A. Addicoat, J. Kim, A. Saeki, H. Ihee, S. Seki, S. Irle, M. Hiramoto, J. Gao, D. Jiang, "Conjugated organic framework with

three-dimensionally ordered stable structure and delocalized π clouds", *Nat. Commun.*, **4** (2013) 2736.

[104] M. Li, W. Xie, X. Cai, X. Peng, K. Liu, Q. Gu, J. Zhou, W. Qiu, Z. Chen, Y. Gan, S.-J. Su, "Molecular Engineering of Sulfur-Bridged Polycyclic Emitters Towards Tunable TADF and RTP Electroluminescence", *Angewandte Chemie International Edition*, **61** (2022) e202209343.

[105] M. Antić, B. Furtula, S. Radenković, "Aromaticity of Nonplanar Fully Benzenoid Hydrocarbons", *J. Phys. Chem. A*, **121** (2017) 3616-3626.

[106] G.J. Bodwell, J.N. Bridson, M.K. Cyrański, J.W.J. Kennedy, T.M. Krygowski, M.R. Mannion, D.O. Miller, "Nonplanar Aromatic Compounds. 8.1 Synthesis, Crystal Structures, and Aromaticity Investigations of the 1,n-Dioxa[n](2,7)pyrenophanes. How Does Bending Affect the Cyclic π -Electron Delocalization of the Pyrene System?", *J. Org. Chem.*, **68** (2003) 2089-2098.

[107] Y. Li, A. Yagi, K. Itami, "Synthesis of Highly Twisted, Nonplanar Aromatic Macrocycles Enabled by an Axially Chiral 4,5-Diphenylphenanthrene Building Block", *J. Am. Chem. Soc.*, **142** (2020) 3246-3253.

[108] E. Nestoros, M.C. Stuparu, "Corannulene: a molecular bowl of carbon with multifaceted properties and diverse applications", *Chem. Commun.*, **54** (2018) 6503-6519.

[109] K.P. Kawahara, H. Ito, K. Itami, "One-step synthesis of polycyclic thianthrenes from unfunctionalized aromatics by thia-APEX reactions", *Org. Chem. Front.*, **10** (2023) 1880-1889.

[110] P.K. Saha, A. Mallick, A.T. Turley, A.N. Bismillah, A. Danos, A.P. Monkman, A.-J. Avestro, D.S. Yufit, P.R. McGonigal, "Rupturing aromaticity by periphery overcrowding", *Nat. Chem.*, **15** (2023) 516-525.

[111] M.E. Speer, M. Kolek, J.J. Jassoy, J. Heine, M. Winter, P.M. Bieker, B. Esser, "Thianthrene-functionalized polynorbornenes as high-voltage materials for organic cathode-based dual-ion batteries", *Chemical Communications*, **51** (2015) 15261-15264.

[112] D.A. Ryndyk, "Theory of quantum transport at nanoscale", *Springer Series in Solid-State Sciences*, **184** (2016) 9.

[113] M. Portais, C. Joachim, "Hole-electron quantum tunnelling interferences through a molecular junction", *Chemical Physics Letters*, **592** (2014) 272-276.

[114] F. Moresco, "Manipulation of large molecules by low-temperature STM: model systems for molecular electronics", *Phys. Rep.*, **399** (2004) 175-225.

- [115] L. Bartels, G. Meyer, K.H. Rieder, "Basic Steps of Lateral Manipulation of Single Atoms and Diatomic Clusters with a Scanning Tunneling Microscope Tip", *Physical Review Letters*, **79** (1997) 697-700.
- [116] W.-H. Soe, M. Kleinwächter, C. Kammerer, G. Rapenne, C. Joachim, "Mechanics of Molecule-Gears with Six Long Teeth", *The Journal of Physical Chemistry C*, **124** (2020) 22625-22630.
- [117] D. Skidin, T. Erdmann, S. Nikipar, F. Eisenhut, J. Krüger, F. Günther, S. Gemming, A. Kiriya, B. Voit, D.A. Ryndyk, C. Joachim, F. Moresco, G. Cuniberti, "Tuning the conductance of a molecular wire by the interplay of donor and acceptor units", *Nanoscale*, **10** (2018) 17131-17139.
- [118] S. Cekli, R. Winkel, E. Alarousu, O. Mohammed, K. Schanze, "Triplet Excited State Properties in Variable Gap π -Conjugated Donor-Acceptor-Donor Chromophores", *Chemical Science*, **7** (2016).
- [119] H.L. Tierney, C.J. Murphy, A.D. Jewell, A.E. Baber, E.V. Iski, H.Y. Khodaverdian, A.F. McGuire, N. Klebanov, E.C.H. Sykes, "Experimental demonstration of a single-molecule electric motor", *Nature Nanotechnology*, **6** (2011) 625-629.
- [120] A.M. Moore, P.S. Weiss, "Functional and Spectroscopic Measurements with Scanning Tunneling Microscopy", *Annual Review of Analytical Chemistry*, **1** (2008) 857-882.
- [121] D. Biermann, W. Schmidt, "Diels-Alder reactivity of polycyclic aromatic hydrocarbons. 1. Acenes and benzologs", *Journal of the American Chemical Society*, **102** (1980) 3163-3173.
- [122] P.v.R. Schleyer, M. Manoharan, H. Jiao, F. Stahl, "The Acenes: Is There a Relationship between Aromatic Stabilization and Reactivity?", *Organic Letters*, **3** (2001) 3643-3646.
- [123] J. Krüger, F. Eisenhut, J.M. Alonso, T. Lehmann, E. Guitián, D. Pérez, D. Skidin, F. Gamaleja, D.A. Ryndyk, C. Joachim, D. Peña, F. Moresco, G. Cuniberti, "Imaging the electronic structure of on-surface generated hexacene", *Chemical Communications*, **53** (2017) 1583-1586.
- [124] J. Krüger, F. Eisenhut, D. Skidin, T. Lehmann, D.A. Ryndyk, G. Cuniberti, F. García, J.M. Alonso, E. Guitián, D. Pérez, D. Peña, G. Trinquier, J.-P. Malrieu, F. Moresco, C. Joachim, "Electronic Resonances and Gap Stabilization of Higher Acenes on a Gold Surface", *ACS Nano*, **12** (2018) 8506-8511.
- [125] J. Krüger, F. García, F. Eisenhut, D. Skidin, J.M. Alonso, E. Guitián, D. Pérez, G. Cuniberti, F. Moresco, D. Peña, "Decacene: On-Surface Generation", *Angewandte Chemie International Edition*, **56** (2017) 11945-11948.

- [126] J. Krüger, N. Pavliček, J.M. Alonso, D. Pérez, E. Guitián, T. Lehmann, G. Cuniberti, A. Gourdon, G. Meyer, L. Gross, F. Moresco, D. Peña, "Tetracene Formation by On-Surface Reduction", *ACS Nano*, **10** (2016) 4538-4542.
- [127] J.I. Urgel, H. Hayashi, M. Di Giovannantonio, C.A. Pignedoli, S. Mishra, O. Deniz, M. Yamashita, T. Dienel, P. Ruffieux, H. Yamada, R. Fasel, "On-Surface Synthesis of Heptacene Organometallic Complexes", *Journal of the American Chemical Society*, **139** (2017) 11658-11661.
- [128] J.I. Urgel, S. Mishra, H. Hayashi, J. Wilhelm, C.A. Pignedoli, M. Di Giovannantonio, R. Widmer, M. Yamashita, N. Hieda, P. Ruffieux, H. Yamada, R. Fasel, "On-surface light-induced generation of higher acenes and elucidation of their open-shell character", *Nature Communications*, **10** (2019) 861.
- [129] M. Zugermeier, M. Gruber, M. Schmid, B.P. Klein, L. Ruppenthal, P. Müller, R. Einholz, W. Hieringer, R. Berndt, H.F. Bettinger, J.M. Gottfried, "On-surface synthesis of heptacene and its interaction with a metal surface", *Nanoscale*, **9** (2017) 12461-12469.
- [130] R. Zuzak, R. Dorel, M. Krawiec, B. Such, M. Kolmer, M. Szymonski, A.M. Echavarren, S. Godlewski, "Nonacene Generated by On-Surface Dehydrogenation", *ACS Nano*, **11** (2017) 9321-9329.
- [131] F. Eisenhut, T. Kühne, F. García, S. Fernández, E. Guitián, D. Pérez, G. Trinquier, G. Cuniberti, C. Joachim, D. Peña, F. Moresco, "Dodecacene Generated on Surface: Reopening of the Energy Gap", *ACS Nano*, **14** (2020) 1011-1017.
- [132] Z. Ruan, J. Schramm, J.B. Bauer, T. Naumann, H.F. Bettinger, R. Tonner-Zech, J.M. Gottfried, "Synthesis of Tridecacene by Multistep Single-Molecule Manipulation", *Journal of the American Chemical Society*, **146** (2024) 3700-3709.
- [133] R. Zuzak, M. Kumar, O. Stoica, D. Soler-Polo, J. Brabec, K. Pernal, L. Veis, R. Blicek, A.M. Echavarren, P. Jelinek, S. Godlewski, "On-Surface Synthesis and Determination of the Open-Shell Singlet Ground State of Tridecacene**", *Angewandte Chemie International Edition*, **63** (2024) e202317091.
- [134] K. Eimre, J.I. Urgel, H. Hayashi, M. Di Giovannantonio, P. Ruffieux, S. Sato, S. Otomo, Y.S. Chan, N. Aratani, D. Passerone, O. Gröning, H. Yamada, R. Fasel, C.A. Pignedoli, "On-surface synthesis and characterization of nitrogen-substituted undecacenes", *Nature Communications*, **13** (2022) 511.
- [135] M. Pinheiro, L.F.A. Ferrão, F. Bettanin, A.J.A. Aquino, F.B.C. Machado, H. Lischka, "How to efficiently tune the biradicaloid nature of acenes by chemical doping with boron and nitrogen", *Physical Chemistry Chemical Physics*, **19** (2017) 19225-19233.
- [136] M. Stolar, T. Baumgartner, "Phosphorus-Containing Materials for Organic Electronics", *Chemistry – An Asian Journal*, **9** (2014) 1212-1225.
- [137] W. Jiang, Y. Li, Z. Wang, "Heteroarenes as high performance organic semiconductors", *Chemical Society Reviews*, **42** (2013) 6113-6127.

- [138] B. Álvarez, J. Janeiro, A. Cobas, M.A. Ortuño, D. Peña, E. Guitián, D. Pérez, "Aryne-Based Synthesis of Cyclobutadiene-Containing Oligoacenes and Related Extended Biphenylene Derivatives", *Advanced Synthesis & Catalysis*, **366** (2024) 961-969.
- [139] D. Geuenich, K. Hess, F. Köhler, R. Herges, "Anisotropy of the Induced Current Density (ACID), a General Method To Quantify and Visualize Electronic Delocalization", *Chemical Reviews*, **105** (2005) 3758-3772.
- [140] T. Wang, S. Sanz, J. Castro-Esteban, J. Lawrence, A. Berdonces-Layunta, M.S.G. Mohammed, M. Vilas-Varela, M. Corso, D. Peña, T. Frederiksen, D.G. de Oteyza, "Magnetic Interactions Between Radical Pairs in Chiral Graphene Nanoribbons", *Nano Letters*, **22** (2022) 164-171.
- [141] A. Berdonces-Layunta, J. Lawrence, S. Edalatmanesh, J. Castro-Esteban, T. Wang, M.S.G. Mohammed, L. Colazzo, D. Peña, P. Jelínek, D.G. de Oteyza, "Chemical Stability of (3,1)-Chiral Graphene Nanoribbons", *ACS Nano*, **15** (2021) 5610-5617.
- [142] S. Mishra, D. Beyer, K. Eimre, S. Kezilebieke, R. Berger, O. Gröning, C.A. Pignedoli, K. Müllen, P. Liljeroth, P. Ruffieux, X. Feng, R. Fasel, "Topological frustration induces unconventional magnetism in a nanographene", *Nature Nanotechnology*, **15** (2020) 22-28.
- [143] R. Zuzak, R. Dorel, M. Kolmer, M. Szymonski, S. Godlewski, A.M. Echavarren, "Higher Acenes by On-Surface Dehydrogenation: From Heptacene to Undecacene", *Angewandte Chemie International Edition*, **57** (2018) 10500-10505.
- [144] R. Zuzak, A. Jančařík, A. Gourdon, M. Szymonski, S. Godlewski, "Correction to On-Surface Synthesis with Atomic Hydrogen", *ACS Nano*, **14** (2020) 14251-14252.
- [145] M. Bendikov, H.M. Duong, K. Starkey, K.N. Houk, E.A. Carter, F. Wudl, "Oligoacenes: Theoretical Prediction of Open-Shell Singlet Diradical Ground States", *Journal of the American Chemical Society*, **126** (2004) 7416-7417.
- [146] F. Plasser, H. Pašalić, M.H. Gerzabek, F. Libisch, R. Reiter, J. Burgdörfer, T. Müller, R. Shepard, H. Lischka, "The Multiradical Character of One- and Two-Dimensional Graphene Nanoribbons", *Angewandte Chemie International Edition*, **52** (2013) 2581-2584.
- [147] T. Stuyver, B. Chen, T. Zeng, P. Geerlings, F. De Proft, R. Hoffmann, "Do Diradicals Behave Like Radicals?", *Chemical Reviews*, **119** (2019) 11291-11351.
- [148] J.-P. Malrieu, G. Trinquier, "Can a Topological Approach Predict Spin-Symmetry Breaking in Conjugated Hydrocarbons?", *The Journal of Physical Chemistry A*, **120** (2016) 9564-9578.
- [149] E. Clar, *The Aromatic Sextet*, in: D. Rondia, M. Cooke, R.K. Haroz (Eds.) *Mobile Source Emissions Including Polycyclic Organic Species*, Springer Netherlands, Dordrecht, 1983, pp. 49-58.

- [150] Y. Gao, D. Xu, T. Cui, D. Li, "Stability of hydrogen-terminated graphene edges", *Physical Chemistry Chemical Physics*, **23** (2021) 13261-13266.
- [151] L. Talirz, H. Söde, J. Cai, P. Ruffieux, S. Blankenburg, R. Jafaar, R. Berger, X. Feng, K. Müllen, D. Passerone, R. Fasel, C.A. Pignedoli, "Termini of Bottom-Up Fabricated Graphene Nanoribbons", *Journal of the American Chemical Society*, **135** (2013) 2060-2063.
- [152] G. Chakraborty, I.-H. Park, R. Medishetty, J.J. Vittal, "Two-Dimensional Metal-Organic Framework Materials: Synthesis, Structures, Properties and Applications", *Chemical Reviews*, **121** (2021) 3751-3891.
- [153] W. Zheng, C.-S. Tsang, L.Y.S. Lee, K.-Y. Wong, "Two-dimensional metal-organic framework and covalent-organic framework: synthesis and their energy-related applications", *Materials Today Chemistry*, **12** (2019) 34-60.
- [154] B. Qie, Z. Wang, J. Jiang, Z. Zhang, P.H. Jacobse, J. Lu, X. Li, F. Liu, A.N. Alexandrova, S.G. Louie, M.F. Crommie, F.R. Fischer, "Synthesis and characterization of low-dimensional N-heterocyclic carbene lattices", *Science*, **384** (2024) 895-901.

Scientific contributions

Articles

S. Sarkar, B. Álvarez, K.H. Au-Yeung, A. Cobas, R. Robles, N. Lorente, D. Peña, D. Pérez, F. Moresco, "On-Surface Stepwise Double Dehydrogenation for the Formation of a para-Quinodimethane-Containing Undecacene Isomer", *Chemistry- A European Journal*, 30 (2024) e202402297.

S. Sarkar, K.H. Au-Yeung, T. Kühne, A. Waentig, D.A. Ryndyk, T. Heine, G. Cuniberti, X. Feng, F. Moresco, "Adsorption and reversible conformational change of a thiophene based molecule on Au(111)", *Scientific Reports*, 13 (2023) 10627.

S. Sarkar, P. Ferreira, K.H. Au-Yeung, P. Das, N. Khera, R. Robles, N. Lorente, K. M. Poulsen, Francesca Moresco, "Direct imaging of a norbornadiene (NBD) derivative adsorbed on the Au(111) surface", submitted.

P. Das, N. Sun, N. Khera, K.H. Au-Yeung, *S. Sarkar*, S. Park, R. Robles, N. Lorente, f. Lissel, F. Moresco, "N-Heterocyclic Carbene vs. Thiophene – Absorption and Unidirectional Rotation on Au(111)", submitted.

K.H. Au-Yeung, *S. Sarkar*, S. Halder, P. Das, T. Kühne, D.A. Ryndyk, P. Bhauriyal, S. Kaskel, T. Heine, G. Cuniberti, A. Schneemann, F. Moresco, "Tuning the Planarity of an Aromatic Thianthrene-Based Molecule on Au(111)", *The Journal of Physical Chemistry C*, 128 (2024) 1855-1861.

K.H. Au-Yeung, *S. Sarkar*, T. Kühne, O. Aiboudi, D.A. Ryndyk, R. Robles, F. Lissel, N. Lorente, C. Joachim, F. Moresco, "Thermal with Electronic Excitation for the Unidirectional Rotation of a Molecule on a Surface", *The Journal of Physical Chemistry C*, 127 (2023) 16989-16994.

K.H. Au-Yeung, *S. Sarkar*, T. Kühne, O. Aiboudi, D.A. Ryndyk, R. Robles, N. Lorente, F. Lissel, C. Joachim, F. Moresco, "A Nanocar and Rotor in One Molecule", *ACS Nano*, 17 (2023) 3128-3134.

K. H. Au-Yeung, T. Kühne, O. Aiboudi, *S. Sarkar*, O. Guskova, D. A Ryndyk, T. Heine, F. Lissel, F. Moresco, "STM-induced ring closure of vinylheptafulvene molecular dipole switches on Au(111)". *Nanoscale Advances*, 4 (2022), 4351-4357.

Other publications

K. H. Au-Yeung, S. Sarkar, F. Moresco, "Driving a single chemisorbed molecule-rotor by thermal energy and tunneling electrons". Advances in Atom and Single Molecule Machines, 2024, Springer.

T. Kühne, K. H. Au-Yeung, S. Sarkar, C. Joachim, F. Moresco, "Azulene Based Nanocars. Single Molecule Mechanics on a Surface." Advances in Atom and Single Molecule Machines, 2023, Springer.

Talks

On-Surface Stepwise Double Dehydrogenation for the Formation of a para-Quinodimethane-Containing Undecacene Isomer

DPG Surface Science Division

Berlin, 2024

LT-STM induced reversible switching of thiophene based molecule on Au(111)

ECOSS Conference

Lodz, Poland, 2023

III: Atomically Precise Single-Layer 2D Conjugated Polymer Frameworks Studied by LT-STM

MGK Seminar

Dresden, 2023

STM-induced ring closure of vinylheptafulvene molecular dipole switches on Au(111)

DPG Surface Science Division

Dresden, 2023

Unidirectional Rotation between Electronic and Thermal Excitation

ESiM Project Meeting

San Sebastian, 2023

II: Atomically Precise Single-Layer 2D Conjugated Polymer Frameworks Studied by LT-STM

IRTT Seminar

Dresden, 2023

LT-STM induced reversible Chiral switching of thiophene based molecule on Au(111)
DPG Surface Science Division
Regensburg, 2022

I: Atomically Precise Single-Layer 2D Conjugated Polymer Frameworks Studied by LT-STM
MGK Seminar
Dresden, 2022

Posters

On-Surface Stepwise Double Dehydrogenation for the Formation of a para-Quinodimethane-Containing Undecacene Isomer
On-surface synthesis workshop (OSS24)
Girona, Spain 2024

Adsorption and reversible conformational change of a thiophene based molecule on Au(111)
CRC 1415 Retreat 2023

Manipulation and functional nanomaterials Retreat
Bad Honnef 2022

Challenges in 2D On-Surface Synthesis-Experimental Perspective
CRC 1415 Retreat 2022

Outreach

Images and oral presentation contribution

“Imaging Science – Die Schönheit der Wissenschaft” Exhibition
Dresden, Germany (September 2021)

Winner of cfaed Image Competition (May 2023)

Nanocar pilot
The Second International Nanocar Race
Toulouse, France (July 2021)

Acknowledgement

I gratefully acknowledge the constant support and motivation provided by the group leader of SMM, Dr. Francesca Moresco, under whose guidance I did my doctoral studies. I am especially thankful to her for giving me the opportunity of joining her group and supporting me through this journey.

I would like to extend thanks to all the past and present group members, especially my colleagues Dr. Kwan Ho Au-Yeung and Dr. Tim Kuehne, who were fellow PhD. Students when I joined the group and were a big part of my everyday lab life. Franz Plate, Natasha Khera and Pranjit Das who were working alongside me during the tail-end of my thesis are also much appreciated.

I would like to thank my supervisor Prof. Dr. Cuniberti for taking time out from his busy schedule to discuss my progress and also to Prof. Dr. Franziska Lissel for collaborating with me on many projects and supervising my thesis.

To our theory collaborators, Nikolas Lorente, Roberto Robles and Dmitry Ryndyk, many thanks for your support.

Finally, to all family and friends who listened to me talking about quantum physics, especially my husband Enrico Marzotto, who now knows more about HOMO-LUMO gaps than any other geologist, and my mother, Swati Sarkar, who has always been my rock, and my father, Milonendu Sarkar, for always guiding me through the ether.

Curriculum Vitae

Personal Information

Name Suchetana Sarkar
Address Nuernbergerstr. 37, 01187 Dresden
Telephone +49 176 64712630
E-mail suchetana.sarkar@tu-dresden.de
Gender Female

List of Publications

- *Suchetana Sarkar*, Berta Álvarez, Kwan Ho Au-Yeung, Agustín Cobas, Roberto Robles, Nicolas Lorente, Diego Peña, Dolores Pérez, and Francesca Moresco "On-Surface Stepwise Double Dehydrogenation for the Formation of a para-Quinodimethane-Containing Undecacene Isomer", In Chemistry- A European Journal, vol 30, July 2024
- Kwan Ho Au-Yeung, *Suchetana Sarkar*, Sattwick Haldar, Pranjit Das, Tim Kühne, Dmitry A. Ryndyk, Preeti Bhauriyal, Stefan Kaskel, Thomas Heine, Gianaurelio Cuniberti, Andreas Schneemann, Francesca Moresco, "Tuning the Planarity of an Aromatic Thianthrene-Based Molecule on Au(111)", In The Journal of Physical Chemistry C, American Chemical Society (ACS), vol. 128, no. 4, pp. 1855–1861, Jan 2024.
- Kwan Ho Au-Yeung, *Suchetana Sarkar*, Tim Kühne, Oumaima Aiboudi, Dmitry A. Ryndyk, Roberto Robles, Franziska Lissel, Nicolas Lorente, Christian Joachim, Francesca Moresco, "Thermal with Electronic Excitation for the Unidirectional Rotation of a Molecule on a Surface", In The Journal of Physical Chemistry C, American Chemical Society (ACS), vol. 127, no. 34, pp. 16989–16994, Aug 2023.
- *Suchetana Sarkar*, Kwan Ho Au-Yeung, Tim Kühne, Albrecht Waentig, Dmitry A. Ryndyk, Thomas Heine, Gianaurelio Cuniberti, Xinliang Feng, Francesca Moresco, "Adsorption and reversible conformational change of a thiophene based molecule on Au(111)", In Scientific Reports, Springer Science and Business Media LLC, vol. 13, no. 1, Jun 2023

- Kwan Ho Au-Yeung, *Suchetana Sarkar*, Tim Kühne, Oumaima Aiboudi, Dmitry A. Ryndyk, Roberto Robles, Nicolas Lorente, Franziska Lissel, Christian Joachim, Francesca Moresco, "A Nanocar and Rotor in One Molecule", In ACS Nano, American Chemical Society (ACS), Jan 2023
- Kwan Ho Au-Yeung, Tim Kühne, Oumaima Aiboudi, *Suchetana Sarkar*, Olga Guskova, Dmitry A. Ryndyk, Thomas Heine, Franziska Lissel, Francesca Moresco, "STM-induced ring closure of vinylheptafulvene molecular dipole switches on Au(111)", In Nanoscale Advances, Royal Society of Chemistry (RSC), vol. 4, no. 20, pp. 4351–4357, 2022.
- Sumit Beniwal, *Suchetana Sarkar*, Felix Baier, Birgit Weber, Peter A Dowben and Axel Enders, "Site selective adsorption of the spin crossover complex Fe(phen)2(NCS)2 on Au(111)", in Journal of Physics: Condensed Matter 32, 2020

Education and Training

15.09.2020 – 19.12.2024: Magna cum Laude for the dissertation, disputation and Rigor Rosum

Doctoral Student in Physics, Single Molecules Machines Group, cfaed TU Dresden

Teaching Duties:

Tutor for Molecular Electronics, WS 2021, WS 2022

Lab Teacher for Physics Grundpraktikum II: SS 2022

Lab Teacher for Fortgeschrittene Praktikum: Molecular and Organic Electronics: SS 2021, WS 2023

19.01.2017-06.03.2020

Research Associate- Functional Nanostructures Lab, Experimental Physics Dept.
Bayreuth University

Teaching Duties:

Tutor for Grundpraktikum: Komplexer Widerstaende WS 2018, WS 2019

24.09.2012 – 7.03.2016

Title of qualification awarded Master of Science, Scientific Instrumentation.

Thesis: "Sensor Development Using Novel Magnetic Detection Technology"

Specialization: Advanced 3D Design, FEM and Simulation, Precision Instrumentation, Physical Material Diagnostics, Nanoelectronics

Institution: Ernst Abbe Fachhochschule, Jena

September 2007- May 2011

Title of qualification awarded Bachelor of Engineering, Instrumentation and Control Engineering

Specialization: Analog System Design, Instrumentation Transducers, Control Systems, Analog Electronic Circuits, Microprocessor and Microcontroller Programming

Institution: Manipal Institute of Technology, Manipal, India.

Project Experience(s)

1. Energy Management in Home Automation Systems- BPL Pvt. Ltd. (Bachelor Thesis, 2011).
2. Circuit Development for Colour Television-LG Electronics (Bachelor Project, 2010).
3. Programming Robotic Arm for Toyota Car Design - L&T (Bachelor Project, 2009).
4. P&I Diagrams design for Desalination Plant- L&T (Bachelor Project, 2009)

Research Internship(s): Development of a Novel Parametric Array Design

October 2013- May 2014

Upgradation of Low-Level Architecture and Control Systems for TRD- ALICE, CERN

July 2014- July 2015

Work Experience: Electronic Design Engineer, R& D, BPL, India

August, 2011- April 2012

Reference

Dr. Francesca Moresco

Group Leader: Single Molecules Machines Group, cfaed, TU Dresden

E-Mail: francesca.moresco@tu-dresden.de

Statement of authorship

Folgende Erklärung gebe ich hiermit ab:

1. Ich versichere, dass ich die vorliegende Arbeit ohne unzulässige Hilfe Dritter und ohne Benutzung anderer als der angegebenen Hilfsmittel angefertigt habe; die aus fremden Quellen direkt oder indirekt übernommenen Gedanken sind als solche kenntlich gemacht.

2. Bei der Auswahl und Auswertung des Materials sowie bei der Herstellung des Manuskripts habe ich Unterstützung von folgenden Personen erhalten:

- a. Prof. G. Cuniberti
- b. Dr. F. Moresco
- c. Prof. C. Joachim
- d. Prof. F. Lissel
- e. Prof. N. Lorente
- f. Prof. D. Pena
- g. Dr. D. A. Ryndyk
- h. Prof. X. Feng
- i. Prof. T. Heine

Weitere Personen waren an der geistigen Herstellung der vorliegenden Arbeit nicht beteiligt. Insbesondere habe ich nicht die Hilfe eines kommerziellen Promotionsberaters in Anspruch genommen. Dritte haben von mir keine geldwerten Leistungen für Arbeiten erhalten, die in Zusammenhang mit dem Inhalt der vorgelegten Dissertation stehen.

3. Die Arbeit wurde bisher weder im Inland noch im Ausland in gleicher oder ähnlicher Form einer anderen Prüfungsbehörde vorgelegt und ist auch noch nicht veröffentlicht worden.

4. Die Promotionsordnung der Fakultät Mathematik und Naturwissenschaften an der TU Dresden vom 23.02.2011 wird anerkannt.